NAWI
Graz

TU
Graz

AFFIDAVIT

I declare that I have authored this thesis independently, that I have not used other than the declared sources/resources, and that I have explicitly indicated all material which has been quoted either literally or by content from the sources used. The text document uploaded to TUGRAZonline is identical to the present master‘s thesis.

Date

Signature

University Supervisor

Kalcher Kurt, Ao.Univ.-Prof. Dr.phil

Institute of Chemistry, Karl-Franzens University Graz

8010 Graz, Universitätsplatz 1/I

kurt.kalcher@uni-graz.at

Industry Supervisor

Markus Kahn, Dr. mont.

Infineon Technologies Austria AG

Siemensstraße 2, 9500 Villach

markus.kahn@infineon.com

Co-Supervisor

Schönherr Helmut, DI

Infineon Technologies Austria AG

Siemensstraße 2, 9500 Villach

helmut.schönherr@infineon.com

Acknowledgements

I want to say special thanks to

Prof. Kalcher for giving me the opportunity to write this thesis and supporting my work all along,

Dr. Kahn for teaching, guiding and challenging me,

DI Schönherr for his advice and assistance,

MSc. Leitl for the efficient cooperation and for introducing me to the world of physics,

the participants of the weekly meeting ‘DLC Jour Fixe’ for the encouragement and inspiring discussions,

Dr. Heider for providing me a basic insight into the field of metrology,

the department at Infineon Villach for giving me such a warm and friendly welcome,

the staff of the Institute of Chemistry – Analytical Chemistry at Graz University for all the cake and nice discussions during lunch breaks,

and of course,

my parents and sisters for always believing in me and supporting my dream of becoming a scientist.

Abstract

This work focuses on examining the influence of plasma enhanced chemical vapour deposition (PECVD) process design on the electrochemical corrosion stability of dielectric films used in power semiconductor industry.

Power semiconductor devices are used in power electronics for the conversion of electrical energy. Amorphous silicon carbide (a-SiC) is a tetrahedral alloy of silicon and carbon that exhibits a high wear resistance and high dielectric properties. In edge termination structures a-SiC can serve as electroactive passivation and protection layer on the semiconductor body, which has to withstand high electric fields. Degradation of the semiconductor body might lead to the loss of the voltage blocking capability and subsequently to preliminary failure of the power device.

The test objects were silicon wafers coated with a-SiC films which were varied regarding RF power density, elemental composition, film thickness and type of deposition chamber. The electrochemical corrosion stability was investigated with electrochemical impedance spectroscopy (EIS) and polarization experiments with Tafel extrapolation.

The electrochemical measurements revealed that the resistance of a-SiC against electrochemical attacks can be improved by decreasing the conductivity of the respective films. Upon increasing RF power an increasing conductivity and densification of a-SiC was observed. High RF powers promoted both the incorporation of carbon in the network as well as the beginning graphitization of the layers. The a-SiC film deposited at low RF power however exhibited a high resistivity and polymer-like features, due to its low moisture barrier ability however it cannot be used in power semiconductor devices. By raising the gas flow rate of the silicon precursor the incorporation of tetrahedrally bonded silicon was promoted and the electrochemical corrosion stability was improved. The choice of deposition chamber and set of parameters had a major impact on elemental composition, structure and corrosion stability of a-SiC. Subsequent heat treatment (annealing) was proven to further enhance the electrochemical corrosion resistance of the films.

Zusammenfassung

Die vorliegende Arbeit konzentriert sich auf die Untersuchung des Einflusses des Prozessdesigns von plasma-unterstützer chemischer Gasphasen-Abscheidung (englisch PECVD) auf die elektrochemische Korrosionsstabilität von dielektrischen Dünnschichten, die in Halbleiter-Leistungsbauelementen verwendet werden.

Halbleiter-Leistungsbauelemente werden in Leistungselektronik zur Umwandlung von elektrischem Strom eingesetzt. Amorphes Siliciumcarbid (a-SiC) ist eine tetraedrische Verbindung bestehend aus Silicium und Kohlenstoff, die eine hohe Verschleißfestigkeit und gute dielektrische Eigenschaften aufweist. In Bauelementen mit Randabschluss kann a-SiC als elektroaktive Passivierungs- und Schutzschicht auf dem Halbleiterkörper, der hohen elektrischen Feldern standhalten muss, dienen. Die Schädigung des Halbleiterkörpers kann zu dem Verlust der Blockierfähigkeit und des Weiteren zu einem vorzeitigen Ausfall des Leistungsbauelementes führen.

Die Testobjekte waren mit a-SiC beschichtete Siliziumwafer. Die Dünnschichten wurden hinsichtlich der Plasma Leistungsdichte, der Elementzusammensetzung, der Filmdicke und der Art der Abscheidungskammer variiert. Die elektrochemische Korrosionsstabilität wurde mit elektrochemischer Impedanzspektroskopie (EIS) und Polarisationsexperimenten mit Tafel-Extrapolation untersucht.

Die elektrochemischen Messungen ergaben, dass die Stabilität von a-SiC gegenüber elektrochemischen Angriffen durch eine Verringerung der Schichtleitfähigkeit verbessert werden kann. Bei zunehmender Plasma-Leistung wurden eine Leitfähigkeitszunahme und die Verdichtung von a-SiC beobachtet. Hohe Plasma-Leistungen förderten sowohl den Einbau von Kohlenstoff ins amorphe Netzwerk, als auch die beginnende Graphitisierung der Schichten. Die bei niedriger Plasma-Leistung abgeschiedene a-SiC-Schicht wies einen hohen spezifischen Widerstand und polymerähnliche Eigenschaften auf, kann aber aufgrund ihres hohen Wasserabsorptionsvermögens jedoch nicht in Halbleiter-Leistungsbauelementen als Teil des Randabschlusses verwendet werden. Durch Erhöhen des Gasflusses der Silicium-Quelle wurde verstärkt tetraedrisch gebundenes Silicium in den Schichten eingebaut und die elektrochemische Korrosionsstabilität verbessert. Die Wahl der Abscheidekammer und der Abscheideparameter hatte einen wesentlichen Einfluss auf die Zusammensetzung, Struktur und Korrosionsbeständigkeit von a-SiC. Eine zusätzliche Wärmebehandlung nach der Abscheidung (englisch annealing) erzielte eine weitere Verbesserung der Korrosionsstabilität der Schichten.

Contents

Acknowledgements 2
Abstract 3
Zusammenfassung 4
Contents 5
List of Figures 6
List of Tables 8
Abbreviations 9
1. Introduction 10
2. Theoretical 12
2.1. Power semiconductors and edge termination structures 12
2.1.1 Power semiconductor devices 12
2.1.2 Applications of IGBTs and diodes 13
2.1.3 Properties of semiconductors 14
2.1.4 Pn-junction and depletion region 16
2.1.5 Challenges in edge-termination design 18
2.1.6 Reliability behaviour and film degradation 19
2.1.7 Carbon-based semiconductor materials: Silicon carbide 20
2.2 Carbon-based Thin Films in Power Semiconductor Industry 21
2.2.1 Carbon- based film types and their applications 21
2.2.2 Deposition techniques for amorphous silicon carbide thin films 23
2.2.3 Characterization of thin films 26
2.3 Electrochemical corrosion measurement techniques 30
2.3.1 Basics of corrosion 30
2.3.2 Electrochemical corrosion 31
2.3.3 Polarization measurements and Tafel extrapolation 39
2.5.4 Electrochemical impedance spectroscopy 43
3. Experimental 51
3.1 Sample preparation and thin film deposition 51
3.1.1 Samples for investigating the influence of deposition parameters on thin film properties and corrosion behaviour 51
3.1.2 Samples for investigating the influence of the deposition chamber and heat treatment on the corrosion behaviour of the thin films 52
3.1.3 Samples for testing the corrosion behaviour of silicon oxides and nitride 52
3.2 Thin film characterization 53
3.2.1 Stress measurements 53
3.2.2 Fourier Transform Infrared Spectroscopy 53
3.2.3 Optical measurements 53
3.3 Electrochemical corrosion measurements 54
3.4 High humidity performance test (AC tests) 59
4. Results and Discussion 60
4.1 Thin film characterization 60
4.1.1 Optical characterization 60
4.1.2 Stress behaviour 65
4.1.3 Infrared spectroscopy 65
4.1.4 Film characterization summary 67
4.2 Electrochemical corrosion measurements 68
4.2.1 Corrosion behaviour of a-SiC thin films as a function of RF power 68
4.2.2 Corrosion behaviour as a function of film thickness 86
4.2.3 Corrosion behaviour depending on stoichiometry 89
4.2.4 Corrosion behaviour of oxides and nitride passivation layer 94
4.2.5 Corrosion behaviour for a-SiC films deposited by different chamber types 98
5 Conclusions 107
References 111

List of Figures

Figure 1: Graphical representation of energy bands in solids, after [hype58] 15
Figure 2: Pn-junctions in the most common semiconductor power devices [lutz1] 17
Figure 3: Pn-junction (cf. Semiconductor devices [dasg4] 18
Figure 4: Forward and reverse bias of pn-junction [lutz1] 18
Figure 5: A on the left shows a pn-junction in reverse bias. The space charge region (SCR) expands to the n- area. In the curved area close to the surface an increase in electric field strength occurs. B: pn-junction with JTE resp. VLD as edge termination, after [knip8] 19
Figure 6: Tetrahedral structure of silicon carbide [sadd6] 20
Figure 7: Ternary phase diagram of the bonding situation in amorphous carbon hydrogen alloys [robe10] 21
Figure 8: CVD reaction steps: Introduction of the reaction and carrier gases into the reactor (A), followed by the activation of the gas species by heat, plasma etc. (B). Adsorption of the reactive species on the substrate (C) and formation of a solid thin film (D). The last two steps involve desorption of by-products from the substrate (E) and their following removal from the reactor (F) [xia18]. 24
Figure 9: PECVD system [lnf59] 25
Figure 10: Sample ellipsometry measurement (source: J.A. Woollam Co.) 28
Figure 11: Setup for Beam Profile Reflectometry [dieb33] 29
Figure 12: Tauc plot for hydrogenated amorphous silicon [flew35] 30
Figure 13: A basic corrosion cell [ahmad23] 31
Figure 14: Polarization diagram of species M [ahmad23] 36
Figure 15: The impact of the change of the electrode potential on the free energy barrier [caff24] 36
Figure 16: Typical Tafel plot [zoski25] 38
Figure 17: Comparison of actual and measured polarization curves [ahmad23] 40
Figure 18: Hypothetical Tafel plot [ahmad23] 41
Figure 19: Sinusoidal input voltage V (above) and resulting current response I (below) at a single frequency [lvov28] 43
Figure 20: A Lissajous Figure; B Nyquist plot [lvov28] 45
Figure 21: Examples for Bode plots [gamry29] 46
Figure 22: Nyquist plot and equivalent circuit for an undamaged coating [gamry29] 48
Figure 23: On the left Nyquist plot, on the right Bode plots of Warburg impedance [gamry29] 49
Figure 24: Equivalent circuit for Randles cell [gamry29] 49
Figure 25: Nyquist plot of a randles cell [metr30] 50
Figure 26: The measuring station with potentiostat on the left and electrochemical cell on the right 55
Figure 27: Schematic cross-section of the electrochemical cell 57
Figure 28: Technical drawings of the electrochemical cell 58
Figure 29: On the left: the customized cup with the specimen on the bottom. On the right: The cup and the lid with the pogo pin for back-side contact 58
Figure 30: TOF-ERDA results for elemental composition of a-SiC thin films depending on silane and methane gas flow ratio 61
Figure 31: Results from the refractive index determination 61
Figure 32: Determination of Tauc gap and band gap E04 [stenz39] 62
Figure 33: Comparison between Tauc gap (Opti-Probe) and band gap (N&K) 62
Figure 34: Change of the Tauc slope with the change of silane/methane gas flow ratio 63
Figure 35: Refractive index as a function of RF power density 64
Figure 36: The optical band gap as function of the RF power density 64
Figure 37: The slope from the Tauc plot as function of RF power density 64
Figure 38: Intrinsic film stress as a function of RF power density 65
Figure 39: Absorption spectrum for PECVD a-SiC with varying silane/methane gas flow ratio 67
Figure 40: Tafel plots of a-SiC thin films with varying RF power in 0,35% aqueous NaCl solution 69
Figure 41: Corrosion rates of the blank wafer sample in different corrosive media 70
Figure 42: Corrosion stability in different media as a function of RF power density 70
Figure 43: Comparison of the corrosion resistance of the samples deposited at low RF powers 71
Figure 44: Ecorr and icorr as a function of residual film stress 71
Figure 45: Nyquist plot of the blank silicon wafer in 0,35% aqueous NaCl solution with Fe(II)/Fe(III) redox couple 73
Figure 46: Equivalent circuit model of the blank silicon wafer 73
Figure 47: Nyquist plot of a-SiC LP (1,11 W/cm²) in 0,35% aqueous NaCl solution with Fe(II)/Fe(III) redox couple 74

Figure 48: Equivalent circuit model of a-SiC LP and a-SiC ST 74
Figure 49: Nyquist plot of a-SiC ST (1,59 W/cm²) in 0,35% aqueous NaCl solution with Fe(II)/Fe(III) redox couple 75
Figure 50: Nyquist plot for a-SiC MP (2,07 W/cm²) in 0,35% aqueous NaCl solution with Fe(II)/Fe(III) redox couple 75
Figure 51: Equivalent circuit model for a-SiC MP 75
Figure 52: Nyquist plot for a-SiC HP (2,55 W/cm²) in 0,35% aqueous NaCl solution with Fe(II)/Fe(III) redox couple 76
Figure 53: Equivalent circuit model corresponding to a-SiC HP 76
Figure 54: Corrosion rates and charge transfer resistances in dependence on RF power density during PECVD 77
Figure 55: Refractive index and intrinsic film stress as a function of RF power density 78
Figure 56: Results from the conductivity measurements on MIS-C structures; conductivity as a function of power density 81
Figure 57: Charge transfer resistance and conductivity as a function of RF power density 81
Figure 58: Raman spectrum for a-SiC deposited with RF power density of 1,11 W/cm² 83
Figure 59: Raman spectra for RF power densities between 1,59 and 2,55 W/cm² 84
Figure 60: Comparison of IR spectra deposited at different RF power densities 85
Figure 61: Tafel plots of a-SiC with variation of film thickness 86
Figure 62: Nyquist plots of a-SiC with variation of film thickness 87
Figure 63: Equivalent circuit model for a-SiC with variation of film thickness 87
Figure 64: Results from the conductivity measurements on MIS-C structures; conductivity as a function of power density for varying a-SiC film thickness 88
Figure 65: Charge transfer resistance and conductivity as a function of film thickness 89
Figure 66: Tafel plots for the variation of the silane/methane gas flow ratio during deposition 90
Figure 67: EIS spectra (Nyquist plots) for the variation of the silane/methane gas flow ratio 91
Figure 68: Equivalent circuit model for a-SiC deposited with increasing silane/methane gas flow ratio 91
Figure 69: Equivalent circuit model for a-SiC deposited with increasing silane/methane gas flow ratio 91
Figure 70: Results of the conductivity measurements for a-SiC PECVD with different silane/methane gas flow ratios 92
Figure 71: Charge transfer resistance and conductivity as a function of the silane/methane gas flow ratio 93
Figure 72: Corrosion rate and charge transfer resistance as a function of elemental composition of a-SiC 94
Figure 73: EIS spectra (Nyquist plot) of silicon wafers coated with a-SiC/nitride layer 95
Figure 74: Equivalent circuit of a purely capacitive coating 95
Figure 75: EIS spectra (Nyquist plot) of POLOX, in situ and after 65 hours immersion in 0,35% aqu. NaCl solution 96
Figure 76: EIS spectra (Nyquist plot) of polymeric SiC 96
Figure 77: Comparison of the conductivities between PR SiC and a-SiC deposited at different RF power densities 97
Figure 78: IR spectra of PR SiC and a-SiC deposited at low RF power 97
Figure 79: Tafel plot analysis for lot VC058588 99
Figure 80: Polarization measurement of a-SiC CxZ after annealing 99
Figure 81: Nyquist plot of the blank sample 100
Figure 82: Equivalent circuit model for the blank silicon wafer 100
Figure 83: Nyquist plot for a-SiC MKII 100
Figure 84: Equivalent circuit model for a-SiC MKII 101
Figure 85: Nyquist plot for a-SiC MKII after thermal treatment 101
Figure 86: Equivalent circuit model for a-SiC MKII annealed and a-SiC CxZ 101
Figure 87: Nyquist plot of a-SiC CxZ 102
Figure 88: Nyquist plot of a-SiC CxZ after heat treatment, shown in detail in the right corner 102
Figure 89: Equivalent circuit model for a-SiC CxZ after annealing 102
Figure 90: Elemental composition [at-%] of a-SiC deposited in CxZ and MKII chamber 104
Figure 91: IR spectra of a-SiC deposited in CxZ and MKII chambers 104
Figure 92: Corrosion rate and charge transfer resistance for each sample (ht: heat treatment) 105
Figure 93: Graphical representation of the corrosion mechanism of a-SiC 108

List of Tables

Table 1: Common circuit elements [gamry29] 46
Table 2: Silicon wafers coated with a-SiC thin films with varying PECVD conditions 51
Table 3: Silicon wafers with a-SiC coating deposited in two different chambers, with and without heat treatment 52
Table 4: Summary of the used silicon oxide and nitride coatings 53
Table 5: List of typical vibrations in FT-IR of a-SiC, after [bull40] 66
Table 6: Corrosion rates of a-SiC films in different media as function of RF power 69
Table 7: Corrosion properties of samples with varying RF power density in 0,35% aqu. NaCl electrolyte 71
Table 8: Calculated inhibition efficiencies in different media 72
Table 9: Comparison of corrosion rates obtained by Tafel plot analysis and charge transfer resistances from EIS measurements 76
Table 10: Standard electrode potentials of reactions that are relevant for a-SiC corrosion [wiki45] 78
Table 11: Data from Tafel plot analysis and inhibition efficiencies for the variation of film thickness (lotVE642365) 86
Table 12: Comparison of corrosion rates obtained by Tafel plot analysis and charge transfer resistances from EIS mesasurements 87
Table 13: Results from Tafel plot measurements (variation of stoichiometry) 90
Table 14: Comparison of the results from Tafel plot analysis and EIS measurements 92
Table 15: Results from Tafel plot analysis (ht.: heat treatment) 98
Table 16: Comparison of corrosion rates and charge transfer resistances for the samples of lot VC058588 103
Table 17: Comparison of film parameters of a-SiC deposited in CxZ and MKII chambers 105

Abbreviations

a-SiC .... amorphous silicon carbide
BKM .... internal best known method
CPE .... constant phase element
CVD .... chemical vapour deposition
DLC .... diamond-like carbon
EIS .... electrochemical impedance spectroscopy
FT-IR .... Fourier transform infrared spectroscopy
IR .... infrared spectroscopy
NIT .... nitride passivation layer
NIR .... near infrared
PECVD .... plasma enhanced chemical vapour deposition
RF .... radio frequency
R_{ct} .... charge transfer resistance
R_s .... solution resistance
sccm .... standard cubic centimetre per minute
UV .... ultraviolet

1. Introduction

The aim of this thesis is to examine the stability and electrochemical corrosion resistance of dielectric films used in power semiconductor industry. The test objects are silicon wafers coated with amorphous silicon carbide (a-SiC) with and without nitride passivation layer. Silicon oxide layers deposited with different parameters and a polymer-like silicon carbide film will be studied as well.

Amorphous silicon carbide is used as thin film and electroactive layer in edge termination structures in high voltage semiconductor power devices [schmidt63] and as barrier layer in sensors, actuators, and microelectromechanical systems [ili16]. Failure in electronic power devices due to corrosion can lead to damage with serious consequences, not only economically but also as far as the safety of the final users is concerned. Potential risks and weak spots must be assessed during the design phase of the product and eliminated.

In order to avoid premature failure of a-SiC layers in power devices, the correlation between specific film properties and measured corrosion resistance will be examined and evaluated. The films will be characterized with infrared spectroscopy, stress measurements and optical measurement techniques. Furthermore, the influence of the deposition parameters on intrinsic stress, optical bandgap, refractive index and extinction coefficient will be examined. For this purpose the specifications of the operating conditions of the plasma-enhanced chemical vapour deposition are varied regarding RF power, film thickness and silane flow rate.

The corrosion stability of a-SiC will be examined by electrochemical corrosion measurements, i.e. polarization measurements with Tafel extrapolation and electrochemical impedance spectroscopy (EIS). The influence of deposition conditions, of the used deposition chamber and of heat treatment of the thin films on the corrosion behaviour will be investigated.

Besides from the introduction (chapter 1), this thesis will be organized in four chapters which are Theoretical, Experimental, Results and Discussion, and Conclusions.

Chapter 2 is divided in three parts and provides the necessary background knowledge and a basic understanding of the materials and methods used.

In chapter 3 the methods for sample preparation and characterization for electrochemical corrosion testing are specified.

In chapter 4 the outcome of the film characterization and of the electrochemical corrosion measurements are reviewed. The main focus is laid on the impact of the variation of the deposition conditions on the

resulting properties and corrosion resistance of the thin films. The main findings are summarized in chapter 5.

The objective is to gain an insight into the relations of material degradation, corrosion mechanisms and related film properties, in order to increase the quality and stability of the final product in the application. Based on the gained knowledge, preliminary device failures shall be further avoidable and the design process of new appliances shall be facilitated. Advances in material science and characterization do not only promote current technologies, but further lay ground for the future possible applications of a-SiC and derive process-relevant information which can be used analogously in similar tasks.

2. Theoretical

This chapter provides background information about the properties and applications of carbon-based thin films, power semiconductor devices and electrochemical corrosion measurement techniques. It is divided in the following three parts:

2.1 Power semiconductors and edge termination structures

> This subchapter provides an insight into common power semiconductor devices and their applications. The basic properties and features of semiconductor materials and their use will be presented. Furthermore, crystalline silicon carbide, a promising bulk and thin film material for future power semiconductor applications will be discussed.

2.2 Carbon-based thin films in power semiconductor industry

> In this subchapter, the properties and applications of two common amorphous carbon-based thin films are examined: diamond-like carbon (DLC) and amorphous silicon carbide (a-SiC). Also the typical deposition methods for a-SiC thin films and the methods for film characterization will be presented.

2.3 Electrochemical corrosion measurement techniques

> A general insight into corrosion and its causes will be given. Then the electrochemical background of corrosion mechanisms is explored by describing the thermodynamics and kinetics of corrosion reactions. After the general part, an insight into two widely used corrosion measurement techniques shall be offered; polarization measurements with Tafel plot extrapolation and electrochemical impedance spectroscopy.

2.1. Power semiconductors and edge termination structures

2.1.1 Power semiconductor devices

Power semiconductor devices are the key components in power electronics that use advanced technologies for electrical energy conversion [lutz1].They are used in power electronic circuits as switches or rectifiers [ncstate46]. Efficient conversion of electrical energy has become more important over the past few decades due to the increasing prices for energy, more restrictive laws and regulations, the upcoming challenges related to the global climate change and the growing relevance of the security of energy [lutz1]. Power semiconductors are active components within the energy conversion system

that can turn on and off the power supply within the converter, either in off-state (forward or reverse-blocking) or in on-state (conducting) [lutz1].

Power electronic converters can be generally divided in the following groups: rectifiers (convert alternate current to direct current), DC to DC converters, AC to AC converters and inverters (convert DC to AC). Power converters should be highly efficient, provide high power densities, have a wide operating temperature range and be low in costs [lutz1].

The development of modern semiconductor devices started with the invention of the thyristor, a silicon controlled rectifier, in late 1957. Subsequently various types of power devices have been developed and made commercially available in the 1970s [sing2]. Since then there have been constant improvements and new inventions, like the power MOSFET (metal oxide semiconductor field-effect transistor) and IGBT (insulated gate bipolar transistor), in this field. The various types of power electronics can be distinguished according to their degree of controllability [sing2]:

- Uncontrolled turn-on and off devices (e.g. diodes)
- Controlled turn-on and uncontrolled turn-off devices (e.g. thyristors)
- Controlled turn-on and off devices (e.g. MOSFETs, GTOs, IGBTs, BJTs) [sing2]

The most common semiconductor for power devices is silicon, other new semiconductor materials like gallium nitride (GaN) are currently under investigation and might provide promising applications in the near-future [lutz1]. Recent advances have been made with silicon carbide (SiC), a material that has a wider band gap than silicon and that might show excellent properties for stable and efficient power electronics. SiC provides high carrier mobility and high electrical and thermal conductivities, thus possibly enabling the production of a new generation of power devices that are more resistant towards higher voltages, temperatures and frequencies [sing2]. The two carbon-based semiconductor materials crystalline silicon carbide and diamond-like carbon (DLC) will be discussed in the following sections in more detail.

2.1.2 Applications of IGBTs and diodes

2.1.2.1 Insulated gate bipolar transistor

The insulated gate bipolar transistor (IGBT) is a three-terminal power semiconductor switch that has been developed in the early 1980s and is used to control electrical energy [rash7]. To a certain degree it has replaced the prior used MOSFETs and bipolar junction transistors. Due to the IGBTs' high cost effectiveness and good switching speed, many new power applications have been realized in the past years and are nowadays economically feasible. Moreover, IGBTs show an enhanced safe operating area, meaning the current and voltage boundary within which the transistor can be operated without damage

[rash7]. IGBTs have been constantly improved during the past few decades, leading to lower energy losses and higher switching speeds. The simplicity of IGBTs facilitates the construction of power electronic circuits and therefore leads to less complex and more cost effective designs. Furthermore, IGBTs provide to some extent protection for the device in case an over-current or short circuit fault occurs [rash7].

The main application of IGBTs is as switching component in inverter circuits in power supply as well as in motor-driven applications [rash7]. Power supply applications include constant voltage, constant frequency power supply, uninterruptible power supply, welders, cutters and medical equipment like CT and X-ray. In the motor drive sector IGBTs are used in variable voltage, variable frequency inverters [rash7].

2.1.2.2 Power Diodes

Diodes are static two-terminal switching devices and have a very simple set-up. Semiconductor diodes may be subdivided into p-n-doped semiconductor crystals and Schottky diodes with a rectifying metal-semiconductor junction. If the diode is forward biased, forward current can flow through the material and only a small voltage drop of less than 1V can be observed. In the case of a reverse bias, the material becomes non-conductive and only small current flows in the reverse direction, the so-called leakage current [rash7].

The primary applications of power diodes are as rectifiers, for voltage clamping and as voltage multipliers. Silicon rectifier diodes show a large forward carrying capability, a high reverse resistance in mega-ohm range, whilst their forward resistance is rather small. They are mainly used in power conversion applications, such as power supply, uninterrupted power supply (UPS), inverters etc. [rash7].

2.1.3 Properties of semiconductors

Semiconductors show various special characteristics, which make them versatile and interesting for their usage in power electronics. By definition, a semiconductor is a solid matter whose conduction band is separated from the valence band by the so-called energy gap E_g [lutz1]. The electrical resistivity of semiconductors lies between that of metals and insulators and covers a wide area from around 10^{-4} to 10^{9} Ω cm. Contrary to metals, the resistivity of semiconductors decreases with temperatures. The degree of conductivity can be controlled over a wide temperature range by doping the material with impurities [lutz1]

When semiconductors are used for power devices, they have to show a sufficiently large band gap, in order to ensure an effective doping structure and high critical field strength [lutz1]. The critical field strength is a measure of the strength of an electrical field that the material can withstand without break-

down and usually increases with the size of the band gap. However, band gaps that are too wide provide some disadvantages for power semiconductor devices, as the built-in and threshold voltages rise and the ionization energies of the impurities become larger. Increasing ionization energies are unfavourable, because as a consequence the amount of free charge carriers being released decreases [lutz1].

In the following subsections a more detailed description of the electrical conductivity of semiconductors, the types of doping and the properties of a pn-junction is provided.

2.1.3.1 Electrical conductivity of intrinsic and extrinsic semiconductors

According to the band gap model of energy levels, the electrical conductivity of a solid depends on its valence band, conduction band and the energy gap in between them [hueb3]. In a conductor like a metal the conduction band is partly filled with electrons and overlaps with the valence band, so that the electrons can move freely through the material and therefore generate a flow of current (cf. Fig. 1, afer [hype58]).

As far as an electrical insulator is concerned, the conduction band is empty, the valence band is fully occupied and the band gap between them is rather big. Due to the lack of free space, the electrons in the valence band cannot rearrange themselves energetically in order to overcome that rather large energy gap, thus no current flow occurs [hueb3].

In a semiconductor material the band gap is much smaller than in an electrical insulator, which enables electrons in the valence band that carry a thermal energy high enough to overcome this barrier and move to the empty conduction band [hueb3].

With increasing temperature the electrical conductivity of semiconductor materials increases because more electrons in the valence band have the energy necessary to overcome the band gap. However, the concentration of electrons in the conduction band is much smaller than in metals, resulting in smaller electrical conductivities of semiconductors [hueb3].

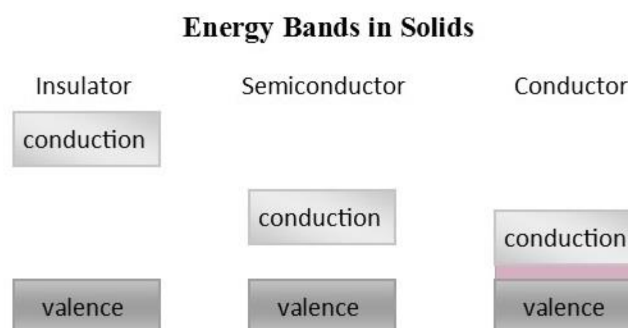

Figure 1: Graphical representation of energy bands in solids, after [hype58]

Basically one distinguishes between intrinsic and extrinsic (doped) semiconductor materials. The term "intrinsic semiconductor" refers to an undoped material whose electrical conductivity derives from the substance itself [hueb3]. Electrons from the valence band are thermally excited to the conduction band and leave back so-called "holes", which correspond to particles of opposite charge. These vacant positions enable a change in the energy distribution of the remaining electrons in the energy band and therefore, the increasing concentration of electrons in the conduction band accompanied by the formation of holes lead to intrinsic conduction. Intrinsic semiconductors usually consist of only one element, such as germanium and silicon from the IV. group, or of several elements, for example binary compounds of the III. and the V. group like GaAs [hueb3].

Regarding modern semiconductor technologies, semiconductors that are doped with foreign atoms in small quantities are more relevant than the intrinsic ones [hueb3]. The reason for this lies in the variability of usable impurity atoms and in the possibility to influence and adjust important factors such as width of the band gap and the concentration of mobile charge carriers. Intrinsic semiconductors have – compared to metals - an extremely low amount of electrons in the conduction band and consequently a high sensitivity of their electrical properties to impurities or defects in the crystal lattice [hueb3].

There are mainly two types of doping mechanisms: p-type and n-type doping. Germanium and silicon are intrinsic semiconductors and have four valence electrons each [hueb3]. N-Type doping means doping them with an element that has five valence atoms, such as phosphorus or arsenic, and therefore providing them an additional electron in the crystal lattice. The excess electrons from the impurity atoms can be thermally excited to the conduction band of the semiconductor, therefore the usage of n-type dopants permits the controlled change of concentration of mobile charge carriers in the energy bands. Doping a semiconductor from the IV. group with an element from the III. group (e.g. aluminium, gallium) – the so-called p-type doping – leads to a depletion of electrons in the host lattice. The missing fourth electron can be replaced by thermal excitation of an electron from the valence band of the semiconductor with simultaneous formation of a hole. The impurity atom remains as negatively charged ion in the host lattice of the semiconductor [hueb3].

2.1.4 Pn-junction and depletion region

The interface between two differently doped regions, namely between a p-typed and an n-typed semiconductor material, is called pn-junction and is one of the basic elements of almost every common semiconductor power device [hueb3] In Figure 2 [lutz1] the pn-juncions in the most common semiconductor devices are displayed. The interface reveals a higher concentration of electrons in the conduction band on the n-doped side and a larger amount of holes in the valence band on the p-doped side. The difference in charge carriers on both sides is being balanced during the establishment of a state

of equilibrium. The electrons migrate from the n- to the p-doped region and at the same time the holes diffuse in the opposite direction [hueb3].

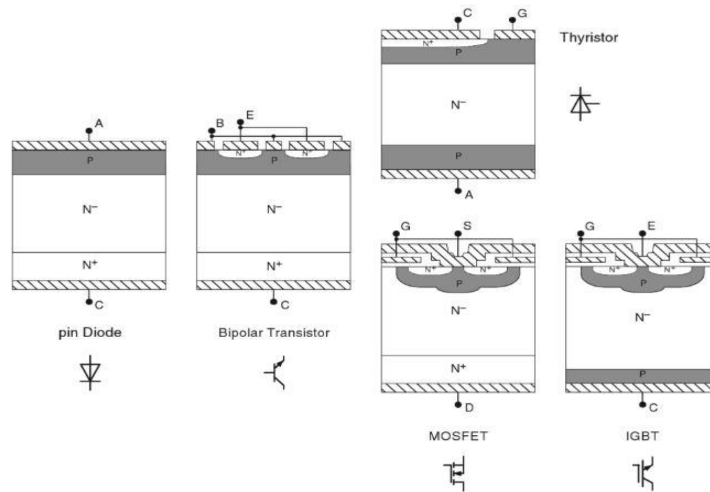

Figure 2: Pn-junctions in the most common semiconductor power devices [lutz1]

This diffusion process at thermal equilibrium leads to the occurrence of some uncompensated donor ions N_D^+ in the n-doped region and some acceptor ions N_A^- in the p-doped region near the pn-junction [dasg4]. Subsequently, a negative space charge (or depletion region) is being formed in the p-region of the material, whilst a positive space charge occurs in the n-region (cf. Fig. 3) [dasg4].

Consequently, this difference in space charge results in a built-in electric field directed from the n- to the p-region, and further causing a drift current in the opposite direction of the diffusion flux of either electrons or holes. At equilibrium, there is no net transport of carriers, as the diffusion species and the drift components are balanced by each other [dasg4]. However, diffusion and drift currents do no longer compensate each other, when an external voltage (called bias voltage) is applied; the pn-junction acts as a rectifier [lutz5]. If the p-region is polarized positively against the n-region, the electrons and holes move through the material towards the pn-junction, providing higher electrical conductivity (cf. Fig. 4 [lutz1]). Due to this forward bias on the junction the current can flow more easily. When the p-doped region is polarized negatively against the n-doped one, a reverse bias is put on the junction. The electrons and holes move away from the pn-junction, leaving behind a layer characterized by a very low electrical conductivity [lutz5]

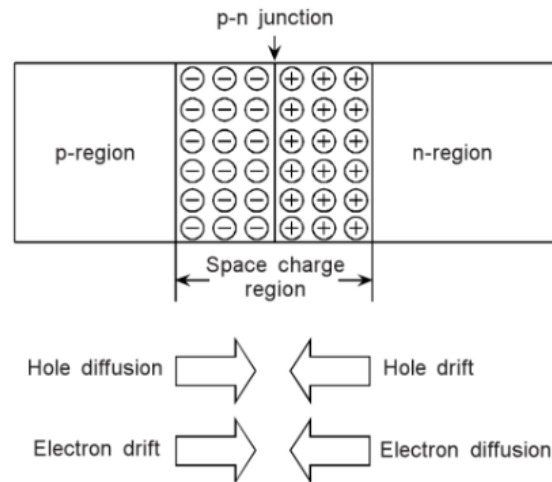

Figure 3: Pn-junction (cf. Semiconductor devices [dasg4]

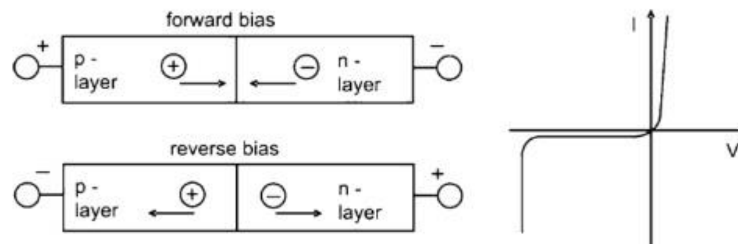

Figure 4: Forward and reverse bias of pn-junction [lutz1]

2.1.5 Challenges in edge-termination design

In silicon power electronics like MOSFETs or IGBTs the p-doped sections are usually produced by implantation and diffusion [knip8]. The planar pn-junctions consist of a coplanar and a curved area. When reverse voltage is applied at the pn-junction, the maximum of the electrical field strength is localized in this curved area for geometric reasons (cf.Fig.5A) [knip8]. Because of that increased field strength the avalanche voltage of the whole chip is lowered, leading to decreased stability and early failure of the final products. Various methods for edge termination design have been developed; on the one hand by covering the semiconductor region with a field plate and on the other by changing the semiconductor area itself by “Junction Terminal Extension” (JTE) or “Variation of Lateral Doping” (VLD) [knip8]

JTE involves a weaker doped p^- area with lateral homogeneous doping directly at the interface of the actual p-region. The same holds true for VLD, with the exception that the doping concentration decreases gradually over the p^- - region (cf. Fig.5B) [knip8]. VLD structures show a high robustness and the required area for the edge termination is reduced [knip8].

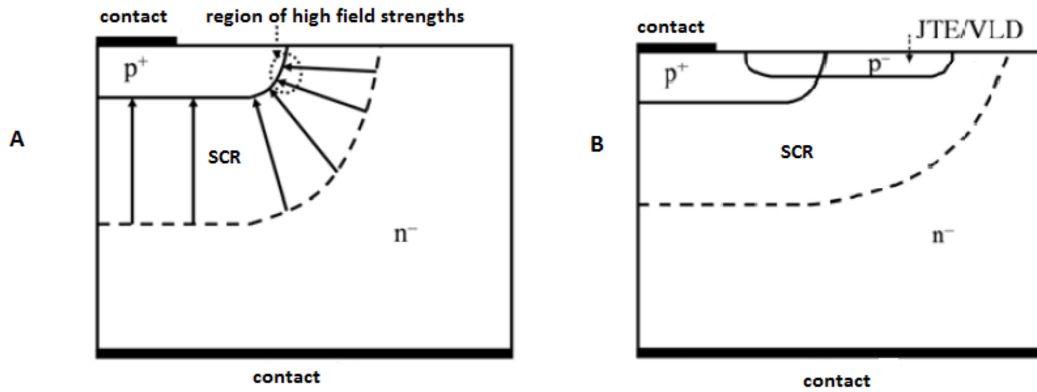

Figure 5: A on the left shows a pn-junction in reverse bias. The space charge region (SCR) expands to the n- area. In the curved area close to the surface an increase in electric field strength occurs. B: pn-junction with JTE resp. VLD as edge termination, after [knip8]

2.1.6 Reliability behaviour and film degradation

Power electronic devices are usually operated up to the limits of tolerable currents, voltages and temperatures [schröd9]. Moreover, the devices often have to face rough ambient conditions like humidity, contamination with extraneous particles and a wide temperature range. Therefore, the manufacturer has to test and ensure their reliability under harsh settings, which are derived from the real operating conditions and intensified in order to accelerate the degradation process [schröd9]. The standard reliability tests for power chips and modules are - amongst others - the following: High temperature reverse bias (HTRB) and high humidity high temperature reverse bias (H3TRB) [lutz1]. The high temperature reverse bias (HTRB) test is conducted on power chip level and loads the samples with the maximum permitted voltage (direct-current voltage) according to the respective voltage class. The chip fails if there is a noticeable increase in reverse current within the time frame of 1000 hours. This setup is used to determine weak spots in the passive layer and the edges, for example contamination with metallic and other types of ions [lutz1].

The high humidity high temperature reverse bias test (H3TRB) is used for evaluation of the impact of humidity on the life-span of power module packages [lutz1]. Furthermore, weaknesses in the passive layer of the chips and degradation processes in the packaging material can be observed. The reverse voltage limit for high blocking voltage elements is set to 80 V, so that the power losses generated by the occurring reverse current do not heat up the chip and therefore locally reduce the relative humidity. For IGBTs the testing environment is given by a set temperature of 85 °C and a relative humidity of 85 %. As in the HTRB tests, the module fails if the reverse current increases over the testing period of 1000 hours [lutz1].

2.1.7 Carbon-based semiconductor materials: Silicon carbide

Crystalline silicon carbide has – depending on the particular polytype – a large bandgap varying between 2,3 to 3,3 eV and is therefore the ideal material for power electronics [lutz1]. In comparison, pure silicon has a bandgap of 1,12 eV at a temperature of 300 K. Crystalline SiC offers some advantages compared to pure silicon, such as a higher maximum operating temperature up to which a sufficient intrinsic carrier concentration is present, and a higher critical field strength at which breakdowns occur. Moreover, in SiC higher doping concentrations at a specific blocking voltage are possible and therefore enabling future development of power devices with low power losses and very high blocking voltages. However, silicon carbide is still more expensive and less versatile than the widely used pure silicon [lutz1].

Silicon carbide consists of silicon and carbon atoms connected via covalent bonds in the form of a tetrahedron (cf. Figure 6) [sadd6]. Because of its short bond length and therefore high bond strength, it provides a high mechanical and chemical stability. There are more than 200 polytypes of crystalline silicon carbide known, originating from the various stacking possibilities of the bilayers of silicon and carbon in different crystal orientations (cubic, hexagonal, rhombohedral) [sadd6].

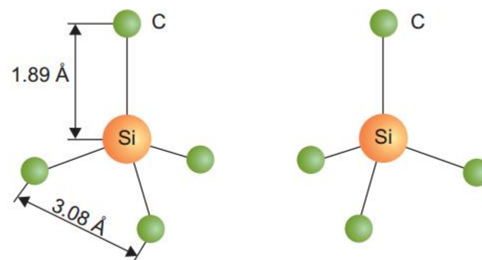

Figure 6: Tetrahedral structure of silicon carbide [sadd6]

Silicon carbide is usually used in electronic switches like transistors and MOSFETs, in micro-electro mechanical (MEM) devices and because of its biocompatibility it is also an interesting material for bioMEMS technology [sadd6].

The most interesting forms of crystalline SiC for technological applications are 4H-SiC, 6H-SiC and 3C-SiC, where the number indicates how many layers are needed in order to form the basic structure and the letter refers to the respective crystal form (C – cubic, H – hexagonal, R – rhombohedric) [sadd6]. The various polytypes of crystalline SiC have different properties and consequently applications. The hexagonal modification 4H-SiC for example has the widest band gap of 3,2 eV and is used in power electronic devices, whilst the 6H-SiC is the ideal material for solid- state lighting applications (LEDs). The 4H- and 6H-SiC variant are processed in bulk form in a high temperature furnace (>2000 °C), the cubic 3C-SiC is usually deposited as thin film [sadd6].

2.2 Carbon-based Thin Films in Power Semiconductor Industry

2.2.1 Carbon- based film types and their applications

2.2.1.1 Diamond-like carbon

Carbon is a highly versatile element that forms a great variety of structures and can exist in three different hybridisations (sp^3, sp^2 and sp^1) [robe10]. The carbon atoms in the allotrope diamond are entirely sp^3 hybridized, so each atom has four tetrahedrally coordinated σ bonds. These strong single bonds are the reason for the extreme properties of diamond, such as outstanding mechanical hardness, chemical inertness, high atomic density and a wide band gap of 5,5 eV [robe10]. Diamond-like carbon (DLC) basically is a meta-stable allotrope of carbon that contains a mixture of sp^3 and sp^2 bonds with a high fraction of sp^3 in an amorphous matrix [zeng11]. The ternary phase diagram of bonding in amorphous hydrogen-carbon alloys was proposed by J. Robertson in 2002 and is shown in Figure 7 [robe10]. The properties of DLC vastly depend on the ratio of sp^2 and sp^3 bonds and furthermore, on the hydrogen content. Hydrogenated DLC shows lower mechanical hardness and wear resistance and is thermally less stable than the hydrogen-free variants [zeng11]. There are two types of DLC, the hydrogenated with a content of hydrogen of up to 60% (a-C:H) and a hydrogen-free one (a-C). When the type of DLC contains a very high fraction of sp^3 bonds then it is called tetrahedral amorphous carbon (ta-C, ta-C:H) [zeng11]. The carbon atoms in graphite however are three-fold coordinated with sp^2 orbitals in stacked monolayers, resulting in a soft and electrically conducting material [robe10].

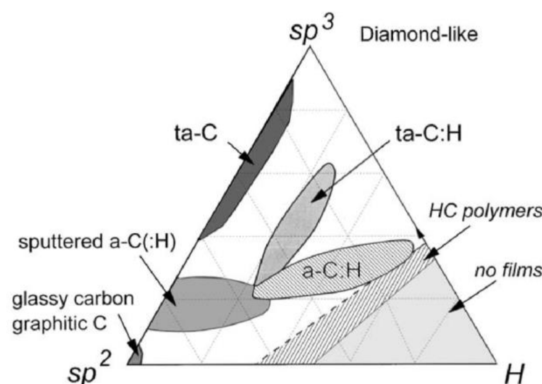

Figure 7: Ternary phase diagram of the bonding situation in amorphous carbon hydrogen alloys [robe10]

The choice of deposition method has a great impact on the obtained type of DLC and the final properties of the thin films. Typical methods include plasma-enhanced chemical vapour deposition (PECVD) for a-C:H, pulsed laser deposition for ta-C with a sp^3 C fraction of up to 70%, high plasma density PECVD for ta-C:H and sputtering for a-Cs [zeng11].

Thin films of DLC are used as protective coatings for optical windows, magnetic storage disks, in biomedical applications and for micro-electromechanical devices (MEMs). The main advantage of DLC films with a high content of sp^3 bonds is that they show similar beneficial properties as diamond, while at the same time being a lot cheaper to produce [robe10]. Typical deposition methods include plasma-enhanced chemical vapour deposition (PECVD), pulsed laser deposition, high plasma density PECVD and sputtering [zeng11].

2.2.1.2 Amorphous silicon carbide

Amorphous silicon carbide (a-SiC) is a tetrahedral alloy of silicon and carbon with no long-range order of the atomic network [janz12]. It has lower hardness than the crystalline form, but shows remarkable corrosion resistance because of its lack of line and planar defects [li13].

Thin films of a-SiC are durable coatings with a high wear resistance and high dielectric properties (K ~ 4,6) [sadd6]. Because of the amorphous microstructure and the low deposition temperatures used, the films are in general highly insulating due to the wide band gap [sadd6]. Moreover, other characteristics are a high melting point, good electron mobility and high thermal conductivity [hura14]. Thin films a-SiC are used as composite materials in various semiconductor devices, for example in colour sensors, metal-insulator-semiconductor structures and light emitting diodes [jung15]. A-SiC is highly compatible with silicon regarding adhesion and can therefore easily be incorporated in silicon-based microfabrication technology, such as MEMS, sensors and actuators [ili16]. Furthermore, thin films of a-SiC are used as diffusion barriers, passivation layers and barrier layers, for example in amorphous silicon solar cells [pern17].

However, the specific electrical, optical and mechanical properties are dependent on the respective deposition method and set of parameters [sadd6]. Other factors influencing the properties and network of a-SiC are hydrogen content, precursor gases and the C/Si ratio. Layers deposited from methane and silane at temperatures below 600 °C contain a significant amount of hydrogen. An elevated carbon content might lead to the formation of clusters with graphitic configuration [janz12]. The typical deposition techniques for a-SiC are explained in more detail below.

In edge termination structures, a-SiC can serve as electroactive layer [schmidt63]. An exemplary semiconductor device with edge termination comprises of a semiconductor body with pn-junction and VLD region (cf. Fig. 5B), a contact electrode on the surface and a passivation layer on top. The passivation stack consists of one amorphous semi-insulating layer and two adjoining nitride layers, such as silicon nitride (Si_3N_4). Power semiconductor devices can block high voltages in the range of several 100V or even several kilovolts, which leads to high electric fields in the semiconductor body. The

surfaces of the semiconductor body are very sensitive to degradation effects that may reduce the voltage blocking capability and thus require an adjoining protective layer [schmidt63].

A-SiC thin films are not only used to passivate the semiconductor body, but may also act as electroactive layers that affect the potential distribution along the semiconductor surface [schmidt63]. Furthermore, a-SiC exhibits remarkable mechanical hardness of about 21 GPa (according to Vickers) and a Young's modulus of about 110 GPa, which results in increased mechanical protection of the semiconductor body. The additional nitride layers are relatively hard and chemically inert and therefore, provide for mechanical protection of both a-SiC film and semiconductor body. The second nitride layer covers potentially present defect regions of the first nitride layer [schmidt63].

2.2.2 Deposition techniques for amorphous silicon carbide thin films

The mechanical and electrical properties of a-SiC are widely dependent on the deposition technique and conditions. The most common deposition methods for thin films of a-SiC are pulsed laser deposition (PLD), magnetron sputtering and chemical vapour deposition (CVD) [sadd6].

Pulsed laser deposition uses a high-energy laser beam that strikes the silicon carbide target material and vaporizes small amounts of it [sadd6]. The target material is deposited from the generated plasma onto the substrate. A disadvantage of this method is the slow deposition rate, however very smooth thin films of a-SiC can be produced. Sputtering involves the bombardment of the target material in a vacuum with ions from a plasma and the ensuing deposition of the ejected target atoms onto the substrate. An advantage is that sputtering can be performed at temperatures close to room temperature [sadd6].

During chemical vapour deposition, a mixture of volatile gases is heated in order to be decomposed into individual atomic species, which subsequently solidify on the surface of the substrate. CVD is a very versatile process with the drawback of high deposition temperatures compared to other techniques [sadd6].

The a-SiC thin films on the silicon wafers used for this master thesis were deposited using radio-frequency (RF) plasma-enhanced CVD; therefore this chapter will focus on this technique in more detail.

Chemical vapour deposition involves the reaction of vaporized chemicals which form the thin film on a substrate [xia18]. The reaction usually happens on or above the temperature controlled surface and the gaseous reactants can be activated by various means; typically being chemical, thermal, plasma or photon energy. In semiconductor industry a wide variety of amorphous or glassy thin films are produced by chemical vapour deposition, for example silicon based (SiC, SiN, SiO_2) or metal based materials (tungsten, titanium nitride). The advantages of this method are step coverage, high material throughput, reliable performance and high cost effectiveness [xia18].

The typical CVD reaction steps are shown in Figure 8 [xia18]. The mechanism involves introducing the reaction and carrier gases into the reactor (A) and then activating the gas species by heat, plasma etc. (B). Subsequently, the reactive species are adsorbed on the substrate (C) and form a solid thin film (D). The last two steps involve desorption of by-products from the substrate (E) and their following removal from the reactor (F). Hereby, the most critical reaction step is the formation of the solid film on the surface [xia18].

The chosen method for activating the gas species basically depends on the respective reaction and the used gaseous precursors [xia18]. Some reactions are very fast and might even be explosive, such as a mixture of silane and O_2 or tetraethyl orthosilicate (TEOS) and ozone. In those cases high density plasma deposition (HDP) or sub-atmospheric CVD (SACVD) are used as deposition methods. In other cases the reactions are rather slow and need additional activation energy, like for example the deposition of silicon nitride based on the precursors silane and NH_3. The required additional energy can be provided by using PECVD [xia18].

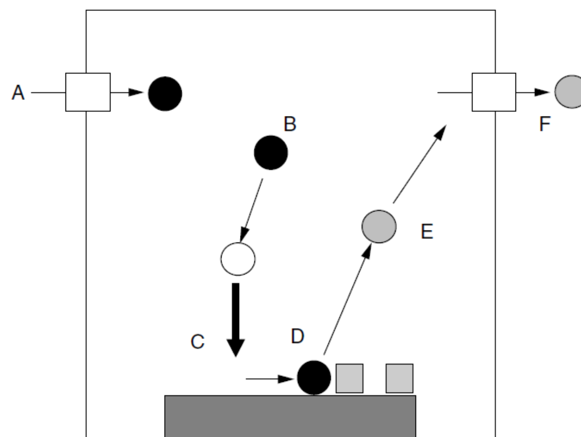

Figure 8: CVD reaction steps: Introduction of the reaction and carrier gases into the reactor (A), followed by the activation of the gas species by heat, plasma etc. (B). Adsorption of the reactive species on the substrate (C) and formation of a solid thin film (D). The last two steps involve desorption of by-products from the substrate (E) and their following removal from the reactor (F) [xia18].

In PECVD less reactive precursor gases are used in order to avoid unwanted reactions in the gas phase [xia18]. The plasma creates high-energy forms of the reactants by dissociating the precursor gases. When using plasma as activating energy form, the reaction rates can be increased while at the same time the process temperature can be decreased [xia18]. The typical setup for a PECVD system with RF plasma is shown in Figure 9 [lnf59].

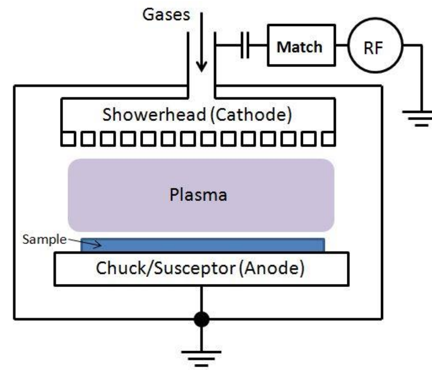

Figure 9: PECVD system [lnf59]

The plasma contains charged species such as electrons and ions and their energy depends on the RF configuration, which involves the type of cathode or anode used, the ground geometry and the RF frequency [xia18]. Therefore, the surface of the substrate is not only bombarded with the active precursors, but also with charged species, leading to a modification of the deposited thin film. The operating temperature is used to control the surface of the substrate and the bulk diffusion of the active species. Both RF configuration and process temperature have a major impact on the final properties of the thin films, including morphology, structure, stress, density and impurities. Films deposited by PECVD usually are of smaller grain size or more amorphous than with other CVD techniques. Moreover, the films tend to have a certain amount of impurities, such as hydrogen [xia18].

Despite the versatility of the method and the possibility to modify the film properties, one major drawback of CVD with RF plasma is that the charged species from the plasma might cause the embedment of charge in the resulting films or uneven charge effects in the final power devices [xia18]. This obstacle can be overcome by using a remote plasma source, which has no direct contact to the substrate. The reactants are dissociated remotely and subsequently transported to the substrate, where they react with second reactants to form a solid film [xia18].

For the deposition of a-SiC thin films a carbon-based and a silicon-based precursor is needed. For PECVD usually silane (SiH_4) and methane (CH_4) are used as reactants and hydrogen or helium as dilution gases [sadd6]. A main advantage of this technique is the low deposition temperature, which usually ranges between 200 and 400°C for a-SiC layers, since it must be well under the melting point of the respective substrate and as far as MEMS applications are concerned, the overall thermal budget of the fabricated device should be kept low [ili16].

Other advantages of PECVD of a-SiC films include stress control depending on the deposition conditions, the large mechanical strength of the layers and the suitability of the final devices for relatively high operating temperatures. Moreover, a-SiC deposited by PECVD has a similar thermal

expansion coefficient as pure silicon, therefore reducing the risk of high internal stress and delamination of the thin films from the Si substrates [ili16].

2.2.3 Characterization of thin films

An important part in thin film deposition processes is quality control by monitoring the properties of the resulting films. Those properties include amongst others the film thickness, stress, the optical bandgap, the refractive index n and extinction coefficient k. A change in those properties without a change in the applied deposition parameters indicates equipment failure or alteration of the deposition conditions.

In this chapter Fourier transformed infrared spectroscopy (FTIR) for identifying molecular components and structures, optical characterization methods for determining film thickness and optical constants and the curvature method for stress measurements will be introduced. Furthermore, the Tauc plot analysis, which is used to estimate the width of the optical bandgap of amorphous materials, will be discussed.

2.2.3.1 Intrinsic stress behaviour

Thin films deposited on wafers usually underlie either compressive or tensile residual stresses. Stress at room temperature equals the sum of intrinsic and extrinsic stresses [fran31]. Extrinsic stress originates in the difference in thermal expansion coefficients of wafer and film, whilst intrinsic stress depends on the respective microstructure of the film and on the deposition process. Tensile stress has a positive value by convention and corresponds to elongation. The thin film however is attached to a substrate and will cause the wafer to bend by trying to regain its original size. The result is a concave shape of the substrate and film and when the stress is too high it will lead to cracking of the film. Compressive stress has a negative value and will force the film and wafer in a convex shape. Too high compressive forces may lead to buckling of the film [fran31].

The stress of a thin film on a wafer can be determined by measuring the wafer curvature with either optical techniques or stylus profilometers. The curvature of the substrate is measured before and after film deposition. Then the stress is calculated by the so-called Stoney formula [fran31]:

$$\sigma = \frac{E_s}{6(1-\nu)} \frac{t_s^2}{t_f} \left(\frac{1}{R} - \frac{1}{R_0}\right)$$

where E_s is Young's modulus of the substrate, t_s and t_f correspond to thickness of each substrate and film, ν is the Poisson ratio of the substrate (0,27 for silicon) and R_0 and R are the radius of curvature before and after film deposition [fran31].

2.2.3.2 Infrared spectroscopy

Fourier transformed infrared spectroscopy (FTIR) is especially suited for the identification and quantification of carbon-containing molecules and is furthermore a cost-effective and rapid analysis technique [janz12]. It uses non-visible light with wavelengths between 2,5 and 16 µm. Depending on the respective structures of the molecules in the sample, they absorb specific frequencies of the light and then transform this absorbed energy to vibrational motion (e.g. rocking, stretching). In contrast to rigid ionic bonds, the nuclei joined by covalent bonds can move or vibrate in a characteristic way [janz12].

Fourier transformation is a mathematical method that translates signals in the time domain into the frequency domain and is used to enhance sensitivity of the IR measurements. The resulting spectra are IR absorption spectra that contain a substance-specific fingerprint. Computerized comparison with standard IR libraries allows fast routine analysis of the spectra [janz12].

2.2.3.3 Optical measurement techniques

The thickness of thin films is usually measured with an incident beam of light as probe and determined by the interference between reflected and transmitted light. This interference can either be constructive or destructive and involves amplitude as well as phase information [wool19]

Optical measurement techniques do not measure the parameters of interest directly, but rather another quantity that is a function of the respective parameters. Based on the known parameters (e.g. wavelength of incident beam of light) a model is developed. The values of the unknown parameters are estimated and then varied until they fit the model to the measured data [wool20]. In the following, the optical measurement techniques used for characterizing the samples in this thesis will be explained briefly.

Spectral ellipsometry

Ellipsometry is a non-destructive, sensitive measurement technique that is used to characterize thin films, surfaces and microstructures [wool20]. It uses polarized light and determines the relative phase change in the beam of reflected or transmitted light of a sample. For the analysis of simple samples ellipsometry measurements at a single wavelength can be used. However, spectral ellipsometry provides more information about a sample because the optical constants vary with the wavelength [wool20]. The refractive index n is defined as the ratio of the velocity of light in vacuum to the one in the respective medium. Its dependence on the frequency of the incident light beam is called dispersion, which is present in all optical materials [fox60]. The frequency-dependent extinction coefficient k corresponds to the energy loss of an electromagnetic wave propagating through a medium, for example due to scattering or free carrier absorption [kasa61].

This technique is most commonly used for determining film thickness of thin films and the optical constants n and k in the wavelength ranges of UV, visible and IR. It works best for smooth and uniform thin films with a thickness in the order of nanometres to microns [wool20]. A sketch of an ellipsometry measurement is shown in Figure 10.

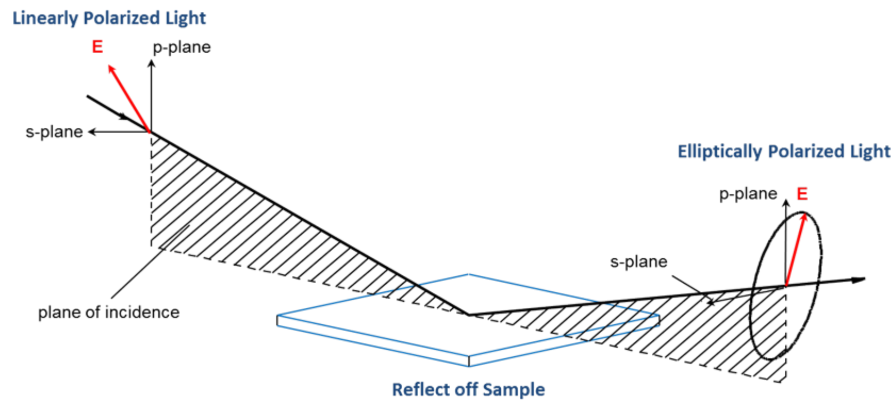

Figure 10: Sample ellipsometry measurement (source: J.A. Woollam Co.)

The polarization state of the incident light beam can be described by two orthogonal basis vectors, the so-called p- and s-directions. The p-direction lies in the the plane of incidence, while the s-direction is perpendicular to it. Ellipsometry is interested in the output polarization and therefore in the change of the p- and s-components in relation to each other of the light beam upon reflection or transmission [wool20].

A modification of this technique is beam profile ellipsometry (BPE), where the incident light beam is focused on a sample by using a high numerical aperture lens and, resulting in a spread of different angles of incidence [opsal32].

Beam profile reflectometry

Beam profile reflectometry (BPR) measures the angular reflectance of a polarized light beam of a fixed wavelength on a wafer [dieb33]. The light beam is focused with a high power microscope objective on only a small spot on the sample (cf. Fig. 11), reflected and detected in two detector arrays parallel and perpendicular to the polarization direction. By detecting the changes in the profile of the reflected beam film thickness, refractive index and extinction coefficient can be determined simultaneously [dieb33].

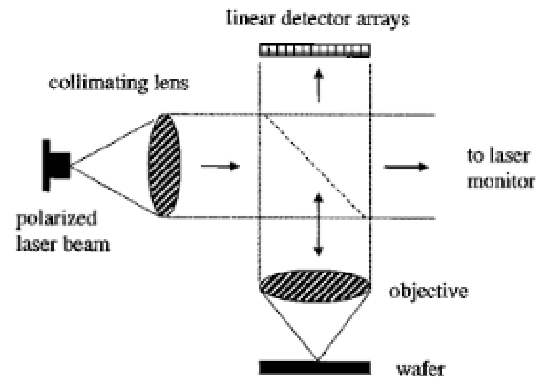

Figure 11: Setup for Beam Profile Reflectometry [dieb33]

2.2.4 Tauc plot analysis

The optical band gap or Tauc gap E_g of amorphous materials can be determined by analysing the optical measurement data of a sample with the so-called Tauc plot, which was originally developed for amorphous silicon. The model is based on the following equation [janz12]:

$$\sqrt{\alpha \hbar\omega} = B(\hbar\omega - E_g)$$

α = absorption coefficient

ħω = E = photon energy

B = Tauc slope

The Tauc plot is a plot of the photon energy E against $\sqrt{\alpha E}$ [flew35] and the Tauc gap E_g is being determined by fitting the linear region of the plot and extrapolating it to the intersection with the x-axis. The Tauc plot can be used to analyse in how far the optical band gap of a material depends on the respective deposition parameters [janz12].

The Tauc plot for hydrogenated amorphous silicon (a-Si:H) is shown in Fig. 12 [flew35]. The drawbacks of this method are the low accuracy due to the fitting step and the need to adapt the model to the particular amorphous sample material as it was developed for amorphous silicon [janz12].

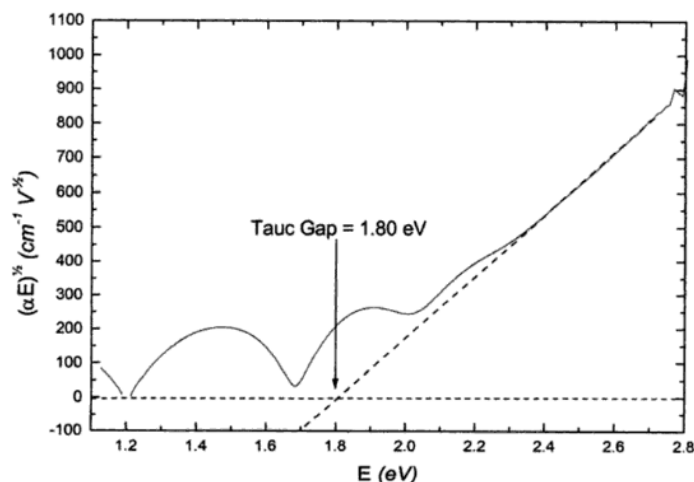

Figure 12: Tauc plot for hydrogenated amorphous silicon [flew35]

2.3 Electrochemical corrosion measurement techniques

2.3.1 Basics of corrosion

The term corrosion generally refers to the degradation of materials due to their interactions and reactions with their surroundings. Corrosive environments mostly are liquid or gaseous, like for example marine atmosphere, but solid-solid corrosion reactions are possible as well [stans21]

Controlling and minimizing corrosion is important because of safety and economic reasons. Material failures due to corrosion might lead to injuries or even death and involve significant costs for restoration and repair. The spendings for corrosion control usually are a compromise between benefits of reducing materials failure and economic feasibility [stans21].

There are many possible corrosion mechanisms, depending on the type of material and the specific environment in which it is being used. In general, corrosion is a transport process, which involves atoms, molecules or ions and happens at the interface of a material. The overall reaction rate of the corrosion process is determined by the slowest reaction step [stans21]. One of the various causes of corrosion is the change in Gibbs free energy ΔG, which indicates the tendency for any given reaction to take place or not. The more negative the value of ΔG, the more likely the chemical reaction will occur [revie22].

The process of corrosion cannot be measured or observed directly on a molecular scale; therefore its mechanisms usually are determined by indirect analytical methods [stans21]. These methods involve the observation of change in weight or dimensions, of the build-up of corrosion products, of changes in mechanical or physical properties or of changes on the surface by optical microscopy. As far as electrochemical corrosion is concerned, the relevant measurement parameters are the changes in electrical potential and current due to the corrosion process [stans21].

The type of corrosion mechanism depends on the form of the specific material, such as ceramics, polymers and metals, and therefore on the type of mass transport along the material interface and can be chemical, physical or electrochemical [stans21]. For an environment that is able to take up ions and an electron conducting material the corrosion mechanism is electrochemical. The most important case of electrochemical corrosion is the degradation of metals in aqueous solutions, where the metal becomes oxidized and enters the aqueous environment in ionic form. The released electrons migrate through the metal and are consumed by a substance in contact with the metal [stans21].
Chemical corrosion leads to breaking of bonds and hence to degradation of material properties, changes in the molecular structure and possibly the transfer of corrosion products to the material's environment [stans21]. Physical corrosion is the result of a mechanical action of the surroundings on the material, for example removing protective films or breaking the material [stans21]. When physical attacks are the cause of the degradation of material, it is not called corrosion but rather erosion or wear. In some cases physical attacks do not occur alone but are accompanied by chemical reactions, like in corrosion-erosion or fretting corrosion. However, the causes of corrosion processes and damage are mostly electrochemical processes [revie22].

2.3.2 Electrochemical corrosion

Generally electrochemical corrosion is based upon a redox reaction system [ahmad23]. The elemental requirement for this type of corrosion to occur is the formation of a corrosion cell, including an anode, a cathode, an electrolyte and electron and current flow. As mentioned above, the material should be electron conducting and the environment should be able to take up ions. Anodic and cathodic regions might occur within the same material and on the same object, depending on the respective sites. The basic outline of a corrosion cell is shown in Figure 13 [ahmad23]. The anode is the negative terminal of the cell where the oxidation of the material occurs. Due to the oxidation electrons are released and move through the material to the cathode. Electrons are insoluble in aqueous solutions and can therefore not be taken up by the electrolyte [ahmad23].

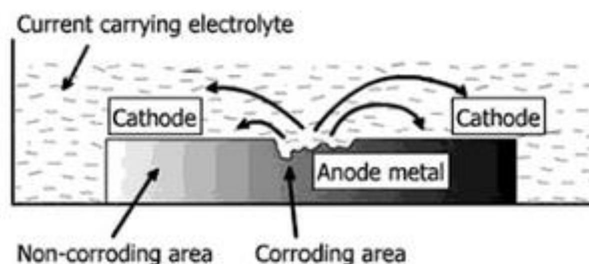

Figure 13: A basic corrosion cell [ahmad23]

The cathode is the positive terminal of the cell and where the reduction reaction occurs. The electrons released at the anode are consumed at the cathode. The electrolyte has to be an electrically conductive

solution (e.g. salt dissolved in water). Positive current flows through the electrolyte in form of cations from the anode to the cathode, while electrons pass through the metallic path from the negative to the positive terminal of the cell in order to complete the circuit [ahmad23].

The environment of the material plays an important role in corrosion, as it has influence on the occurrence, the reaction rate and the degree of the degradation of the material [ahmad23]. Different geographic locations have different impacts on the severity of corrosion damages, depending on substances and contaminations in the atmosphere and the variation in moisture and temperature. The marine environment is considered to be the most corrosive in nature because of its high relative humidity and the high concentration of atmospheric contaminants. Other corrosive environments are damp and wet atmospheres, acids, brines and industrial atmospheres. Humidity is a problem because thin invisible films of moisture are formed on the surfaces and make a good electrolyte in combination with residual salts. Moreover, visible water layers like dew and rain drops can be problematic as they form small corrosion cells. The difference to corrosion in aqueous solutions is that only a limited quantity of water is present, but also an unlimited supply of oxygen from the air is given. Furthermore, during atmospheric corrosion the corrosion products are formed close to the surface of the material and therefore might act as a physical barrier to further degradation [ahmad23].

The equilibrium state between a material and its surroundings is described by thermodynamics [revie22]. Corrosion occurs when this equilibrium is disturbed and the system tends towards establishing a new one with a specific reaction rate, the so-called corrosion rate. Therefore, thermodynamics as well as kinetics of the electrochemical reactions should be studied in corrosion science [revie22]. The basic concepts of thermodynamics and kinetics of corrosion will be outlined in the following two subchapters, aiming to provide a better understanding of the underlying mechanisms as well as the later described corrosion measurement techniques that were used for this thesis.

2.3.2.1 Thermodynamics of corrosion

The tendency for any given chemical reaction to occur is described by the change in Gibbs free energy ΔG [ahmad23]. Both enthalpy H and entropy S are indicators of the feasibility of a reaction at constant temperature and pressure, however they act in opposite directions. A negative value for the enthalpy and an increase in entropy implicate a spontaneous course of the reaction. According to the second law of thermodynamics, the Gibbs free energy expresses the relationship between enthalpy, entropy and temperature of a chemical reaction and is a driving force for it to occur [ahmad23]:

$$\Delta G = \Delta H - T\Delta S \tag{2.1}$$

A negative value for ΔG indicates a tendency for the reaction to take place spontaneously, a positive one implicates that the reaction will not start without activation. However, the Gibbs free energy does

not provide any insight into the kinetics of the reaction, meaning that the reaction rate can be either high or small depending on various factors [revie22]. The kinetics of corrosion reactions will be discussed in the following subchapter.

The probability of a reaction to occur can also be described by the electromotive force (EMF), which represents the sum of two half-cell potentials of a cell. The greater the value of EMF, the more likely the reaction will start. The relationship between the electromotive force and the free energy is described by the following equation [revie22]:

$$\Delta G = -n * F * E \qquad (2.2)$$

ΔG ….. Gibbs free energy [J]

n ..... Number of electrons in reaction

F ….. Faraday constant = 96485 [J/mol]

E ….. electromotive force [V]

Considering a basic reaction for a galvanic cell (equ. 2.3), the corresponding ΔG is given by the difference in the molal free energy of products and reactants [revie22]:

$$\boldsymbol{lL + mM -> qQ + sS} \qquad (2.3)$$

$$\boldsymbol{\Delta G = \left(qG_Q + sG_S\right) - \left(lG_L + mG_M\right)} \qquad (2.4)$$

When each species is in standard state, the standard molal free energy (G°) is used [revie22]:

$$\boldsymbol{\Delta G° = \left(qG°_Q + sG°_S\right) - \left(lG°_L + mG°_M\right)} \qquad (2.5)$$

The difference between the free energy for species L in any given state and the standard state is related to the activity of L, a_L as shown in equation 2.6, with R being the gas constant (8,314 J/molK) and T being the absolute temperature in Kelvin [revie22].

$$l(G_L - G°_L) = lRTlnL = RTln\, a_L^l \qquad (2.6)$$

If equation 2.5 is subtracted from equation 2.4, the following formula is obtained [revie22]:

$$\Delta G - \Delta G° = RT\, ln\, \frac{a_Q^q * a_S^s}{a_L^l * a_M^m} \qquad (2.7)$$

At equilibrium ΔG equals to zero and the reaction will not occur. The equilibrium constant K is defined as follows [revie22]:

$$K = \frac{a_Q^q * a_S^s}{a_L^l * a_M^m} \quad (2.8)$$

Therefore, the standard Gibbs free energy can be expressed in relation to the equilibrium constant [revie22]:

$$\Delta G° = -RT \ln K \quad (2.9)$$

$$\Delta G° = -nFE° \quad (2.10)$$

If the terms for ΔG and ΔG° in equation 2.7 are replaced by E and E° from equations 2.9 and 2.10, the so-called Nernst equation shall be obtained, which expresses the value of the electromotive force of a cell with regard to the activities of the products and reactants of the respective cell [revie22]:

$$E = E° - \frac{RT}{nF} \ln \frac{a_Q^q * a_S^s}{a_L^l * a_M^m} \quad (2.11)$$

For an electrochemical reaction the Nernst equation has the following form [ahmad23]:

$$E = E° - \frac{RT}{nF} \ln \frac{reduced\ state\ activities\ product}{oxidized\ state\ activities\ product} \quad (2.12)$$

2.3.2.2 Corrosion kinetics

Electrode kinetics examines the reaction rates at the interface between electrode and electrolyte and helps to understand corrosion mechanisms [revie22]. An electrode is not at equilibrium when there is a net current flow to or from its surface, leading to a change in the measured potential depending on the intensity of the current and its direction.
The shift from the equilibrium as well as the flow of current opposes the direction of the potential change. This potential change is called polarization of the electrode [revie22].

A general distinction is made between three types of electrochemical polarization [caff24]:

- Activation polarization

  Slow electrode reactions cause the polarization of the electrode. For example, electrons are supplied faster to a platinum electrode than they can react with H^+ ions, resulting in an increase of the electron concentration at the interface. As a result the electrode potential is shifted to more negative values [caff24].

- Concentration polarization

  The polarization is caused by the changes in the concentration of reactants and products near the electrode surface [caff24].

- Ohmic polarization

  It is caused by a drop of internal resistance in the solution or across surface films. Ohmic drop occurs in the electrochemical measuring cell because the reference electrode cannot be placed directly at the surface of the sample [caff24].

The so-called overpotential η characterizes the degree of the polarization as it is defined as the electrode potential E for a given current minus the open-circuit potential E_0 at zero current flow [caff24]:

$$\eta = E - E_0 \tag{2.13}$$

The cathode as well as the anode can be polarized. Cathodic polarization shifts the electrode potential in a negative, anodic in a positive direction [caff24].

In the following sequence the electrode kinetics for activation polarization shall be discussed. Considering a metal species M in aqueous solution at equilibrium, both oxidation and reduction of M occur at the same reaction rate [caff24]:

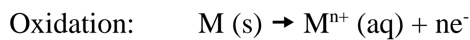
Oxidation: $M (s) \rightarrow M^{n+} (aq) + ne^-$

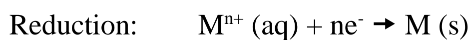
Reduction: $M^{n+} (aq) + ne^- \rightarrow M (s)$

At equilibrium the cathodic current density of the reduction reaction j_c equals the anodic current density of the oxidation reaction j_a [caff24]. In Figure 14 the polarization diagram of species M is shown [ahmad23]. The rate of reaction j_0 in either direction at equilibrium potential (open-circuit potential) is called the exchange current density [caff24]:

$$j_a = j_c = j_0 \tag{2.14}$$

At open-circuit potential the net rate of the total reaction is zero [caff24]:

$$j_{net} = j_c - j_a = 0 \tag{2.15}$$

This is the reason why the open-circuit potential E_0 can be measured directly, but not the exchange current density itself. It can be determined indirectly by disturbing the system and shifting it to non-equilibrium states [caff24].

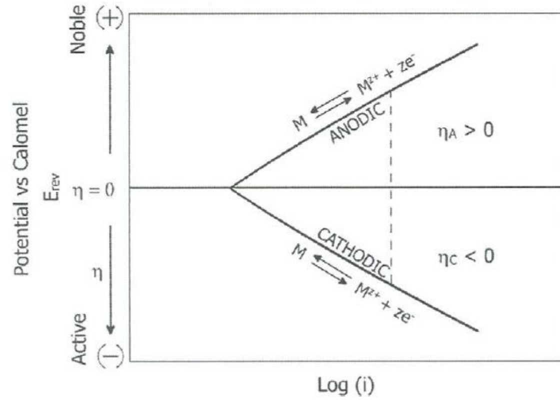

Figure 14: Polarization diagram of species M [ahmad23]

In activation-controlled reactions the free energy barrier has to be overcome in order for the reaction to start. When the electrode potential is being changed from its equilibrium state E_0 to another value, the free energy barrier $\Delta G^{\neq}$ is affected by that change and either raised or lowered (cf. Figure 15). Furthermore, the height of the free energy barrier has an impact on the reaction rate of the respective reaction [caff24].

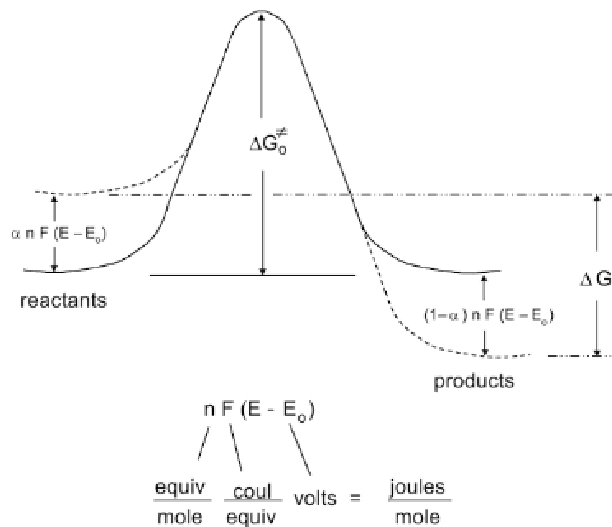

Figure 15: The impact of the change of the electrode potential on the free energy barrier [caff24]

When the electrode potential change results in a decrease of the free energy barrier, the following equation can be applied:

$$\Delta G^{\neq} = \Delta G_0^{\neq} - \alpha nF (E-E_0) \tag{2.16}$$

$\Delta G_0^{\neq}$ ….. free energy barrier at E_0

α ….. dimensionless symmetry factor between 0 and 1

The parameter α defines the extent of the modification of the symmetry of the free energy barrier by the electrode potential change. The degree of the decrease in the free energy barrier in the forward direction equals its increase in reverse direction when α takes on a value of 0,5 [caff24].

At non-equilibrium state the overall current i [A] in the corrosion cell corresponds to the difference of the cathodic current i_c [A] and the anodic current i_a [A] [zoski25]:

$$i = i_c - i_a \tag{2.17}$$

Both anodic and cathodic current are proportional to their corresponding heterogeneous rate constants; k_f stands for the forward reduction reaction and k_b for the backward oxidation electrode reaction [zoski25]:

$$i_c = FAk_f C_O(0,t) \tag{2.18}$$

$$i_a = FAk_b C_R(0,t) \tag{2.19}$$

A ….. electrode area [cm²]

C_Z (x,t) ….. concentration of species Z at distance x [cm] from the electrode at time t [s]

The forward as well as the reverse reaction rate constant can be written in relation to the standard heterogeneous rate constant k^0 [cm/s] [zoski25]:

$$k_f = k^0 e^{[-\alpha F(E-E_0)]/RT} \tag{2.20}$$

$$k_b = k^0 e^{[(1-\alpha)F(E-E_0)]/RT} \tag{2.21}$$

Dividing these two expressions of the rate constants, an equation that describes all types of electrode kinetics models is obtained [zoski25]:

$$\frac{k_b}{k_f} = e^{\frac{F(E-E_0)}{RT}} = e^{-(E-E_0)\kappa T} \tag{2.22}$$

κ ….. Boltzmann’s constant [J/K]

Combining the equations 2.17 - 2.21 results in the complete current-potential characteristic [zoski25]:

$$i = FAk^0[C_O(0,t)e^{-\frac{\alpha F(E-E_0)}{RT}} - C_R(0,t)e^{\frac{(1-\alpha)F(E-E_0)}{RT}}] \qquad (2.23)$$

At equilibrium state the exchange current i_0 can be expressed as [zoski25]:

$$i_0 = FAk^0 {C^*}_0^{(1-\alpha)} {C^*}_R^{\alpha} \qquad (2.24)$$

C^*_0 ….. bulk concentration of oxidized species [mol/cm³]

C^*_R ….. bulk concentration of reduced species [mol/cm³]

However, the exchange current can also be determined experimentally by extrapolation of the linear regions of anodic and cathodic slope in the Tafel plot, as can be seen in Figure 16 [zoski25]. Tafel plots are described in greater detail in the subsequent chapter "Electrochemical polarization with Tafel plot analysis".

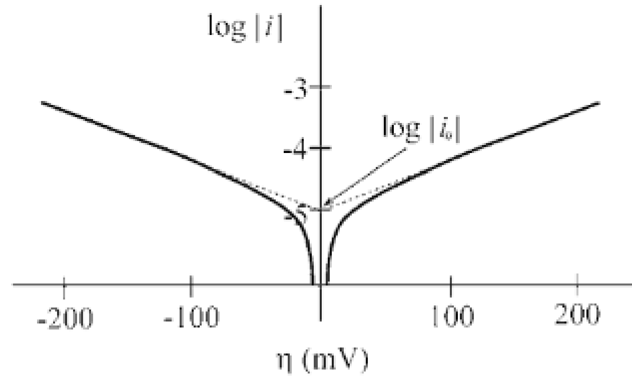

Figure 16: Typical Tafel plot [zoski25]

When equations 2.23 and 2.24 are combined, the current-overpotential equation is obtained [zoski25]:

$$i = i_0[\frac{C_0(0,t)}{C^*_0}e^{-\frac{\alpha F\eta}{RT}} - \frac{C_R(0,t)}{C^*_R}e^{\frac{(1-\alpha)F\eta}{RT}}] \qquad (2.25)$$

Assuming an efficient degree of mass transfer where the concentration of the solution at the electrode surface and of the bulk solution are equal, equation 2.25 can be reduced to the so-called Butler-Volmer equation [zoski25]:

$$i = i_0[e^{-\frac{\alpha F\eta}{RT}} - e^{\frac{(1-\alpha)F\eta}{RT}}] \qquad (2.26)$$

The Butler-Volmer equation is used to predict the overall current i of the cell as a function of the over-potential [zoski25].

After having discussed the theoretical background of electrochemical corrosion and corrosion kinetics, the next subchapters provide a detailed description of two widely used electrochemical techniques for corrosion studies. Electrochemical polarization with Tafel plot analysis is a direct current method, whilst electrochemical impedance spectroscopy (EIS) is an alternate current technique. Both are powerful methods and provide insight into complex corrosion mechanisms. Moreover, experimental design and the obtained results from the corrosion studies will be discussed.

2.3.3 Polarization measurements and Tafel extrapolation

The corrosion stability of the a-SiC samples used for this thesis were characterized with polarization measurements and EIS. Tafel extrapolation is applied for interpreting the results from polarization measurements and for calculating the corrosion rate of the respective sample.
In this chapter, the basic concepts of polarization measurements and Tafel extrapolation are described in order to provide an insight into the main features, the advantages as well as the limitations of this corrosion measurement technique.

In electrochemical corrosion measurements, the open-circuit potential OCP is also referred to as corrosion potential E_{corr} [ahmad23]. At this potential, the surface corrodes freely without any impressed current. At E_{corr} the rate of the reduction reaction equals the rate of the oxidation and the current is called corrosion current i_{corr}. The corrosion current corresponds to the exchange current that has been discussed in the previous section and cannot be measured by conventional methods.

However, in corrosion studies it is very favorable to determine the corrosion current as it can be used to calculate the corrosion rate of the material in the specific medium and therefore allow comparisons of corrosion stability between different materials [ahmad23].
The corrosion current determination is carried out by measuring the corrosion potential first, subsequently performing polarization measurements and finally doing Tafel plot analysis. The polarization measurements are carried out with a three-electrode arrangement in an electrochemical measuring cell, whereby the test material acts as the working electrode [ahmad23].
Starting from E_{corr} an over-potential of around 300 mV is impressed in positive direction for anodic polarization as well as in negative direction for the cathodic polarization, the occurring current is recorded [ahmad23].
At sufficiently large over-potentials in either direction, only the reduction or the oxidation reaction takes place. In Figure 17 a theoretical (actual) and an experimental (measured) polarization curve for a corroding metal species M are shown [ahmad23].

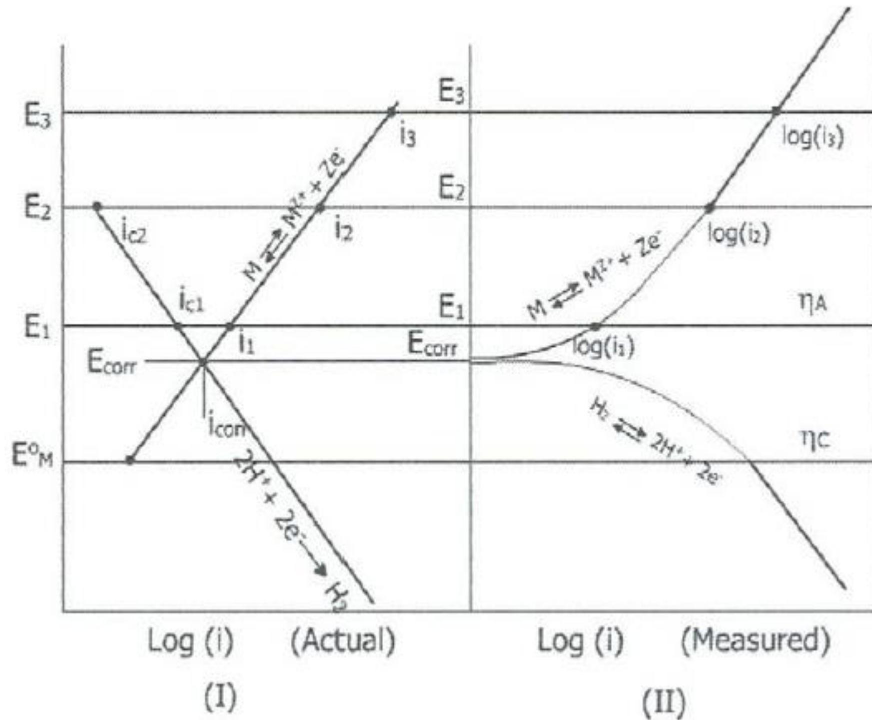

Figure 17: Comparison of actual and measured polarization curves [ahmad23]

In the actual polarization diagram the corrosion potential occurs at the intersection between anodic and cathodic curve [ahmad23]. For the experimental polarization curve the corrosion potential has to be measured and plotted in the diagram. Impressing the potentials E_1, E_2 and E_3 in the positive direction from the corrosion potential, the lines intersect the anodic curve at i_1, i_2 and i_3. At point E_3 the current becomes completely anodic. Shifting the potential in a negative direction to E_1, E_2 and E_3, the cathodic polarization curve with the currents i_{c1} and i_{c2} is obtained.

The experimental polarization curve in Figure 17 does not show the same linear behaviour as the theoretical one, but linear regions above 50 mV > E_{corr} and asymptotic behaviour in the region near E_{corr} [ahmad23].

As can be seen in Figure 17 [ahmad23], the corrosion current i_{corr} cannot be read directly from the measured polarization diagram. Therefore the Tafel extrapolation method is used, where the linear regions of the polarization curves are extrapolated to an intersection at E_{corr} in order to yield i_{corr}. A hypothetical Tafel plot of a metal species M with the extrapolated regions of anodic and cathodic curve is shown in Figure 18 [ahmad23].

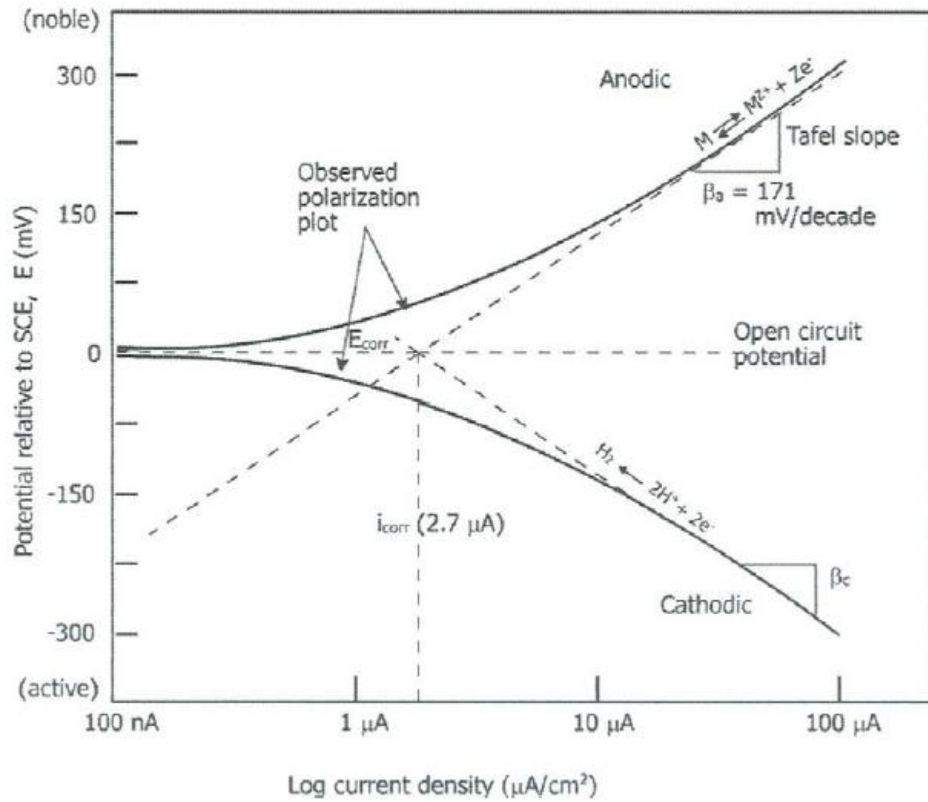

Figure 18: Hypothetical Tafel plot [ahmad23]

The Tafel equation links the applied over-potential to the resulting current that flows through the circiuit and can be used to calculate the exchange current i_0, which corresponds to the corrosion current [zoski25]:

$$\eta = \frac{RT}{\alpha F} \ln i_0 - \frac{RT}{\alpha F} \log i \qquad (2.27)$$

The Tafel equation can also be reduced to a simpler form; however its utility is limited due to diffusion and the reverse reaction [zoski25]:

$$\eta = a + b \log i \qquad (2.28)$$

a…. constant

b….. Tafel slope

The determined value of icorr can be used to calculate the rate of corrosion by means of Faraday's law, which relates the total charge that is passed through a circuit to the amount of reaction product [zoski25]:

$$Q = nFN \qquad (2.29)$$

Q …. total charge passed through circuit [A]

n ..... number of electrons transferred per mole of product

N …. amount of product [mol]

F ….. Faraday constant = 96485 C/mol

The current I corresponds to the change in charge with time and the amount of product in moles can be calculated with the molar mass and the mass in grams [zoski25]:

$$i = \frac{dQ}{dt} \qquad (2.30)$$

$$N = \frac{m}{M} \qquad (2.31)$$

M ….. molar mass [g/mol]

m ….. mass [g]

By combining equations 2.29 – 2.31, the following formula is obtained [ahmad23]:

$$m = \frac{1}{F}\frac{M}{n}\, it \qquad (2.32)$$

The Faraday constant F indicates the amount of electricity required in order to deposit the ratio of mass to the valency of a substance. The corrosion rate R_{corr} is proportional to the current passed and depends on the molar mass of a substance. Its dimension is the change of mass per time unit [ahmad23]:

$$corrosion\, rate = \frac{dm}{dt} \qquad (2.33)$$

Combining equations 2.23 and 2.24 and replacing current i by the corrosion current [ahmad23]:

$$corrosion\, rate = \frac{dm}{dt} = \frac{M\, i_{corr}}{nF} \qquad (2.34)$$

In the corrosion analysis of thin films a corrosion rate R_{corr} in the unit [mm/year] is more applicable:

$$m = Ad\rho \qquad (2.35)$$

$$R_{corr} = \frac{dd}{dt} = \frac{Mi_{corr}}{nFA\rho} * 3{,}1536 * 10^{7} \qquad (2.36)$$

A ….. area [mm²]

d ….. thickness of the film [mm]

ρ ….. density of the material [g/mm³]

2.5.4 Electrochemical impedance spectroscopy

Electrochemical impedance spectroscopy is a fast and non-destructive method for the evaluation of the electrochemical corrosion stability of a wide range of materials, along with coatings, anodized films and corrosion inhibitors [hamd62]. As described in more detail later on in chapter 4, the proposed corrosion mechanism of a-SiC is mainly of electrochemical nature and thus, electrochemical corrosion measurements were chosen in order to investigate the material degradation process.

EIS is a technique that measures the impedance of an electrochemical system over a predefined range of frequencies. The general approach is to apply an alternating current potential to a system and measuring the current response [silv26] (cf. Figure 19 [lvov28]). In a linear system the current response to a sinusoidal potential at a certain frequency is expected to be also sinusoidal, but with a phase shift [silv26].

EIS is a versatile electrochemical technique that has been receiving increased recognition in scientific research over the past few years [metr27]. The main applications of EIS are characterization of materials and corrosion phenomena regarding coatings, batteries and fuel cells. Moreover it is used for studying semiconductor interfaces and investigating mechanisms in electro-deposition, electro-dissolution, and passivation [metr27].

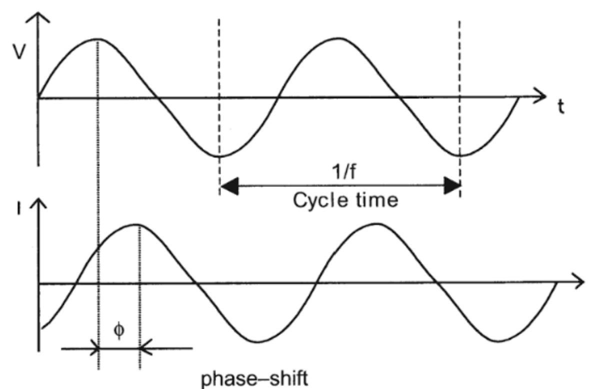

Figure 19: Sinusoidal input voltage V (above) and resulting current response I (below) at a single frequency [lvov28]

First, the concept of impedance and the theoretical background of electrochemical impedance spectroscopy will be discussed. Furthermore, it will be shown how the measured data is graphically presented and described by equivalent circuit models.

According to Ohm's law, the electrical resistance is a measure of the ability of a circuit element to resist the flow of electrical current and is described as ratio between input voltage and current response [lvov28]:

$$R = \frac{V}{I} \tag{2.37}$$

However, the resistance is only applicable to an ideal resistor, at which it is independent of AC frequency and the input and output signal are in phase with each other [lvov28]. In contrast, the impedance term includes the phase shift between input voltage and output current as it consists of two parts: the real and the imaginary one. The real impedance corresponds to the Ohmic resistance, whilst the imaginary part is related to the ability of the system to store electrical energy. Therefore, impedance can be regarded as complex resistance that applies to alternate as well as direct currents and to circuits containing different elements, like resistors, capacitors and inductors [lvov28].

In EIS experiments an excitation AC voltage signal V of small amplitude V_A is applied at a certain frequency f. The voltage signal expressed as a function of time gives the following relationship [lvov28]:

$$V(t) = V_A \sin(2\pi f t) = V_A \sin(\omega t) \tag{2.38}$$

The parameter ω stands for the radial frequency in rad/s [lvov28]:

$$\omega = 2\pi f \tag{2.39}$$

The response current is shifted in phase φ, depending on the ratio of its respective capacitive and resistive components, and has an amplitude I_A [lvov28]:

$$I(t) = I_A \sin(\omega t + \varphi) \tag{2.40}$$

Based on 3.1 and 3.2, an equation analogous to Ohm's law can be expressed for impedance Z [lvov28]:

$$Z^* = \frac{V_t}{I_t} = \frac{V_A \sin(\omega t)}{I_A \sin(\omega t + \varphi)} = |Z| \frac{\sin(\omega t)}{\sin(\omega t + \varphi)} \tag{2.41}$$

Plotting the response current against the applied voltage gives the so-called Lissajous Figure (cf.Fig. 20A [lvov28]), which used to be the subject of analysis prior to modern instrumentation and methods.

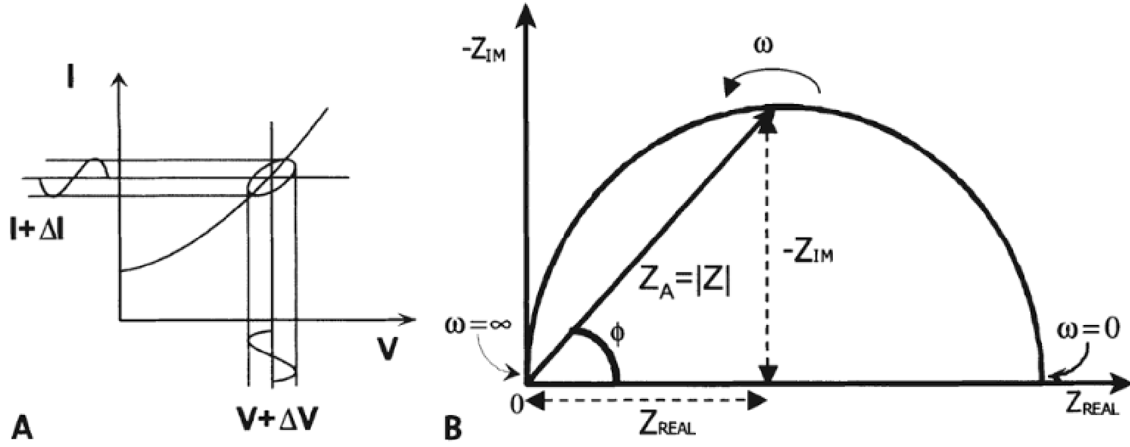

Figure 20: A Lissajous Figure; B Nyquist plot [lvov28]

Based on Euler's relationship:

$$\exp(j\varphi) = \cos\varphi + \mathrm{j}\sin\varphi \tag{2.42}$$

the impedance can be expressed as complex function. Input voltage and current response can be described as follows [lvov28]:

$$V(t) = V_A e^{j\omega t} \tag{2.43}$$

$$I(t) = I_A e^{j\omega t - j\varphi} \tag{2.44}$$

In 2.45, the impedance is expressed in terms of complex mathematics as a combination of a real and an "imaginary" component [lvov28]:

$$Z^* = \frac{V}{I} = |Z|\, e^{j\varphi} = |Z|\,(\cos\varphi + j\sin\varphi) = Z_{real} + j\, Z_{im} \tag{2.45}$$

The phase shift φ at a specific radial frequency ω can be described as the ratio of the real and imaginary part:

$$\tan\varphi = \frac{Z_{im}}{Z_{real}} \tag{2.46}$$

$$\varphi = \arctan\frac{Z_{im}}{Z_{real}} \tag{2.47}$$

The graphical representation of equation 2.45 is shown in Fig. 20B [lvov28]. This form of data presentation is called Nyquist plot, at which the imaginary part of the impedance is plotted against the real one. Each point on the curve conforms to the impedance at a single frequency. As shown in Fig. 20B, the impedance can be represented as vector of the length of its absolute value and with the phase

shift φ as the angle between vector and x-axis. One major drawback of the data presentation using Nyquist plots is that it cannot be seen at which frequency the impedance was measured [gamry29].

Another common type of graphical EIS data presentation does show frequency information, the so-called Bode plot [gamry29]. Hereby the absolute values of Z or the phase shift are plotted against the logarithm of the frequency (cf. Figure 21 [gamry29]). The shapes of the Nyquist and Bode plots depend on the underlying equivalent circuit model and its respective elements. The plots shown in the Figures 20B and 21 are derived from a very simple equivalent circuit model that contains only one time constant (resistance and capacitance element in parallel). Nyquist plots often consist of a part of one or of several semicircles [gamry29].

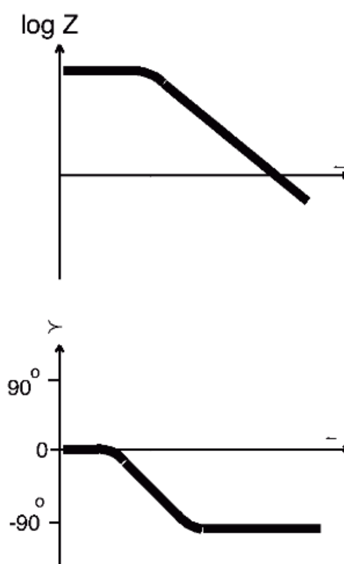

Figure 21: Examples for Bode plots [gamry29]

The electrical equivalent circuits and their elements will now be discussed in more detail [gamry29]. Data from EIS measurements is usually analysed by fitting to equivalent circuit models that consist of various electrical elements, such as resistors, capacitors and inductors. The common circuit elements, their impedance and current/voltage relationship are shown in Table 1 [gamry29].

Table 1: Common circuit elements [gamry29]

Element	Current vs voltage	Impedance
Resistor	**E = IR**	**Z = R**
Inductor	**E = L di/dt**	**Z = jωL**
Capacitor	**I = CdE/dt**	**Z = 1/ jωC**

L….. inductance [H]

C….. capacitance [F]

The resistor has no imaginary component and therefore its impedance Z is independent of the frequency [gamry29]. The current through a resistor is not shifted in phase compared to the input voltage. Most

equivalent circuit models contain a resistor element for the solution resistance between reference and working electrode. It corresponds to the intercept with the x-axis at high frequencies in the Nyquist plot and can be determined by fitting the experimental EIS data to a model [gamry29]. An inductor only has an imaginary component and its impedance increases as the frequency is raised. The current response is shifted -90° in phase compared to the input voltage. In a capacitor the current is phase-shifted 90° in respect to the voltage and the impedance decreases with increasing frequency [gamry29].

In order to fit the obtained experimental data, it has to be distinguished whether the elements are arranged in series or in parallel. Both can occur within the same circuit [gamry29].

In series: $Z_{eq} = Z_1 + Z_2 + Z_3$

In parallel: $\frac{1}{Z_{eq}} = \frac{1}{Z_1} + \frac{1}{Z_2} + \frac{1}{Z_3}$

Besides from the solution resistance, there are several typical equivalent circuit elements being used for fitting EIS data, which will now be introduced briefly.

Two common electrical analogues of the capacitance are the double layer capacitance C_{dl} and the coating capacitance C_c [gamry29]. A capacitor consists of two conducting plates that are separated by a non-conducting medium (dielectric). The value of the capacitance C is dependent on the dielectric constant ε_r of the respective medium, the surface of each plate A and the distance d between them [gamry29]:

$$C = \frac{\varepsilon_0 \varepsilon_r A}{d} \qquad (2.48)$$

ε_0 ….. vacuum permittivity

A substrate with an undamaged coating usually has high impedance and its capacitance changes as the coating starts absorbing water [gamry29]. This change in coating capacitance can be measured by means of electrochemical impedance spectroscopy. A typical equivalent circuit for an undamaged coating consists of the solution resistance and of the coating capacitance, as shown in Figure 22 [gamry29].

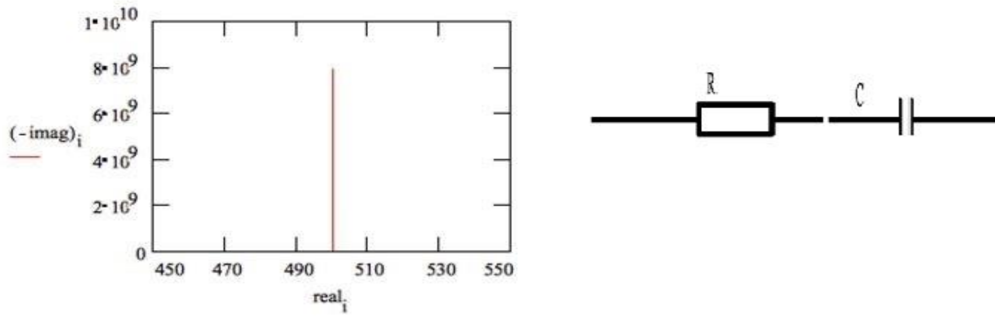

Figure 22: Nyquist plot and equivalent circuit for an undamaged coating [gamry29]

An electrical double layer is formed when ions from the electrolyte solution adsorb onto the surface of the electrode. An insulating space separates the charged electrode from the ions, leading to the formation of a capacitor. The value of the double layer capacitance is dependent on the temperature, the ionic concentration in the solution, the electrode potential, oxide layers etc. [gamry29].

In EIS measurements capacitors often do not behave ideally and therefore have to be modeled as constant phase elements (CPE). There have been several theories regarding this deviation, such as surface roughness or non-uniform current distribution, but the real reasons are still not clear. The impedance of a capacitor is being described by the following formula [gamry29]:

$$Z = \frac{1}{(j\omega)^{\alpha} C} \tag{2.49}$$

For an ideal capacitor the exponent α equals 1, for a CPE it has a value of less than 1 [gamry29].

Diffusion in the cell creates an impedance that is called Warburg impedance and appears as diagonal line with a slope of 45° on a Nyquist plot [gamry29]. At high frequencies the diffusing reactants only have to move a short distance and therefore the Warburg impedance is small. At small frequencies the reactants have to diffuse a longer way, leading to an increase in Warburg impedance.

In the case that semi-infinite diffusion is the rate-determining step and the solution resistance is the only other cell impedance, the resulting Nyquist and Bode plots have the typical shapes as shown in Figure 23 [gamry29].

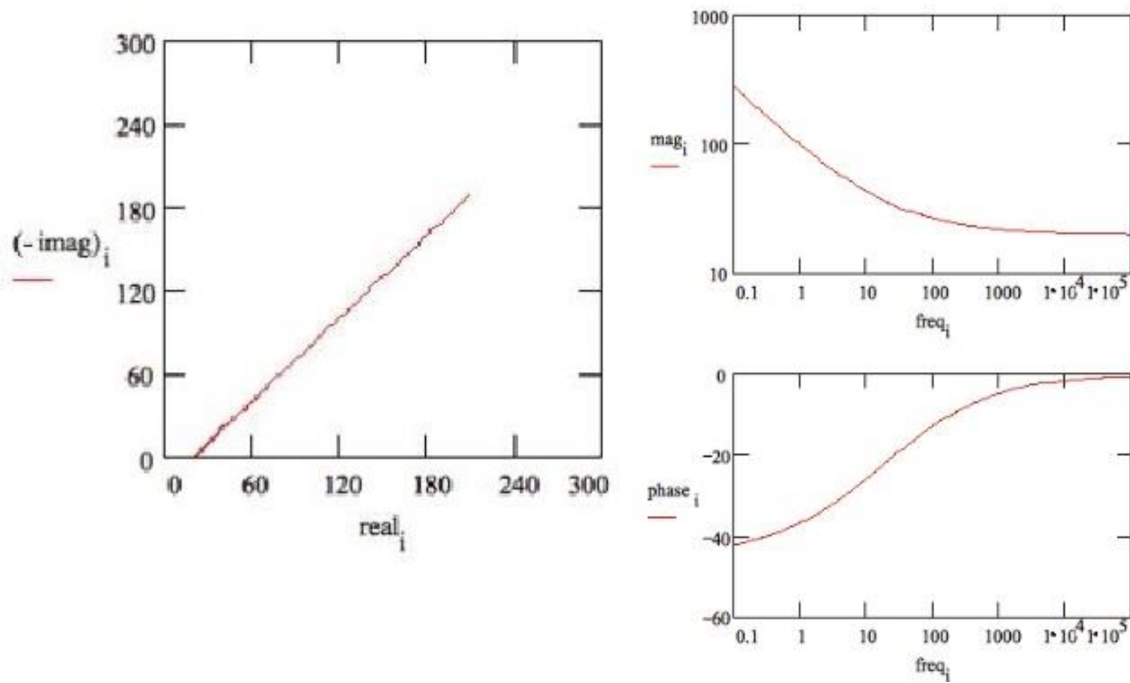

Figure 23: On the left Nyquist plot, on the right Bode plots of Warburg impedance [gamry29]

The most important circuit element for corrosion science is the so-called charge transfer resistance R_{ct}, which is formed by a single kinetically controlled electrochemical reaction [gamry29]:

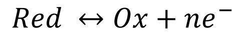

$$Red \leftrightarrow Ox + ne^{-}$$

The investigated material undergoes an electrochemical reaction when it comes in contact with an electrolyte solution and starts dissolving. This process involves the transfer of charge between electrode and electrolyte and its reaction rate depends on the temperature, the applied potential, the concentration of reaction products and on the type of reaction. The greater the sample's resistance to charge transfer, the more stable it is against corrosion [gamry29].

The most common equivalent circuit model is the Randles circuit, which can be used for modelling uniform corrosion and is the starting point for more complex models. It consists of the resistance of the solution, a double layer capacitor and the charge transfer resistance (cf. Fig. 24. [gamry29]).

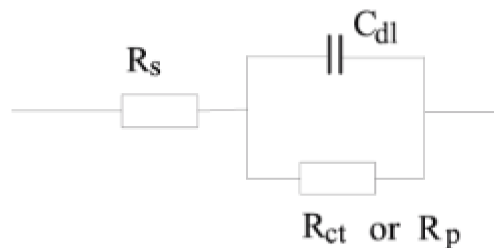

Figure 24: Equivalent circuit for Randles cell [gamry29]

Its Nyquist plot has always the shape of a semi-circle, as shown in Fig. 25 [metr30]. The intercept with the real axis at high frequencies corresponds to the solution resistance, the intercept at low frequencies equals the sum of solution and charge transfer resistance [gamry29].

The replacement of the capacitance by a constant phase element results in a decrease of the semi-circle in height, as shown by the blue semi-circle in Fig. 25 [metr30].

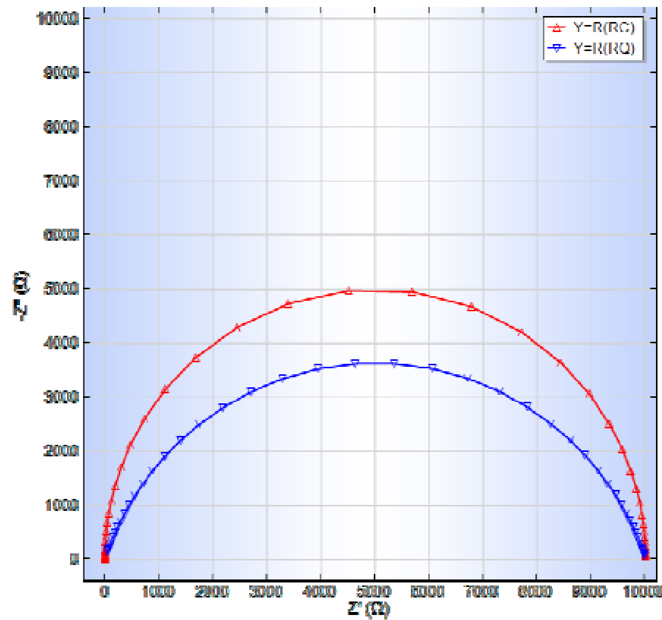

Figure 25: Nyquist plot of a randles cell [metr30]

3. Experimental

3.1 Sample preparation and thin film deposition

3.1.1 Samples for investigating the influence of deposition parameters on thin film properties and corrosion behaviour

Wafers: Crystalline silicon, p-type (boron), 1,9 – 3 mΩ*cm
Oxide layer after etching / before thin film deposition < 5 nm
Backside metallization: 300 nm Ti, 200 nm NiV, 200 nm Ag

The wafer substrates and the respective thin films used for this thesis are listed in Table 2. Silicon wafers without any thin film coating are referred to as "blanks" and their surfaces only consist of a few nanometres of native silicon oxide. For PECVD a single-wafer platform from Applied Materials Inc., USA, with remote RF plasma source was used. The precursor gases for the standard deposition of amorphous silicon carbide were silane (SiH_4) and methane (CH_4). Helium was used as dilution gas and the heater temperature was set to 400 °C.

Table 2: Silicon wafers coated with a-SiC thin films with varying PECVD conditions

Lot number	Wafer number	Shortcut	Film thickness [nm]	RF power/ wafer area [W/cm²]	Variation of
VE628564	#17	Blank	0	-	
	#09	a-SiC LP	300	1,11	RF power
	#10	a-SiC ST	300	1,59	
	#11	a-SiC MP	300	2,07	
	#16	a-SiC HP	300	2,55	
VE642365	#6	a-SiC 100 nm	100	1,59	Film thickness
	#8	a-SiC 300 nm	300	1,59	
	#10	a-SiC 500 nm	500	1,59	
VE642365/ VE669293	#21/#30	silane/methane gas flow ratio 0,11	300	1,59	Stoichiometry
	#22/#33	silane/methane gas flow ratio 0,12	300	1,59	
	#23/#36	silane/methane gas flow ratio 0,13	300	1,59	
	#24/#39	silane/methane gas flow ratio 0,14	300	1,59	
	#25/#42	silane/methane gas flow ratio 0,15	300	1,59	

3.1.2 Samples for investigating the influence of the deposition chamber and heat treatment on the corrosion behaviour of the thin films

Wafers: Crystalline silicon, p-type (boron), 3 – 8 mΩ*cm
Oxide layer after etching / before thin film deposition < 5 nm
Backside metallization: 300 nm Ti, 200 nm NiV, 200 nm Ag

For plasma-enhanced chemical vapour deposition two deposition chambers with the same mainframe from Applied Materials Inc. (USA) were used. One was set up with a CxZ chamber and the other one with a Mark II chamber. The deposition parameters and used precursor gases were the ones for the standard a-SiC deposition as listed in section 3.1.1, with an RF power density of 1,59 W/cm². All other process conditions are tabulated in Table 3. Two of them underwent a heat treatment (annealing) after thin film deposition with the following conditions:

1. **15 minutes at 420 °C**
2. **65 minutes at 380 °C**

Table 3: Silicon wafers with a-SiC coating deposited in two different chambers, with and without heat treatment (ht)

Lot number	Wafer number	Shortcut	Thin film thickness [nm]	Annealing
VC058588	#25	Blank	0	no
	#16	a-SiC CxZ	300	no
	#19	a-SiC CxZ ht	300	yes
	#21	a-SiC Mark II ht	300	yes
	#23	a-SiC Mark II	300	no

3.1.3 Samples for testing the corrosion behaviour of silicon oxides and nitride

Wafers: Crystalline silicon, p-type (boron), 1,9 – 3 mΩ*cm
Oxide layer after etching / before thin film deposition < 5 nm
Backside metallization: 300 nm Ti, 200 nm NiV, 200 nm Ag

The wafers listed in Table 4 were coated with either silicon oxide or an a-SiC/ NIT layer combination.

Table 4: Summary of the used silicon oxide and nitride coatings

Wafer number	a-SiC film thickness [nm]	Type of coating	Precursors	Film thickness [nm]	Deposition method
18	0	SiO_2	TEOS, O_2, He	300	PECVD
19	0	SiO_2	SiH_4, N_2O	300	PECVD
20	0	SiO_2	SiH_4,O_2, Ar	300	PECVD, HDP
21	0	SiO_2	SiH_4,O_2, Ar	300	PECVD, STI
22	0	polymeric SiC	SiH_4, CH_4	300	PECVD
23	100	nitride (NIT)	N_2, SiH_4, NH_3	400	PECVD
24	100	nitride (NIT)	N_2, SiH_4, NH_3	800	PECVD
25	300	nitride (NIT)	N_2, SiH_4, NH_3	400	PECVD

3.2 Film characterization

3.2.1 Stress measurements

The residual stress of the thin films was being determined by optical measurements of the wafer curvature before and after the layer deposition, using a model of the MX series of E+H metrology GmbH (Germany).

3.2.2 Fourier Transform Infrared Spectroscopy

The infrared spectra were recorded using a Bio-Rad FT-IR Spectrometer model QS-500 (Bio-Rad Laboratories Inc., USA).

3.2.3 Optical measurements

Two different optical metrology systems were used to characterize the a-SiC thin films; Opti-Probe 5240 and n&k Olympian. Film thickness, refractive index, extinction coefficient and Tauc gap (or band edge) are the chosen parameters for quality and process control.

The metrology tool Opti-Probe 5240 of the former company Therma-Wave Inc. (now KLA-Tencor Corporation, USA) integrates five different wavelength-based and angle-based optical measurement techniques. In order to characterize extremely thin films and complex film stacks, a single wavelength ellipsometer and a spectroscopic ellipsometer are employed [entre36]. A visible spectrometer and a broadband spectrometer are used to cover the whole wavelength of ultraviolet and visible light in the range between 190 and 840 nm [photo37]. A thermoelectrically cooled diode laser that works with a fixed wavelength of 675 nm is used for the beam profile reflectometry (BPR) and the beam profile ellipsometry (BPE) mode. For the spectrometry mode in the visible light range of 450 to 840 nm a

tungsten halogen lamp is used [entre36]. Spectroscopic ellipsometry is used to determine the optical components of a thin film, while BPR provides information about the film composition and BPE about the film thickness [photo37]. A few years back, an algorithm that is based on the Tauc gap model has been implemented in the software of one of the company-owned Opti-Probe units in order to provide automated determination of Tauc gap and slope for process control.

The metrology tool n&k Olympian (n&k Technology Inc.,USA) is a scatterometer and thin film metrology system that operates at a wavelength range between 190 and 15000 nm. It is used for measuring the thickness of thin and thick films, determining the values for refractive index (n) and extinction coefficient (k) over the whole wavelength range, calculating the energy band gap and generating trench profiles [olymp44].

In the following the measurement tools will be referred to as N&K and Optiprobe.

3.3 Electrochemical corrosion measurements

The electrochemical corrosion measurements Tafel plot analysis and electrochemical impedance spectroscopy were conducted with the following equipment and settings:

- Potentiostat / galvanostat: Autolab PGSTAT128N with an FRA32M module for impedance analysis (Metrohm Autolab B.V., The Netherlands)
- Software: Nova Version 1.10.5 (Metrohm Autolab B.V., The Netherlands)

Three-electrode-arrangement:

- Working electrode: specimen coated with thin film
- Counter electrode: platinum electrode
- Reference electrode: Ag/AgCl electrode, 3 M KCl

Figure 26: The measuring station with potentiostat on the left and electrochemical cell on the right

Tafel plot analysis:

OCP determination: dE/dt limit = 1E-06 V

Working electrode mode: potentiostatic

Working electrode current range: 1 mA

Start potential: -0,250 V

Stop potential: 0,250 V

Step potential: 0,00100 V

Scan rate: 0,0010000 V/s

Based on the data determined with Tafel plot analysis, the software Nova calculated the corrosion rates with the following formula and then converted it to the unit [mm/year]:

$$R_{corr} = \frac{M}{nFA\rho}\, i_{corr}$$

R_{corr} = corrosion rate [cm s^{-1}]

i_{corr} = corrosion current [A]

M = 28,085 g mol^{-1} (atomic weight of silicon)

A = 0,5027 cm² (surface area of sample)

ρ = 2,336 g/cm³ (density of silicon)

n = electrons exchanged in reaction

F = 96485 C mol^{-1} (Faraday constant)

Electrochemical Impedance Spectroscopy:

Working electrode mode. potentiostatic

Set potential: open circuit potential

Frequency scan:

Frequency range: 100000 – 0,01 Hz

Number of frequencies: 50

Frequency step: logarithmic

Amplitude: 0,01 V

Software for equivalent circuit modelling: ZView® (Scribner Associates Inc., USA)

Designing the electrochemical cell:

The first challenge of the electrochemical corrosion measurements was to design a suitable electrochemical cell and a specimen holder for the wafer samples. The front side of the wafer is coated with the respective thin film and must be in contact with the electrolyte solution. The wafer specimen serves as working electrode and thus a rear-side contact to the potentiostat must be given. The electrolyte container has to fit the three electrodes and the electrolyte and its geometry has to be designed in a way that dead spots where no electrolyte exchange occurs are minimized.

A 50 ml polypropylene jar with a centered hole of 8 mm in the bottom for mounting the wafer specimen was used for the first test measurements. The wafer specimen was placed directly on the hole of the jar (front-side up) with a lid beneath it.

Based on this first demonstrator a machined electrochemical cell was designed. Figure 28 shows the technical drawings. Its schematic cross-section is shown in Figure 27; a picture of the actual cell is presented in Figure 29.

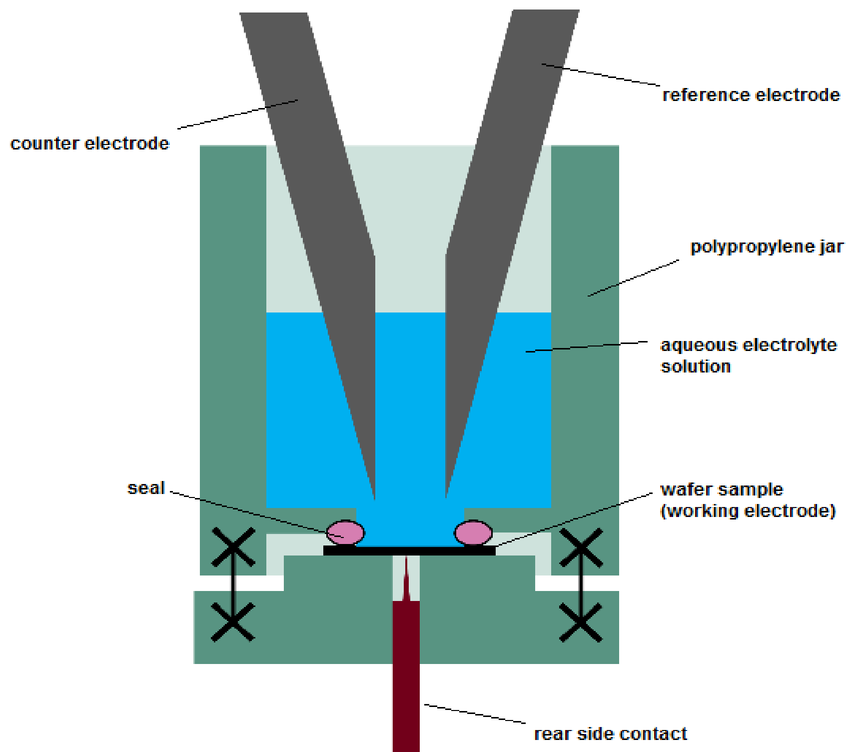

Figure 27: Schematic cross-section of the electrochemical cell

On the bottom of the jar there is a hole of 8 mm diameter, beneath which the wafer specimen is placed and fixed by 3 M4 screws on the jar by a button back plate. The back-side contact of the wafer specimen is provided by a pogo-pin in the lid (cf. Fig. 28).

With this setup a proper contact between the metalized specimen backside and the electrode cable is ensured. The pressure for sealing is applied homogeneously while the specimen remains unstressed and planar.

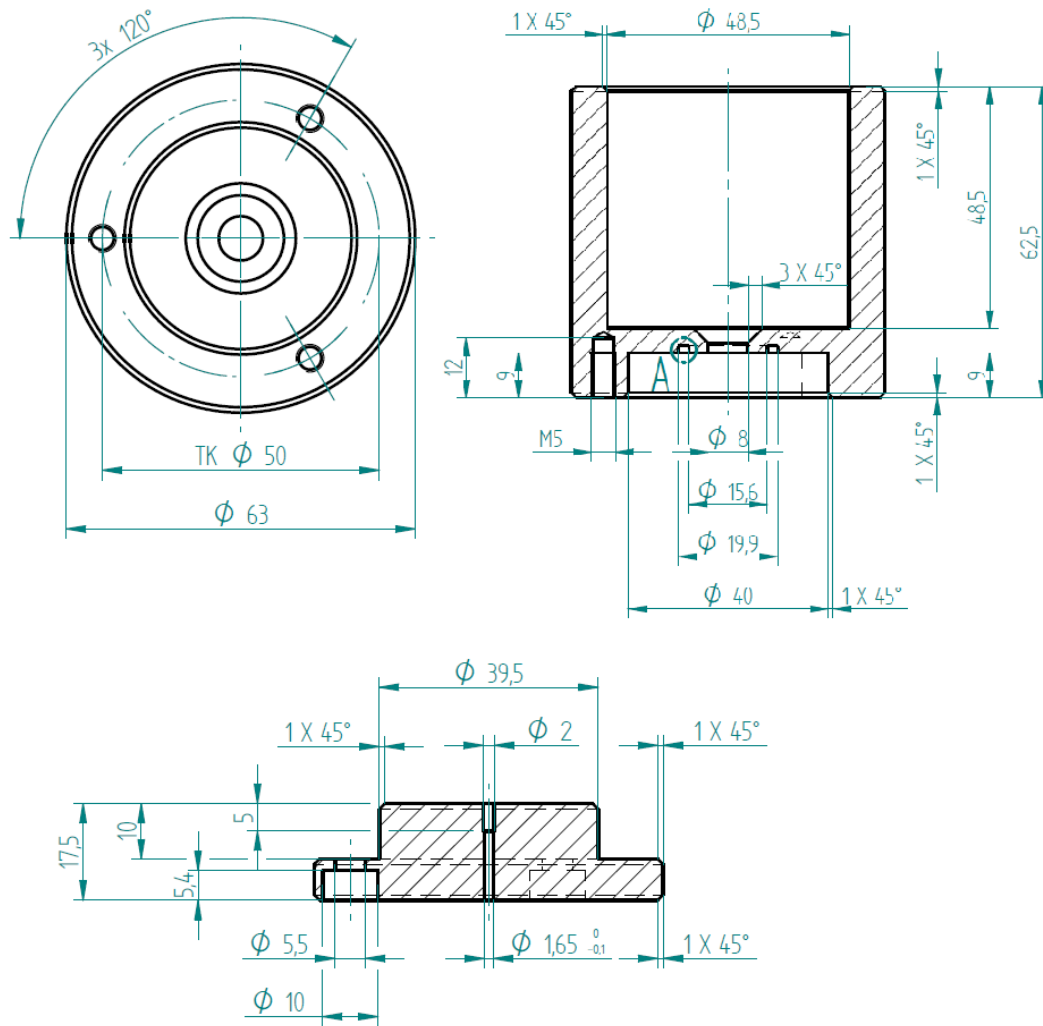

Figure 28: Technical drawings of the electrochemical cell

Figure 29: On the left: the customized cup with the specimen on the bottom. On the right: The cup and the lid with the pogo pin for back-side contact

Electrolyte solutions

The electrochemical corrosion measurements are performed in the following aqueous electrolyte solutions:

- 0,1 M sulphuric acid (H_2SO_4)
- 0,1 M caustic soda (NaOH)
- 0,35% sodium chloride (NaCl) solution
- 0,35% sodium chloride (NaCl); 0,5 mM $K_4[Fe(CN)_6]$; 0,5 mM $K_3[Fe(CN)_6]$
- "urban rain":
  - 0,2 g/L Na_2SO_4
  - 0,2 g/L $NaHCO_3$
  - 0,2 g/L $NaNO_3$
  - acidified with sulphuric acid to pH 5

All solutions were prepared with MilliQ ultrapure water. In corrosion science, the used electrolyte solutions should as good as possible simulate the typical corrosive environments that the product has to face later in the field. Sodium chloride is abundant in the environment and highly corrosive. Small amounts of potassium ferrocyanide and potassium ferricyanide were added to the aqueous NaCl solution for the electrochemical impedance spectroscopy measurements in order to allow the determination of the charge transfer resistance. An acidic and an alkine electrolyte were chosen to investigate the corrosion stability of the thin films depending on the pH value of the surroundings. The acidic rain that is common in pollutant urban regions was being simulated by the so-called "urban rain". It was prepared according to the recipe of Fabjan, Kosec et al. [fabj38].

3.4 High humidity performance test (AC test)

The high humidity performance tests were performed at the Infineon site in Villach in an autoclave with 100 % humidity at a temperature of 121 °C and a pressure of 2 bar for 96 hours.

4. Results and Discussion

4.1 Thin film characterization

4.1.1 Optical characterization

This chapter of the thesis will provide an insight in the structural evolution of the film with varying deposition parameters and therefore sets the basis for the structure-property relationships discussed in chapter 4.2. Here, only the most important structural evolution trends as function of the deposition parameters are shown.

As mentioned before, optical thin film characterization is important for monitoring and controlling the deposition process. In a-SiC parameters such as the refractive index n or the optical band gap strongly depend on composition of the layer and therefore can be tuned over a wide range by varying the deposition conditions. The band gap energy is determined by measuring the optical transitions between valence and conduction band [janz12] and typically has values between 1,8 and 3,0 eV for a-SiC. The refractive index of a-SiC layers can be tuned over the range between 3,7 and 1,8 at infinite wavelength [bull40].

In this subchapter the influence of the a-SiC film composition and the possibility to tune optical parameters by changing the RF power during deposition shall be investigated.

4.1.1.1 The influence of a-SiC film composition on optical parameters

The PECVD process of a-SiC is monitored with an Opti-Probe 5240 by measuring the parameters film thickness, refractive index, Tauc gap and Tauc slope. The sensitivity of these values against changes in the deposition process shall be investigated. Moreover, another optical metrology tool, the N&K Olympian, should be tested for its suitability for process control as well. For this design of experiments, five silicon wafers coated with a-SiC were prepared and analysed with both tools. During deposition of the films the silane flow rate was gradually increased for each sample, while all the other deposition parameters were kept constant (cf. Lot VE669293 in 3.1 Experimental).

The influence of the silane flow rate on the bond types and structural composition of the a-SiC films was studied by means of FT-IR spectroscopy (cf. the following subchapter). The stoichiometry of the layers was analysed at the Ruđer Bošković Institute in Zagreb with TOF-ERDA measurements (Time-of-Flight Elastic Recoil Detection Analysis). The TOF-ERDA results are shown in Fig. 30.

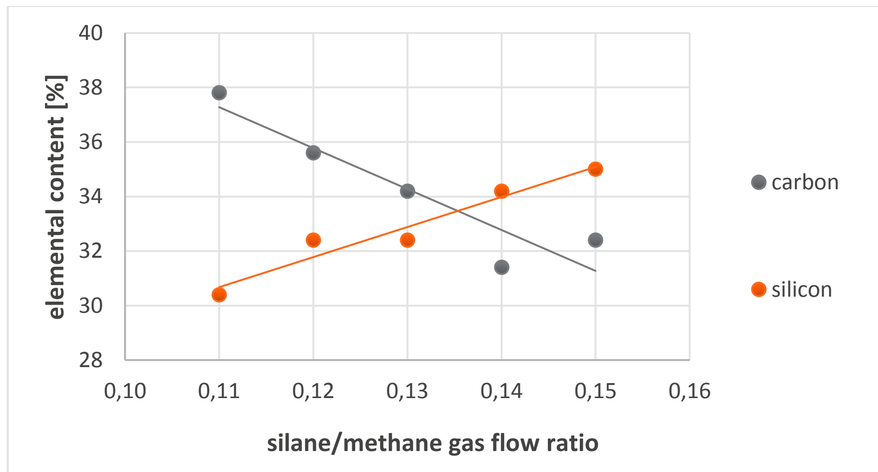

Figure 30: TOF-ERDA results for elemental composition of a-SiC thin films depending on the silane/methane gas flow ratio

As expected, the carbon content in the films decreases while the silicon content increases as a result of raising the silane gas flow rate during deposition. Moreover, a linear correlation between the silane gas flow rate and the silicon content in the final thin films can be demonstrated. By tuning the silane/metane gas ratio from 0,11 to 0,15 the silicon content is increased from 30 to 35 %.

The refractive indices determined with Optiprobe and N&K are shown in Figure 31. The values increase linearly with the silane/methane gas flow ratio and the results for each sample obtained from both tools differ from one another in less than 0,9 %. The Optiprobe only displays values measured at the wavelength of 675 nm. The refractive index however is a parameter that changes with the wavelength of the incident light source. The N&K determines n and k values over the range between 190 and 1000 nm, thus only the refractive index at 673 nm was chosen for the comparison with the Optiprobe.

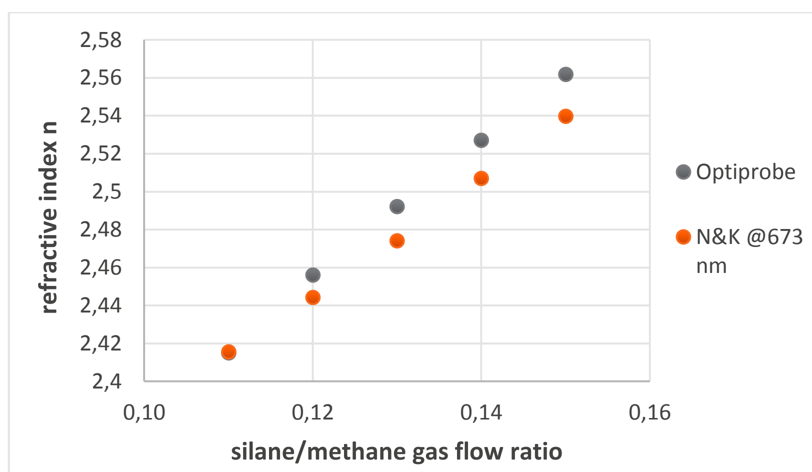

Figure 31: Results from the refractive index determination

The software of the used Optiprobe tool uses a customized algorithm for generating the Tauc plot of the obtained data and the automated determination of the Tauc gap and slope. The N&K tool does not

provide the Tauc plot analysis, therefore another model is needed to determine the optical bandgap of a material. For that purpose, Dr. Franz Heider adapted the method of the band gap energy E04, which originally equals the photon energy where the absorption coefficient takes on the value of 10^4 cm^{-1} [stenz39] in the absorption spectrum (cf. Fig.32).

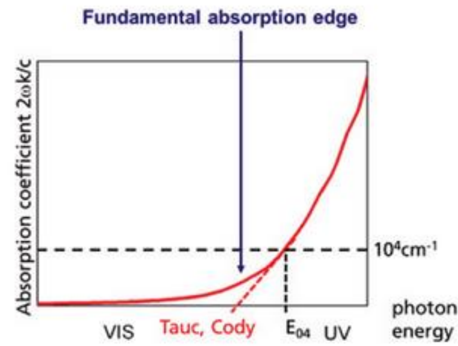

Figure 32: Determination of Tauc gap and band gap E04 [stenz39]

In Figure 33 the values for the Tauc gap obtained with Optiprobe and band gap energies that correspond to the photon energy where the absorption coefficient equals to $8*10^4$ cm^{-1} determined with the N&K tool are displayed. The Tauc gap as well as the band gap decrease with increasing silicon content in the thin films. The band gap energies for each sample from the N&K measurements are approximately 1,07 eV higher than the corresponding Tauc gap energies.

What has to be kept in mind is that both methods exhibit major drawbacks. On the one hand the fitting process of the linear region in the spectrum can easily lead to systematic errors of the resulting Tauc gaps, on the other hand the band gap E04 only depends on a single point in the curve and small deviations or outliers can lead to major changes in the obtained band gap energy values.

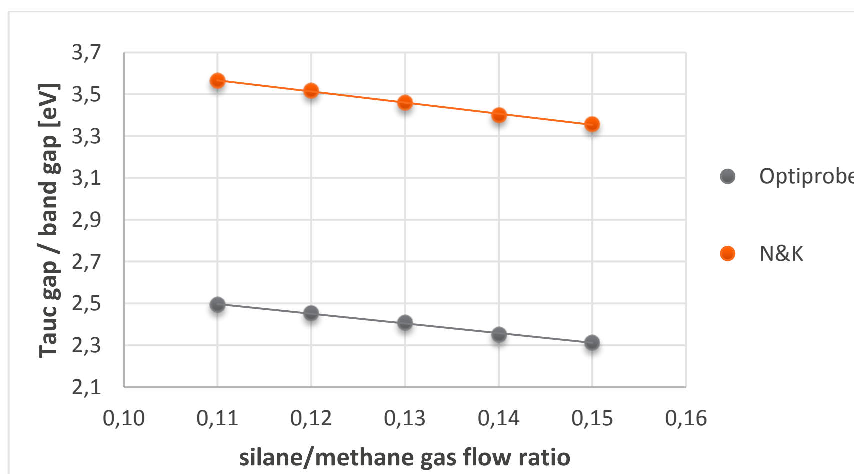

Figure 33: Comparison between Tauc gap (Optiprobe) and band gap (N&K)

The slope of the linear region of the Tauc gap is currently used for monitoring the silicon content of the deposited a-SiC thin films. However, recent analysis suggests that there is no evident linear correlation between these two factors. (cf. Fig. 34). Suggesting that the obtained Tauc slope of 615 is an outlier, a non-linear correlation between Tauc slope and silicon content in the film could be identified.

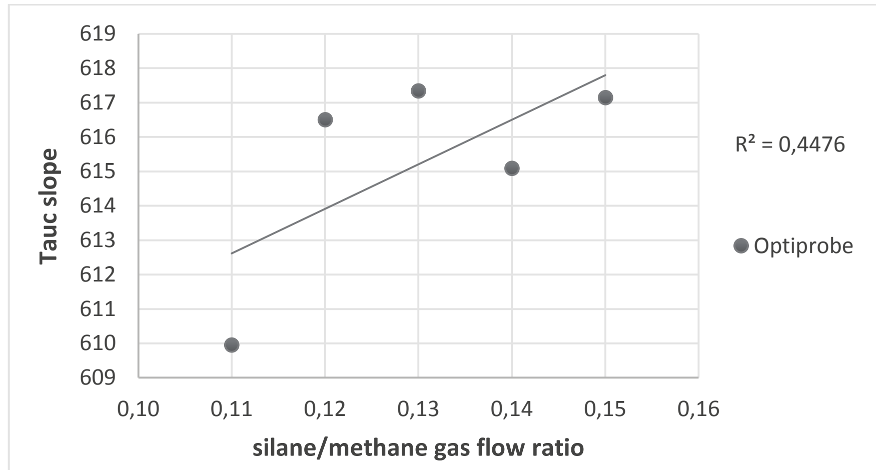

Figure 34: Change of the Tauc slope with the change of silane/methane gas flow ratio

As a conclusion both refractive index and Tauc gap are suitable parameters for monitoring the silicon content in a-SiC thin films deposited with PECVD. The results basically correspond to the findings of Janz [janz12] who investigated the effects of tuning the methane gas flow during microwave PECVD on refractive index and band gap energy of a-SiC thin films. He observed a decrease of the refractive index and an increase in the band gap energy resulting from raising the C/Si ratio [janz12].

4.1.1.2 The influence of the RF power on the optical parameters of a-SiC thin films

As the deposition rates change with the RF power, the deposition time has been adjusted for each sample. Film thickness, refractive index, Tauc gap and slope are measured by the Opti-Probe 5240. The uniformity of the a-SiC film thickness decreases from 5,88 % to 13,7 % as a result of increasing the RF power density (RF power per wafer area) from 1,11 to 2,55 W/cm².

The refractive index and RF power seem to have a strong relationship as shown in Fig. 35. By increasing the RF power density the refractive index can be decreased from 2,54 to 2,44.

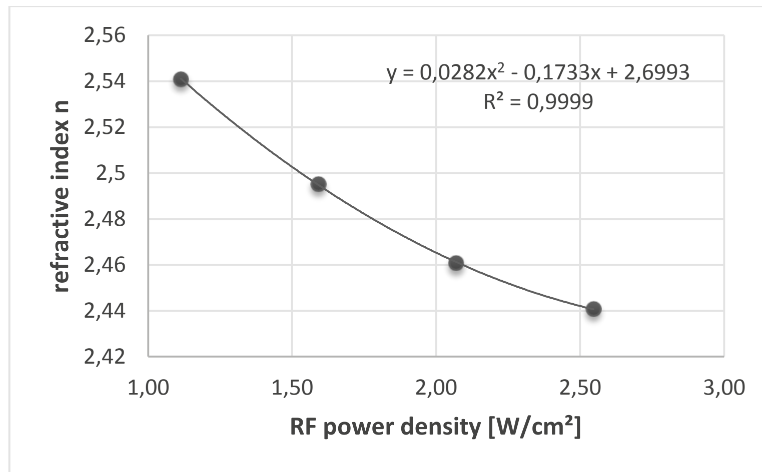

Figure 35: Refractive index as a function of RF power density

Both Tauc gap and slope exhibit a nonlinear relationship with the RF power during PECVD and take the highest values at a RF power density of 1,6 and 2,1 W/cm², as displayed in Figures 36 and 37.

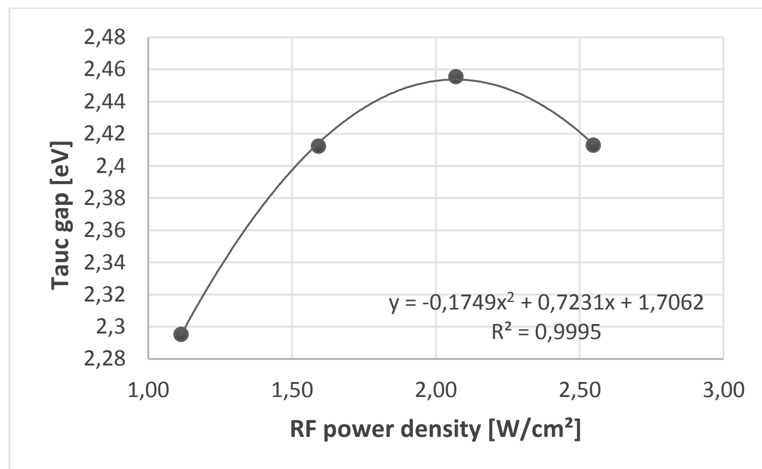

Figure 36: The optical band gap as function of the RF power density

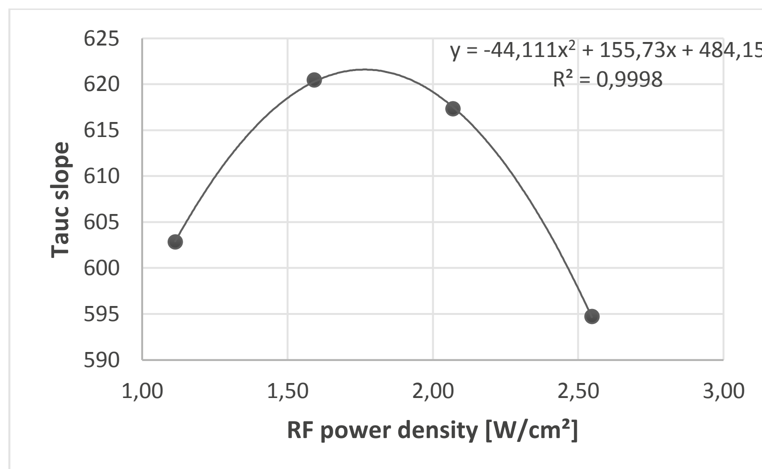

Figure 37: The slope from the Tauc plot as function of RF power density

4.1.2 Stress behaviour

The residual stresses of the a-SiC films deposited at different RF power densities were determined by optical wafer curvature measurements. The results are shown in Fig. 38. The stress of a thin film can be widely controlled by varying the deposition parameters. The PECVD a-SiC films show stress only in the compressive region. By increasing the RF power density in a range from 1,11 and 2,55 W/cm², the stress is gradually shifted from -232 to -910 MPa.

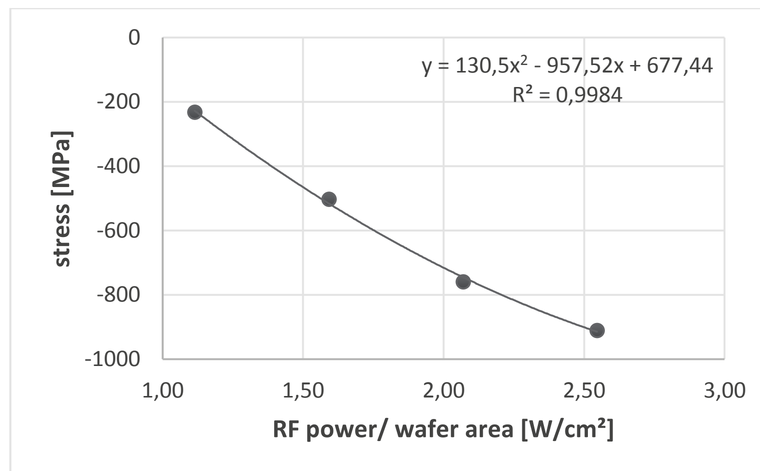

Figure 38: Intrinsic film stress as a function of RF power density

4.1.3 Infrared spectroscopy

The infrared absorption spectrum of lot VE669293 is shown in Fig. 39. The interpretation of the peaks is based on the work of Bullot et al. [bull40] about absorption frequencies in amorphous silicon-carbon alloys. The typical frequencies and vibration modes found in IR spectra of a-SiC are listed in Table 5 [bull40].

The peak with the strongest absorption appears in the range between 700 and 800 cm^{-1} and can be assigned to Si-C stretching mode in amorphous silicon carbide. At 780 cm^{-1} rocking or wagging vibrations of CH_3 groups that are attached to silicon are expected. The mixing of these vibration modes leads to enhanced absorption strength in the spectrum [bull40].

Vibrations of C-H bonds have rather small absorption strength compared to those of Si-H and Si-C bonds, especially when the carbon atom is bonded to silicon. Moreover, some of the Si-H, Si-C and C-H vibrations overlap in the spectrum which makes the interpretation more difficult (cf. Table 5) [bull40].

The small inflection at the biggest peak at around 1010 cm^{-1} might be also deriving from Si-CH_3 rocking or wagging vibrations as well, however a more detailed specification is not possible [bull40]. There are

three peaks with very low intensity in the range between 1250 and 1400 cm^{-1}. Symmetric Si-CH_3 band bending vibrations can be assigned to the one at 1250 cm^{-1}, and antisymmetric Si-CH_3 deformation might appear at 1350 and 1400 cm^{-1}. Stretching of SiH_2 and $(SiH2)_n$ is observed at 2000 – 2090 cm^{-1}. The absorption in the area of 2860 to 3000 cm^{-1} can be attributed to CH, CH_2 and CH_3 stretching vibrations [bull40].

Table 5: List of typical vibrations in FT-IR of a-SiC, after [bull40]

Frequency [cm^{-1}]	Attribution	Vibration mode
630	Si-H_2	wagging
670-680	Si-C	stretching
780	Si-CH_3	rocking or wagging
900 to 980	Si-CH_3	rocking or wagging
1010	Si-CH_3	rocking or wagging
1000	CH_n	rocking or wagging
1020 to 1040	Si-CH_2	rocking or twisting
1000 to 1100	Si-$(CH_2)_n$ or Si-$(CH_2)_n$-Si	
1250	Si-CH_3	symmetric bond bending
1350	Si-CH_3	antisymmetric deformation
1350 to 1370	CH_3	symmetrical bending
1350 to 1370	CH_2	wagging
1400	Si-CH_3	antisymmetric deformation
1410	Si-CH_2	scissoring or bending
1450 to 1470	CH_2	scissoring
1450 to 1470	CH_3, CH_2	bending
1620	C=C	stretching
2090	SiH_2	stretching
2860 to 3000	CH, CH_2, CH_3	stretching

The variation of the silane/methane gas flow ratio does not seem to have a greater impact on the composition of the a-SiC layers, although the results of the TOF-ERDA measurements showed an increase in the silicon content of ~5 % of the layers between a silane/methane gas flow ratio of 0,11-0,15 The increase in silicon content of the layers can be seen in the increasing intensity of the silicon-related peaks.

The obtained infrared spectrum of a-SiC and its interpretation is in good agreement with the FT-IR spectroscopy measurements of Janz [janz12] who analysed stoichiometric a-SiC thin films of 200 nm thickness. His suggestion is that the silane and methane related signals in the spectrum derive from incomplete bond breaking processes in the plasma during deposition. On one hand the energy coupled into the plasma could be too low; on the other, the growth rate could be too high which does not provide sufficient time for molecular collisions [janz12].

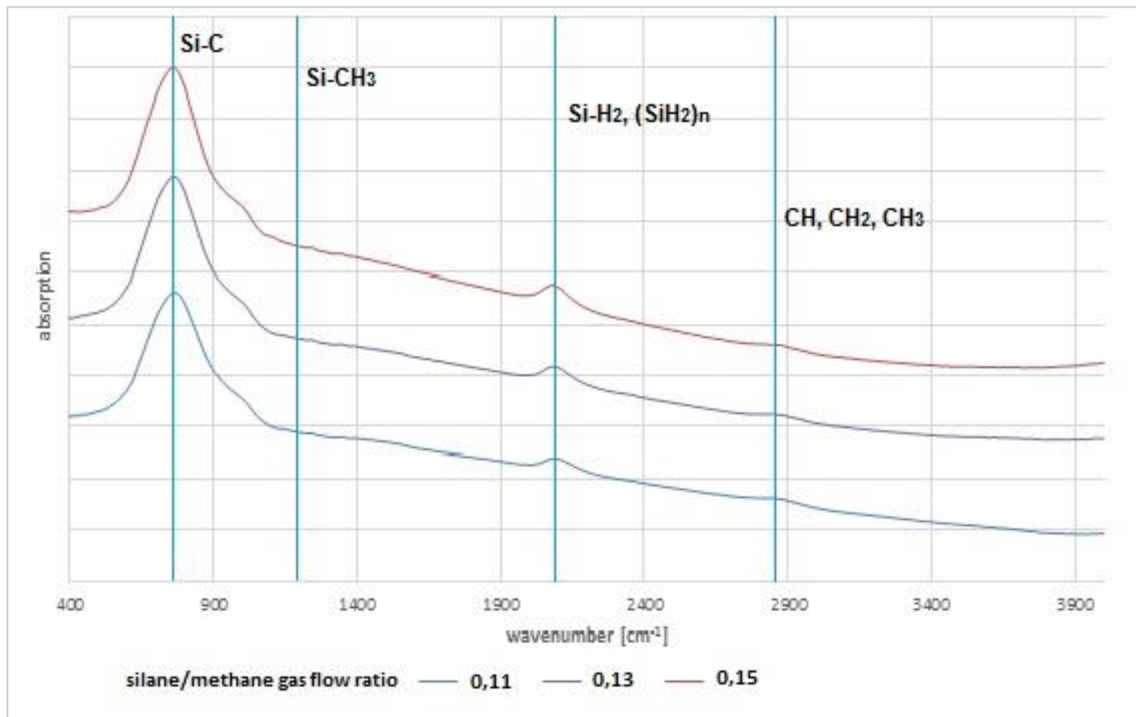

Figure 39: Absorption spectrum for PECVD a-SiC with varying silane/methane gas flow ratio

4.1.4 Film characterization summary

The aim of this chapter was to provide the basic understanding of the influence of the deposition parameters on the structure and composition of a-SiC and further lay the foundation for a comprehensive analysis of its corrosion resistance.

It was shown that by raising the silane/methane gas flow ratio from 0,11 to 0,15 the silicon content of the layers increased from around 30 to 35 %. Both refractive index and optical band gap strongly depend on the composition of the film and can therefore be used as indicators for process control. An increase of silicon content from 30 to 35 % led to an increase of the refractive index from 2,42 to 2,56 and a decrease of the Tauc gap from 2,50 to 2,31. In infrared spectra of the respective samples Si-C, Si-CH_3, Si-H_2 and CH_n bonds were identified, however no evidence of a significant structural change induced by the increasing silicon content was observed.

The RF power density was increased from 1,11 to 2,55 W/cm², resulting in a decrease of the refractive index from 2,54 to 2,44. Moreover, a non-linear relationship between RF power and Tauc gap was observed, as it changed in the range between 2,30 and 2,46. High RF powers also led to high compressive film stress, which was raised from -232 to -910 MPa with increasing RF power density.

In the following chapters the relations between film properties, composition and structure and electrochemical corrosion stability will be discussed.

4.2 Electrochemical corrosion measurements

The electrochemical corrosion behaviour of various a-SiC thin film variations in different corrosive media was examined. The first step was the determination of open-circuit potential (E_{corr}), followed by polarization experiments with Tafel plot analysis. The linear regions of the Tafel plots were extrapolated in order to obtain the corrosion current, which is further used to calculate the respective corrosion rates (cf. chapter 2.3). Subsequently the EIS spectra of the samples were recorded. The fitting software ZView was used for generating equivalent circuit models and for determining the charge transfer resistance of the used material. As mentioned before, the charge transfer resistance is a measure of the corrosion stability of the sample; the greater its value, the more stable is the specimen in the corrosive environment.

The electrochemical corrosion stability was investigated for samples with varying

- **RF power density**
- **a-SiC elemental composition**
- **Film thickness**
- **Type of deposition chamber**

In additional experiments, the influence of nitrides and oxides on the electrochemical corrosion behaviour was investigated. The focus of the research was placed on determining the best set of deposition parameters in respect of electrochemical corrosion resistance and overall film stability.

4.2.1 Corrosion behaviour of a-SiC thin films as a function of RF power

4.2.1.1 Tafel plot analysis

The Tafel plots of the blank and the variants with low RF power (LP) in aqueous NaCl solution are shown in Fig. 40. The a-SiC LP layer (RF power density 1,11 W/cm²) has lower values for E_{corr} and for i_{corr} than the silicon wafer without any coating (blank). Lower values of E_{corr} imply that the corrosion reaction starts at lower potentials and a smaller i_{corr} shows that the investigated material is more stable against corrosion.

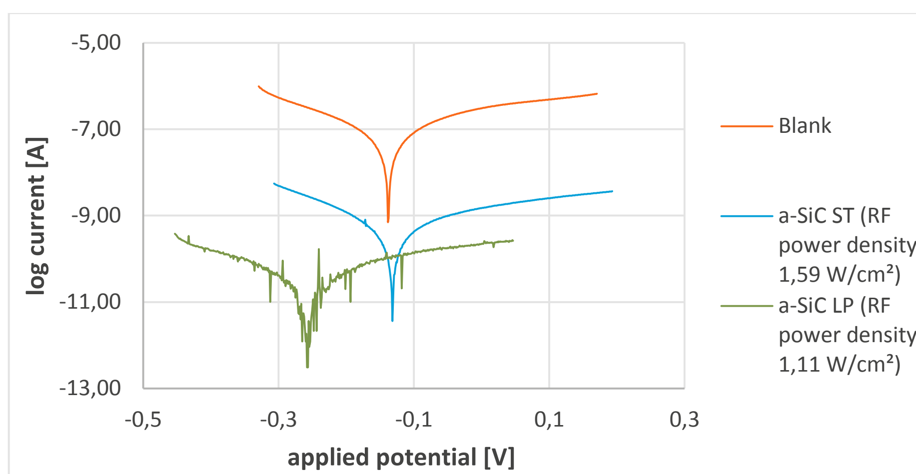

Figure 40: Tafel plots of a-SiC thin films with varying RF power in 0,35% aqueous NaCl solution

In Table 6 the calculated corrosion rates of the samples in different corrosive media are shown, the Figures 41 – 43 show the graphical presentation of the obtained values in block diagrams. Regarding the Tafel plots and the corrosion rates, the a-SiC film deposited at the lowest RF power density is the most stable in all four media. The corrosion resistance seems to decrease with increasing RF power density during deposition. The a-SiC LP variant exhibits corrosion rates four orders of magnitude lower than the a-SiC HP thin film. The a-SiC coatings definitely have a protective function as for every sample with coating lower corrosion rates than for the blank wafer are obtained (cf. Table 6).

Table 6: Corrosion rates of a-SiC films in different media as function of RF power

				Corrosion rate [mm/year]			
Lot	**Wafer number**	**Shortcut**	**RF power density [W/cm²]**	**0,35% NaCl**	**0,1 M NaOH**	**0,1 M H_2SO_4**	**Urban rain**
VE628564	#17	Blank	-	1,41E-02	3,97E-01	5,31E-03	9,62E-03
	#09	a-SiC LP	1,11	6,95E-06	5,48E-06	1,12E-05	6,07E-07
	#10	a-SiC ST	1,59	9,35E-05	5,22E-05	7,85E-05	7,82E-05
	#11	a-SiC MP	2,07	8,42E-04	5,12E-04	4,25E-04	4,29E-04
	#16	a-SiC HP	2,55	2,52E-03	1,94E-03	1,99E-03	1,49E-03

The corrosion rates of the blank wafer in Figure 41 exhibit a significantly reduced corrosion stability in an alkaline environment (0,1 M NaOH, pH 13). The blank silicon sample shows a native thin layer of SiO_2 of less than 5 nm thickness, Silicon oxide is a solid and weakly acidic oxide that is insoluble in aqueous environments except for very strong alkaline pH values.

In alkaline environments an acid-base process is induced and SiO_2 is dissolved to the species $SiO(OH)_3^-$ and $SiO_2(OH)_2^{2-}$ [smith41]. In the other media the blank sample shows significantly lower corrosion rates in approximately the same range of 9,62E-03 – 1,41E-02 mm/year. Its corrosion stability seems

slightly reduced in the aqueous sodium chloride electrolyte compared to the two acidic ones (cf. Fig. 41).

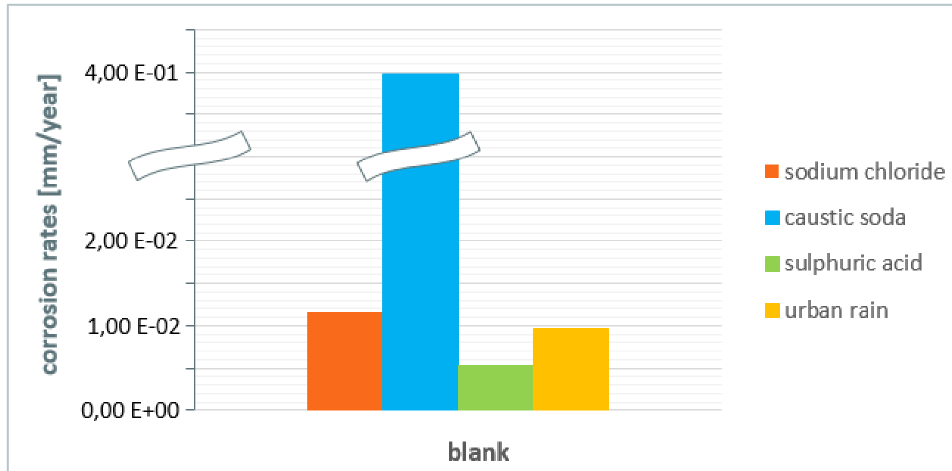

Figure 41: Corrosion rates of the blank wafer sample in different corrosive media

In the Figures 42 and 43 the corrosion rates for the a-SiC thin films deposited with varying RF power density are shown. The a-SiC coatings seem to be nearly equally stable in all four media and not as prone to alkaline pH values as the bare wafer substrate.

However, it is not possible to create a ranking of the corrosive effects of the respective media on a sample when the calculated corrosion rates are within the same order of magnitude. The polarization measurements are performed at very small currents and the i_{corr} values are determined by extrapolation, so small deviations can have a rather high impact on the obtained corrosion rates.

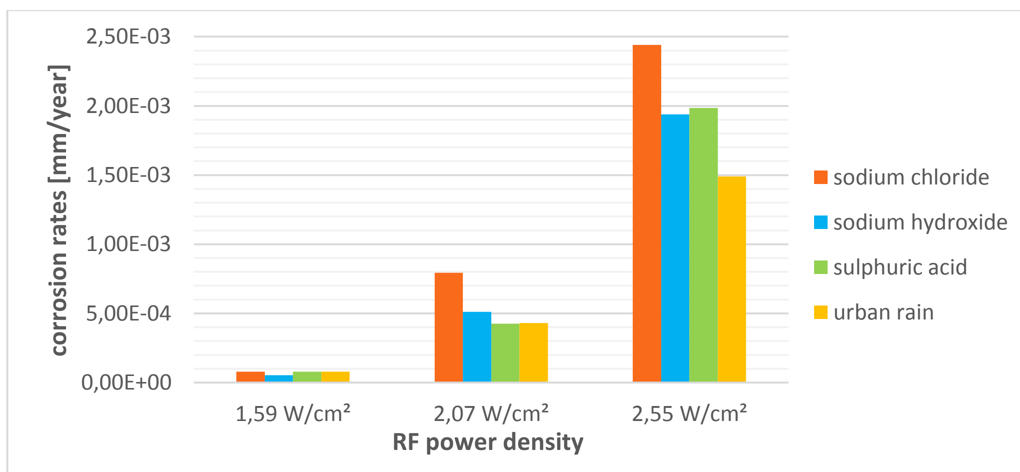

Figure 42: Corrosion stability in different media as a function of RF power density

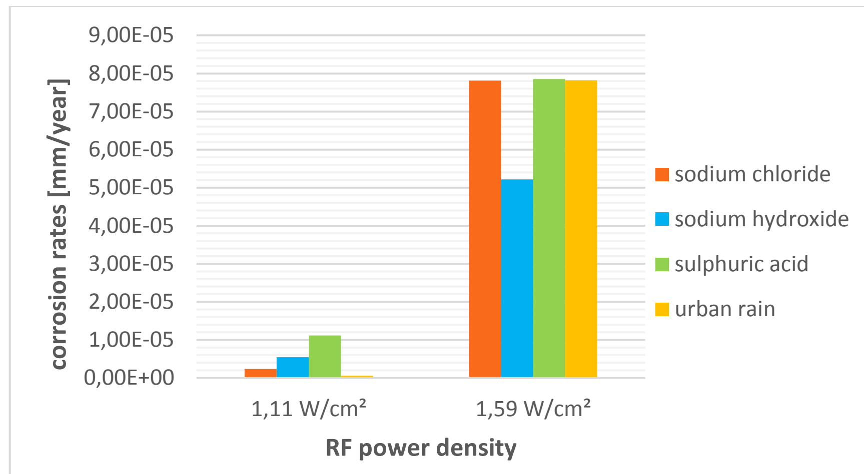

Figure 43: Comparison of the corrosion resistance of the samples deposited at low RF powers

In Table 7 the corrosion properties of the samples of lot VE62864 in aqueous NaCl solution are shown. The values of i_{corr} and E_{corr} as a function of the residual film stress are displayed in Figure 44.

Table 7: Corrosion properties of samples with varying RF power density in 0,35% aqu. NaCl electrolyte

Shortcut	RF power/ wafer area [W/cm²]	i_{corr} [A/cm²]	E_{corr} [V]	Polarization resistance [Ω]	Residual film stress [MPa]
Blank	-	2,98E-07	-1,38E-01	4,58E+05	
a-SiC LP	1,11	6,04E-11	-2,65E-01	1,18E+09	-232
a-SiC ST	1,59	1,99E-09	-1,32E-01	7,07E+07	-502
a-SiC MP	2,07	2,02E-08	-3,81E-02	1,17E+07	-759
a-SiC HP	2,55	6,21E-08	-0,03736	4,81E+06	-910

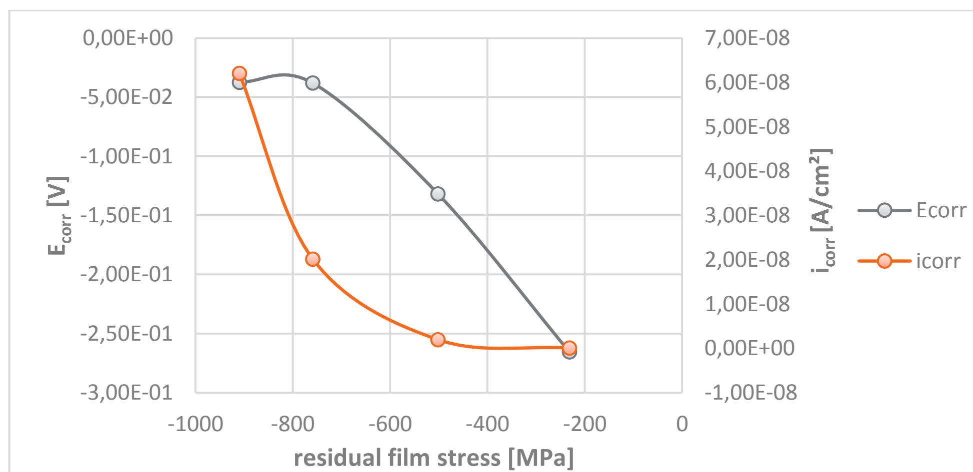

Figure 44: E_{corr} and i_{corr} as a function of residual film stress

In order to quantitatively compare the effectiveness of the coatings, the inhibition efficiency (IE) is calculated according to [ahme42]:

$$IE\ \% = \frac{i^{\circ}_{corr} - i_{corr}}{i^{\circ}_{corr}} * 100$$

with i°_{corr} being the corrosion current of the uncoated sample (blank).

The determined inhibition efficiencies are shown in Table 8. The IE indicates by how much the corrosion resistance of a sample is improved by a coating (decrease of i_{corr}). The variant a-SiC LP exhibits the highest inhibition efficiencies for all tested media, while the a-SiC HP type yielded the lowest. The stability of a-SiC thin films against corrosive attacks seems to be reduced with increasing RF power during PECVD.

Table 8: Calculated inhibition efficiencies in different media

	Inhibition Efficiency [%]			
Sample	NaCl	NaOH	H_2SO_4	Urban rain
a-SiC LP	99,98	100,00	99,79	99,99
a-SiC ST	99,33	99,99	98,52	99,19
a-SiC MP	93,23	99,87	92,00	95,54
a-SiC HP	79,16	99,51	62,59	84,53

4.2.1.2 Electrochemical impedance spectroscopy (EIS)

All EIS measurements were performed in aqueous solution of 0,35 % NaCl, 0,5 mM $K_4[Fe(CN)_6]$ and 0,5 mM $K_3[Fe(CN)_6]$. The addition of the Fe(II)/ Fe(III) redox couple is necessary in order to determine the charge transfer resistance R_{ct} of the sample.

The Nyquist plot of the blank silicon wafer is shown in Fig. 45. Two semicircles can be identified; the larger one is attributed to the corrosion process of the substrate. Modelling and fitting the obtained data with ZView revealed a charge transfer resistance of 9,90E+04 Ω. The smaller semicircle in the high frequency range can be assigned to eventual inhomogeneities or the formation of pores filled with electrolyte in the silicon oxide layer.

In Figure 46 the corresponding equivalent circuit model is shown. It contains three resistance elements; one for the solution resistance of the electrolyte, the resistance related to pores or film inhomogeneity and the charge transfer resistance.

The data obtained for the a-SiC LP thin film (RF power density 1,11 W /cm²) can be modelled with a Randles circuit as shown in Fig. 48. The recording of the impedance values in the low frequency range is limited due to the high charge transfer resistance and capacitance of the material.

Fitting the data yields a charge transfer resistance of 6,05E+08 Ω. A capacitor element does not fit the data very well, thus a constant phase element with a capacitance of 2,2E-08 F/cm² and α of 0,96 is used. This is usual for all types of electrodes which do not behave as an ideal capacitor as the phase shift is smaller than the ideal phase angle shift of 90 °. The reasons for this behaviour are still unknown.

Comparing the Nyquist plots of the blank with the a-SiC LP film, it can be shown that the a-SiC thin film significantly enhances the charge transfer resistance and therefore the corrosion stability of the silicon wafer.

Furthermore, the a-SiC layer seems is homogeneous and impermeable to water.

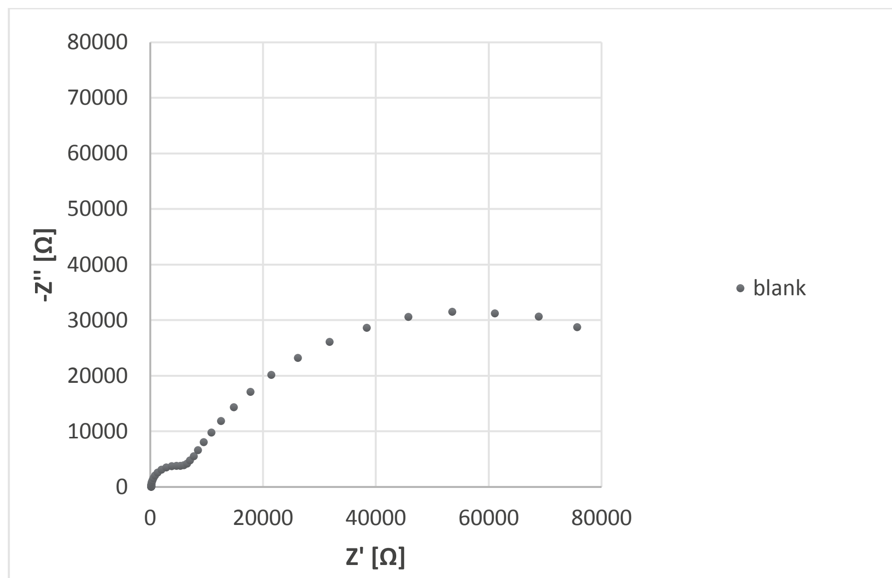

Figure 45: Nyquist plot of the blank silicon wafer in 0,35% aqueous NaCl solution with Fe(II)/Fe(III) redox couple

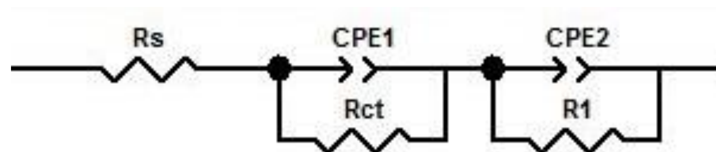

Figure 46: Equivalent circuit model of the blank silicon wafer

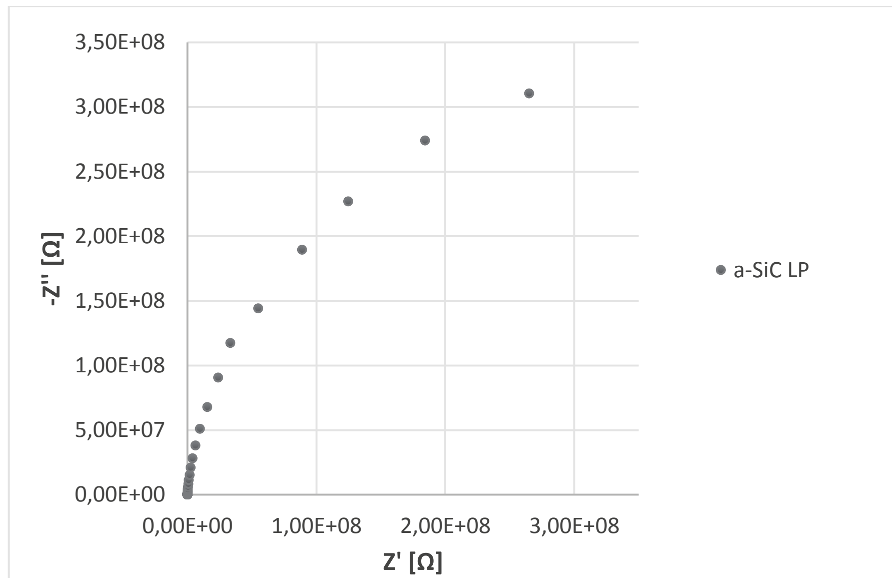

Figure 47: Nyquist plot of a-SiC LP (1,11 W/cm²) in 0,35% aqueous NaCl solution with Fe(II)/Fe(III) redox couple

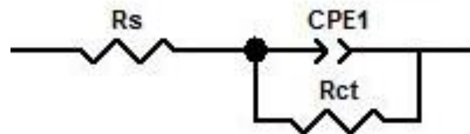

Figure 48: Equivalent circuit model of a-SiC LP and a-SiC ST

The Nyquist plot of a-SiC ST (RF power density of 1,59 W/cm²) is shown in Figure 49. It corresponds almost ideally to a Randles cell and therefore it is modelled by the same equivalent circuit elements as the a-SiC LP film (cf. Fig. 48). A charge transfer resistance of 4,18E+07 Ω and a constant phase element of 2,7E-08 F/cm² with α = 0,95 are determined by fitting the measured data to the equivalent circuit model. The obtained R_{ct} is lower than the one for a-SiC LP, meaning that the a-SiC thin film deposited at higher RF power density could become less corrosion resistant. This result coincides with the outcome of the Tafel plot analysis.

The Nyquist plot of the a-SiC MP sample (cf. Fig. 50) corresponds to the model of mixed diffusion and kinetic control, so it is modelled as Randles cell with a Warburg element (cf. Fig. 51). The Warburg element appears in the low frequency area of the plot as straight line with a slope of 45°, as the species in the electrolyte travel a longer diffusion path at low frequencies. The region of high frequencies is controlled by charge transfer resistance [gamry29]. The calculations yield a constant phase element of 4,66E-08 with α = 0,90 and a charge transfer resistance of 4,36E+06 Ω.

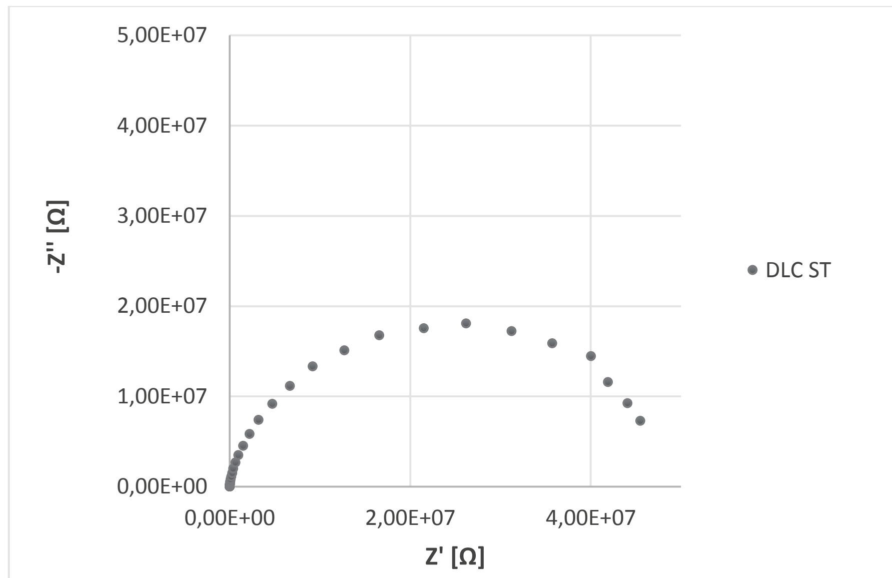

Figure 49: Nyquist plot of a-SiC ST (1,59 W/cm²) in 0,35% aqueous NaCl solution with Fe(II)/Fe(III) redox couple

The Warburg element within the circuit is caused by mass transfer limitations due to diffusion processes of reactants to the surface of the electrode. This diffusion control of a corrosion reaction is often caused by pores in coatings or films on the electrode, for example consisting of corrosion products absorbed solution components [ghali42].

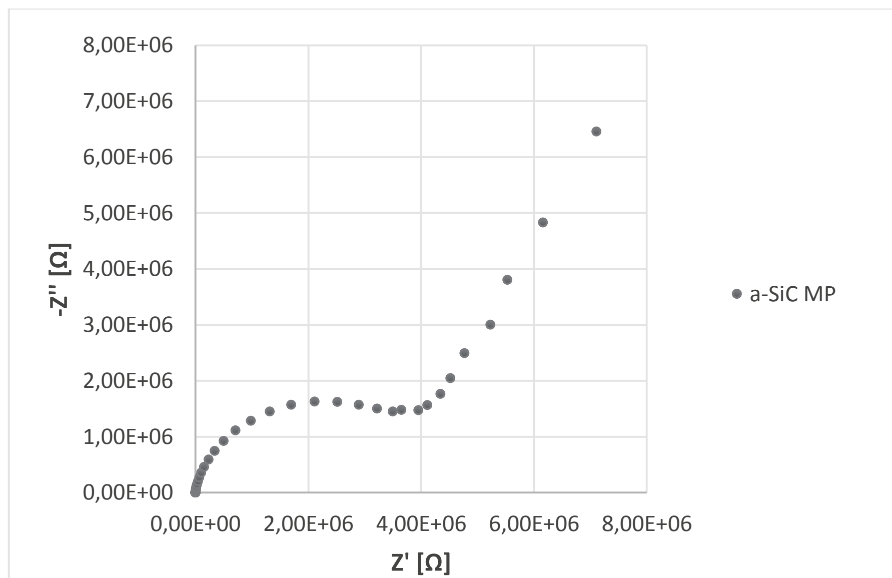

Figure 50: Nyquist plot for a-SiC MP (2,07 W/cm²) in 0,35% aqueous NaCl solution with Fe(II)/Fe(III) redox couple

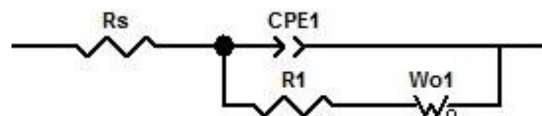

Figure 51: Equivalent circuit model for a-SiC MP

The layer variant a-SiC HP which is deposited at the highest RF power density (2,55 W/cm²) electrochemically behaves like a failed coating. The obtained Nyquist plot shows two semicircles which are related to two different interfaces (cf. Fig. 52). The a-SiC coating is becoming permeable to the electrolyte solution, resulting in a new interface between the liquid phase and the solid substrate. The substrate is basically unprotected and prone to corrosion reactions [gamry29]. The charge transfer resistance is 5,69E+05 Ω, the lowest of all four a-SiC thin film types.

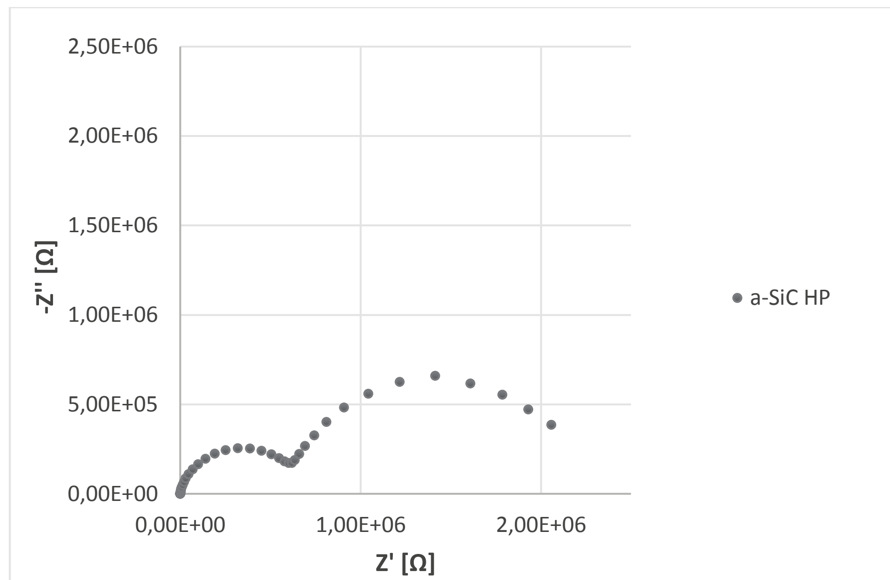

Figure 52: Nyquist plot for a-SiC HP (2,55 W/cm²) in 0,35% aqueous NaCl solution with Fe(II)/Fe(III) redox couple

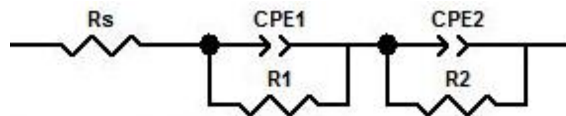

Figure 53: Equivalent circuit model corresponding to a-SiC HP

The calculated values for the corrosion rates and the charge transfer resistances are summarized in Table 9. The charge transfer data from the EIS measurement agrees very well with the results obtained from Tafel plot analysis. Apparently the RF power during deposition has a major impact on the later corrosion stability of the a-SiC layers showing an exponential increase with increasing RF power (cf. Figure 54).

Table 9: Comparison of corrosion rates obtained by Tafel plot analysis and charge transfer resistances from EIS measurements

RF Power [W/cm²]	Label	Corrosion rate [mm/year]	Charge transfer resistance [Ω]
-	Blank	1,41E-02	9,90E+04
1,11	a-SiC LP	6,95E-06	6,05E+08
1,59	a-SiC ST	9,35E-05	4,18E+07
2,07	a-SiC MP	8,42E-04	4,36E+06
2,55	a-SiC HP	2,52E-03	5,69E+05

With increasing RF power density during deposition the corrosion rate increases, while at the same time the charge transfer resistance decreases. As expected, the corrosion rates, which indicate the removal of material due to corrosion reactions in the respective medium, are high for samples with low charge transfer resistance.

The thin films with high charge transfer resistances have a lower tendency to exchange electrons with its surroundings, which is the prerequisite for electrochemical corrosion. Apparently the increase in RF power entails a change in composition and microstructure of the samples tested, which in further consequence affects the corrosion stability of the samples. This assumption is confirmed by the results from film characterization in chapter 4.1, which shows that the intrinsic film stress and the refractive index of the layers are related to the RF power during deposition (cf. Fig. 55). With increasing RF power during deposition the refractive index decreases and the film stress becomes more compressive. A change in film stress is usually the result of re-arrangement within the structure, while the refractive index is sensitive to variations of the composition of the sample. A shift of the intrinsic stress to more compressive values might be an indicator of an increasing density and compactness of the layers.

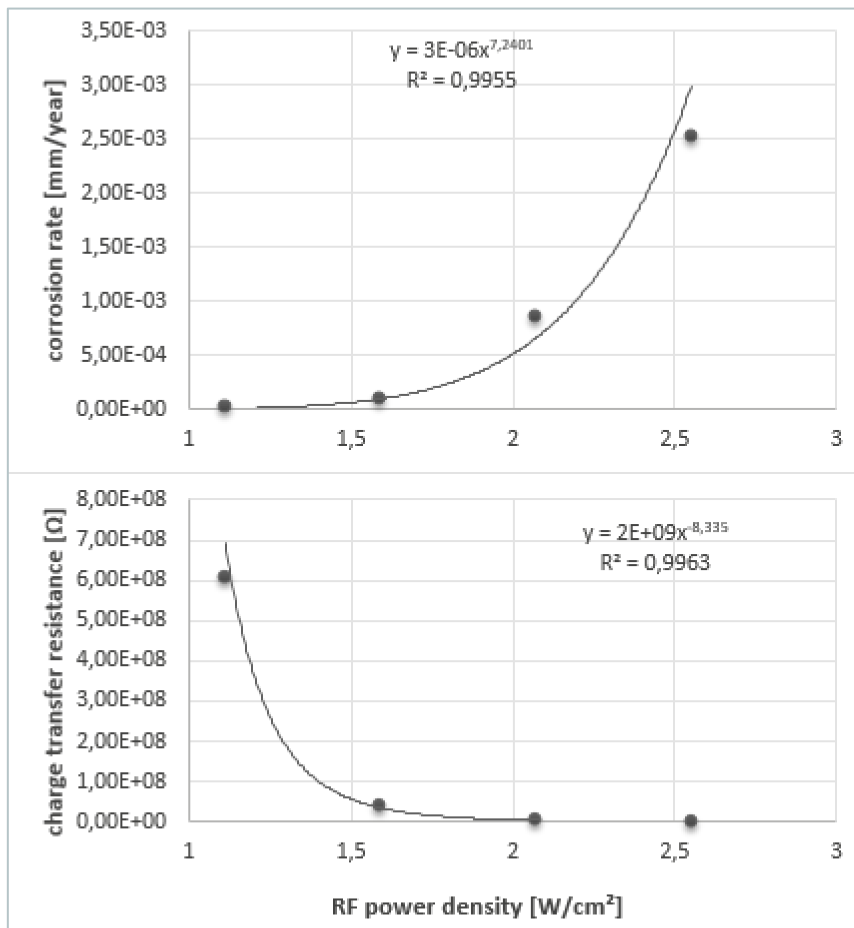

Figure 54: Corrosion rates and charge transfer resistances in dependence on RF power density during PECVD

The refractive index of a-SiC decreases when the carbon content increases [kuhm55], therefore it can be used as indicator of the chemical composition of the samples. Tetrahedral amorphous carbon (ta-C) exhibits a refractive index of 2,52 at 673 nm, pure crystalline silicon on the contrary one of 3,82 [refra47]. Thus, an increase of the refractive index can be interpreted as rise of the silicon content in the sample. In chapter 4.1 it was shown that by tuning the silicon content of the thin films from 30 to 35 % the refractive index can be raised from 2,42 to 2,54 at 673 nm. Therefore, it can be concluded, that increasing the RF Power from 1,11 to 2,55 W/cm² results in less silicon incorporation in the films.

The question arises of which bonding types within the a-SiC structure are especially prone to corrosive attacks and furthermore, why the thin films deposited at higher RF power densities are more susceptible to electrochemical corrosion.

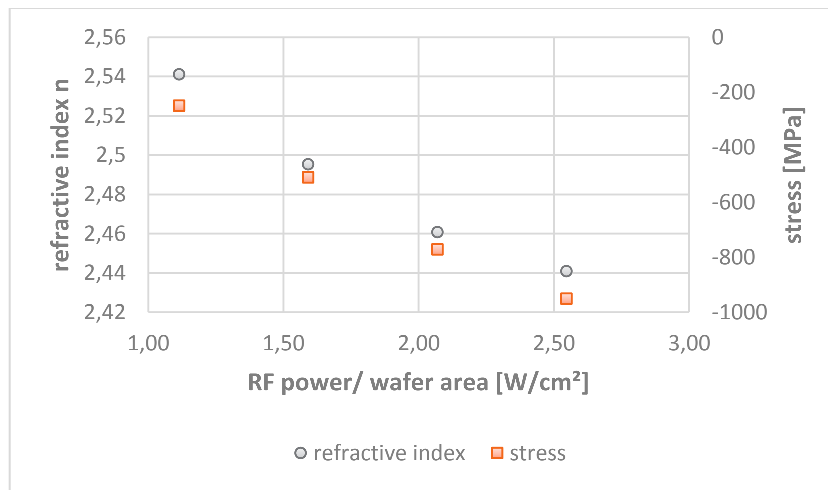

Figure 55: Refractive index and intrinsic film stress as a function of RF power density

In order to investigate and understand the underlying corrosion mechanism it is helpful to examine the possible reactions between the substrate and the corrosive media. Table 10 contains a summary of the standard reduction potentials concerning the corrosion of a silicon wafer covered with an a-SiC layer. The displayed values are standard potentials and vary strongly with ambient conditions and the binding situation of carbon and silicon.

Table 10: Standard electrode potentials of reactions that are relevant for a-SiC corrosion [wiki45]

Process	E° [V]
$SiO_3^{2-} + 3\,H_2O + 4\,e^- \rightleftharpoons Si + 6\,OH^-$	-1,697
$SiO_2 + 4\,H^+ + 4\,e^- \rightleftharpoons Si + 2\,H_2O$	-0,91
$Si + 4\,H^+ + 4\,e^- \rightleftharpoons SiH_4$	-0,14
$CO_2 + 2\,H^+ + 2\,e^- \rightleftharpoons CO + H_2O$	-0,11
$C + 4\,H^+ + 4\,e^- \rightleftharpoons CH_4$	+0,13
$CH_3OH + 2\,H^+ + 2\,e^- \rightleftharpoons CH_4 + H_2O$	+0,50
$CO + 2\,H^+ + 2\,e^- \rightleftharpoons C + H_2O$	+0,52
$2\,H^+ + 2\,e^- \rightleftharpoons H_2$	0,000

As shown in Table 10, the binding state of the respective atom has a major influence on the occurring reaction. Basically one can distinguish between terminally bound atoms and atoms present in the bulk. In a-SiC layers the terminal bonds may be present as Si-H, Si-OH, C-H, C-OH, Si-O-Si, Si-O-C and C-O-C. The ones in the bulk material may comprise Si-C, Si-Si, C-C (sp^3) and C=C (sp^2).

The reactions that may occur within the a-SiC layer might be of purely chemical or electrochemical nature. The possible chemical reactions include hydrolysis and oxidations, where also oxygen and aggressive pollutants such as radicals and ozone might be involved. The Si-H group might be prone to hydrolysis leading to a conversion to Si-OH with additional hydrogen gas evolution, while the Si-C and C-C bonds are relatively inert. This hydrolysis reaction however is restricted to the surface of the film and does not affect the bulk material. Hydrolysis of potentially present Si-O-Si and Si-O-C groups might occur on the surface as well. The occurrence of corrosion due to reactions with reactive oxygen species such as ozone is also not very likely. Singlet oxygen and radicals might attack the bonds, especially the C=C double bond, but a proper insulating layer can inhibit such reactions.

Thus, electrochemical reactions seem the most probable reason for corrosion. Regarding the standard reduction potentials in Table 10, the ones for silicon compounds have lower values and therefore silicon is more likely to be electrochemically oxidized than carbon. The electrochemical attacks of the bonds Si-Si and Si-C start from the surface of the film and might lead to a disruption of the compact layer of silicon carbide. The C-C and C=C bonds might be rather inert to these attacks.

The following two electrochemical oxidation reactions can be assumed for the corrosion mechanism:

(i) 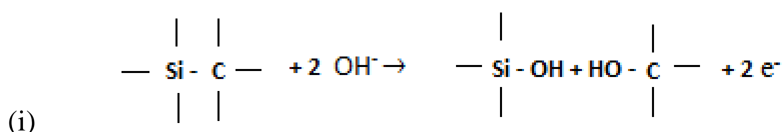

(ii) 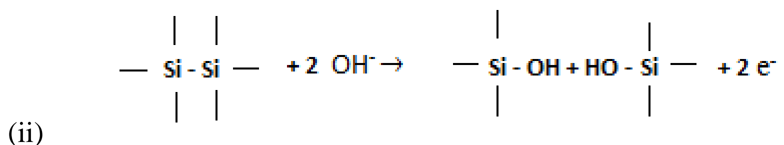

The additional reduction reaction might be the formation of hydrogen from water or the reduction of the –C-OH group:

(iii) 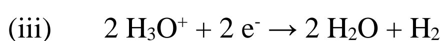 $2\,H_3O^+ + 2\,e^- \rightarrow 2\,H_2O + H_2$

(iv) 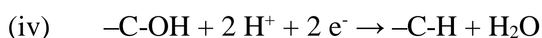 $–C\text{-}OH + 2\,H^+ + 2\,e^- \rightarrow –C\text{-}H + H_2O$

This proposed behaviour is supported by the results observed with FT-IR. As shown in Figure 39, the a-SiC layer exhibits strong signals for Si-C bonds and relatively strong ones for Si-H_2. The Si-H bonds on the surface of the film might be prone to hydrolysis, resulting in the degradation of the surface. The

Si-Si and Si-C bonds in the bulk become more exposed to electrochemical attacks. Due to the advancing corrosion process, the required a-SiC film properties cannot be maintained any more. In edge termination structures the shielding effect of the a-SiC layer would be lost, consequently leading to a breakdown of the device due to the occurrence of high field strengths.

The corrosion process is mainly electrochemical since the sample that exhibits the highest charge transfer resistance is least influenced by the surrounding media.

In this context the question arises of how the RF power changes the deposited material so that its corrosion resistance is affected. The charge transfer resistance is a measure of how much a material ‘resists’ the exchange of electrons with its surroundings, thus it has to be inversely related to the conductivity of the respective material.

Resistivity is one important factor that determines the stability of a material against corrosive attacks. Conductive materials are prone to electrochemical corrosion, while the ones with high resistivities exhibit significantly lower corrosion rates [herm43]. Higher charge transfer resistances are related to higher resistivities of the investigated material. As mentioned in chapter 2.3, the prerequisites for electrochemical corrosion are an electron-conducting material and an environment that is able to take up released ions [ahmad23].

In order to prove that higher RF power densities during PECVD yield a-SiC layers with lower resistivites, Bernhard Leitl, MSc, from KAI GmbH performed conductivity measurements on so-called MIS-C (metal insulator semiconductor capacitance) structures. Besides from a-SiC at different RF powers, various oxides, a-SiC with nitride passivation layer and with varying film thicknesses and a-SiC at different silane gas flow rates have been tested as well. The results are shown in Figure 56. The RF power density has an actual impact on the conductivity on the resulting a-SiC thin film. Within the layer deposited at the highest RF power, the highest current density occurs and therefore it is the most susceptible to electrochemical corrosion. This result was proved by the Tafel plot analysis and EIS measurements.

The respective conductivities were calculated by dividing the measured current density by the electric field strength. The calculated values at electric field strength of 0,5 MV/cm and the charge transfer resistances as a function of RF power density are displayed in Figure 57. As expected, the charge transfer resistance appears to be inversely proportional to the conductivity of the respective thin film.

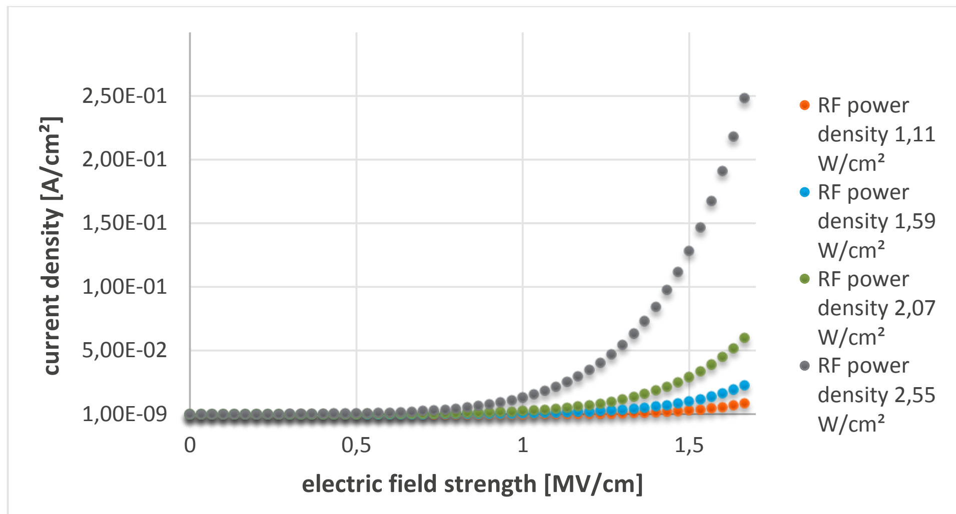

Figure 56: Results from the conductivity measurements on MIS-C structures; conductivity as a function of power density

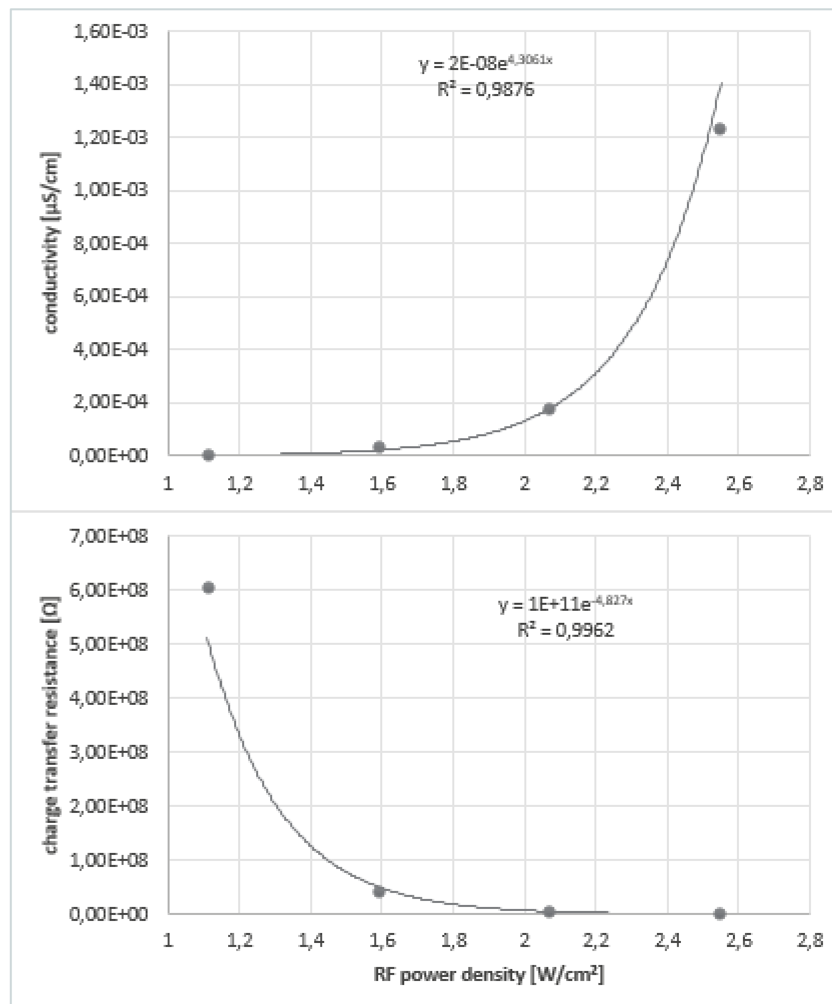

Figure 57: Charge transfer resistance and conductivity as a function of RF power density

In order to investigate the changes in structure provoked by the variation of RF power, Bernhard Leitl, MSc, examined the a-SiC thin films using Raman spectroscopy, a non-destructive structural characterization technique that is suitable for any carbon system [ferra64].

The Raman effect is a light-scattering effect that occurs when a monochromatic beam of light is used to induce the transition of a molecule to an excited energy state [gaug65]. The majority of molecules emit light of the same wavelength as the incident light as they relax back to the ground state of energy (Rayleigh scattering). A small percentage of molecules however relaxes back to a vibrationally excited state and emits light of a different wavelength (Stokes scattering). Anti-Stokes scattering occurs when light is emitted at higher frequencies than the excitation frequency. A prerequisite for molecules to be Raman active is that their polarization changes upon radiation. The Raman effect can be observed in the ultraviolet (UV), visible and near-infrared (NIR) region [gaug65].

Carbon species show their common features in the spectral range between 800 and 2000 cm^{-1} [ferra64]. Upon visible und UV excitation, all carbons show the so-called D band at ~1360 and the G band at ~1560 cm^{-1}. Both can be assigned to vibrations of sp^2 sites; Bond-stretching of pairs of sp^2 atoms in rings and chains occurs as G band and breathing modes of sp^2 carbon rings result in the D band. The T band at 1060 cm^{-1} originates in C sp^3 vibrations and can only be observed upon UV excitation. Except for UV excitation, the excitation resonates with π states and thus, the Raman spectra are dominated by vibrations of sp^2 sites [ferra64].

Raman spectra of carbon systems basically depend on [ferra64]:

- Clustering of the sp^2 phase
- Disorder of bond-length and bond-angle of carbon bonds
- The presence of sp^2 rings or chains
- The ratio between sp^2/sp^3 hybridised carbons

Therefore, Raman spectroscopy provides a comprehensive insight into the carbon bonding situation of carbon-based films [ferra64]. It allows identification of the structural class of carbon, the degree of order and disorder within the structure, and the sp^2 and sp^3 bonding content. In visible Raman spectra hydrogenated carbon samples exhibit an increasing photoluminescence background with increasing hydrogen content, allowing an estimation of the bonded hydrogen content. For hydrogen contents of more than 40 – 45 at.% the photoluminescence background tends to overshadow the Raman signals [ferra64].
The Raman spectrum for the a-SiC layer deposited at the lowest RF power density is shown in Figure 58. The first peak at around 520 cm^{-1} corresponds to the crystalline silicon wafer substrate. Crystalline silicon always appears as sharp and strong Raman peaks due to the symmetrical silicon-silicon bonds

with uniform bond angles and lengths [desch49]. The small peak between 950 and 1000 cm^{-1} can also be assigned to the silicon substrate as second order Raman band [ino50].

In Figure 58, a very small peak at around 1480 cm^{-1} can be identified as C=C (sp^2) bonds. Due to the incorporation of silicon in the carbon network the G band is shifted to smaller wavelengths [guru51] and might overlap with the D band. In the Raman spectrum shown in Figure 58 a high degree of photoluminescence can be seen, which indicates an elevated hydrogen content in the film [ferra64].

Based on the spectrum a hydrogen content of 40 % can be estimated. The elevated amount of hydrogen in the thin film combined with the very weak signal for C-C sp^2 bonds lead to the assumption that the sample has a high content of sp^3 hybridised carbon.

Furthermore, the sample exhibits the lowest conductivity and the smallest compressive intrinsic stress of all tested layer variants. It can be assumed that the a-SiC thin film deposited at RF power density of 1,11 W/cm^2 is a polymeric material, as it exhibits the typical properties that are related to polymers, such as low conductivity, low density and high C sp^3 content.

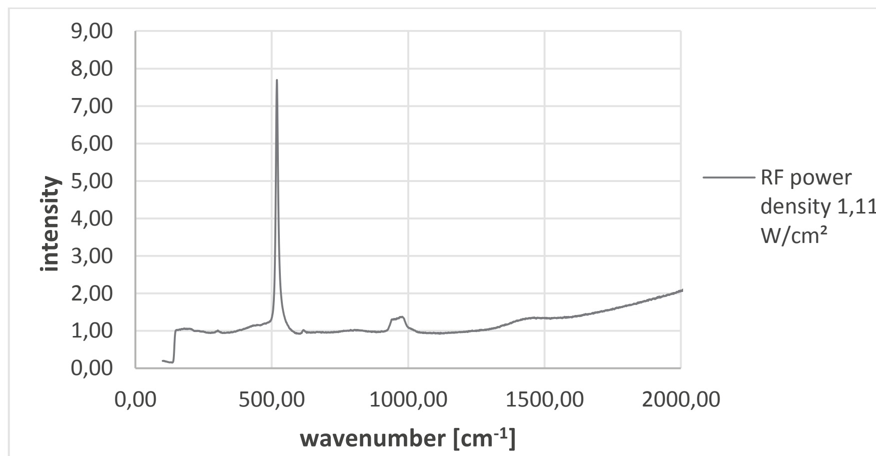

Figure 58: Raman spectrum for a-SiC deposited with RF power density of 1,11 W/cm^2

The Raman spectra for the a-SiC thin films deposited at higher RF power densities are displayed in Figure 59. The spectra exhibit the same peaks for crystalline silicon as the one for 1,11 W/cm^2, which are the main peak at around 520 and the second order Raman band between 950 and 1000 cm^{-1}.

It should be noted that the Raman band for the C-C sp^2 bonds is more strongly pronounced in these layers and that its intensity increases continuously with increasing RF power density for deposition. Apparently the RF power during deposition has an influence on the bonding situation of carbon in the a-SiC thin films.

The C-C sp² content within the films seems to be increasing significantly with RF power density. In order to identify C-C sp³ bonds further tests with Raman spectroscopy in the UV range will be necessary.

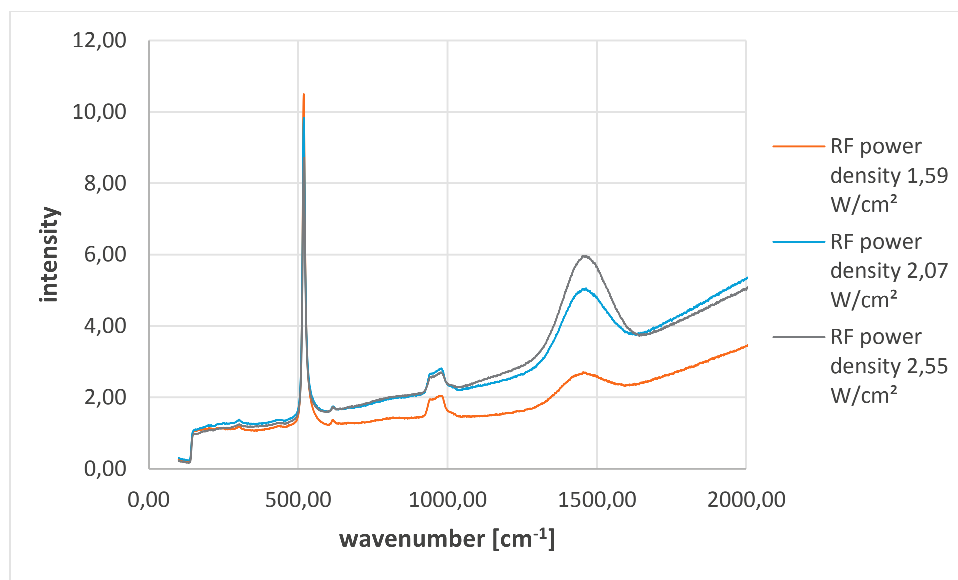

Figure 59: Raman spectra for RF power densities between 1,59 and 2,55 W/cm²

As shown in Figure 55, the refractive index of the a-SiC layers decreases with increasing RF power in PECVD, which indicates the increasing incorporation of carbon in the thin films. A high amount of sp³ hybridised carbon results in non-conductive layers, as could be proved for the polymer-like a-SiC film deposited with an RF power density of 1,11 W/cm².

The other films deposited with higher RF powers exhibited however gradually improved conductivity properties, which can be explained by the changing bonding situation of the carbon atoms from sp³ to sp² hybridisation.

Additionally IR measurements revealed a sharpening and increased intensity of the Si-C related signals in the spectral region of 780 cm^{-1} by increasing RF power (Figure 60). At the same time the Si-H and C-H bonding character is reduced, which leads to the assumption that higher plasma energies diminish the polymeric character of the tested samples.

The increased electron mobility in more conductive films induces a higher sensitivity to electrochemical attacks, which further confirms an electrochemically driven corrosion process. The increased density and higher compressive stress leads in general to more reliable films, the increased conductivity however has a negative effect on the electrochemical stability.

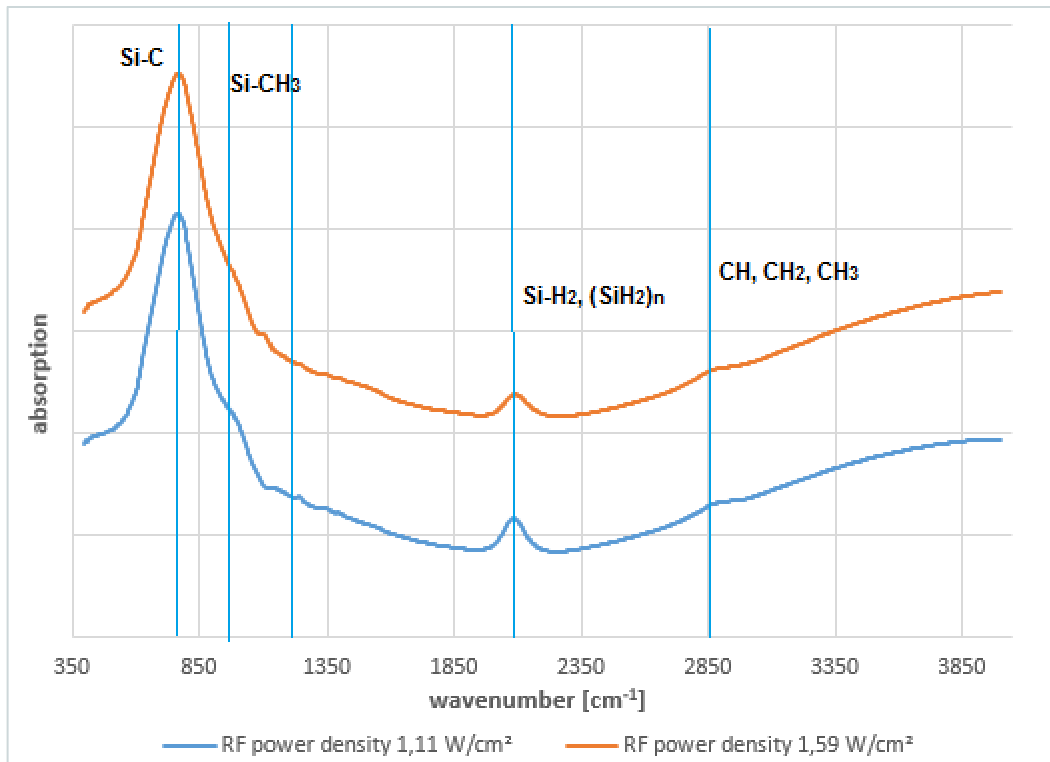

Figure 60: Comparison of IR spectra deposited at different RF power densities

Within this regard, the polymeric SiC film modification with strongest signals for Si-H and C-H in the IR spectrum shows the lowest electrochemical corrosion rate of 6,95 nm/year of the whole SiC series investigated (Figure 54). In accordance, this film shows the highest charge transfer resistance of 6,05E+08 Ω and the lowest conductivity of 2,17E-06 µS/cm determined by MIS-C measurements.

On the other hand this polymeric film is highly water-absorbing even at standard clean room conditions, which prevents its successful use as electroactive passivation in VLD high voltage termination structures. The water incorporation in the films leads to unstable electrical performance and therefore premature failure of the final device.

An a-SiC material with increased density can withstand the absorption of water and thus, is able to maintain stable electrical performance, although its higher conductivity makes it more prone to electrochemical corrosion. Based on these observations it can be concluded that for a given application it is mandatory to review both – the overall material stability and as well as the best possible electrochemical performance.

4.2.2 Corrosion behaviour as a function of film thickness

The samples #06, 08 and 10 from lot VE642365 were coated with thin films of a-SiC with varying thickness and their corrosion behaviour was characterized by means of Tafel plot analysis and EIS measurements. The obtained Tafel plots (cf. Fig. 61) do not differ substantially and the calculated corrosion rates lie within the same order of magnitude (cf. Table 11).

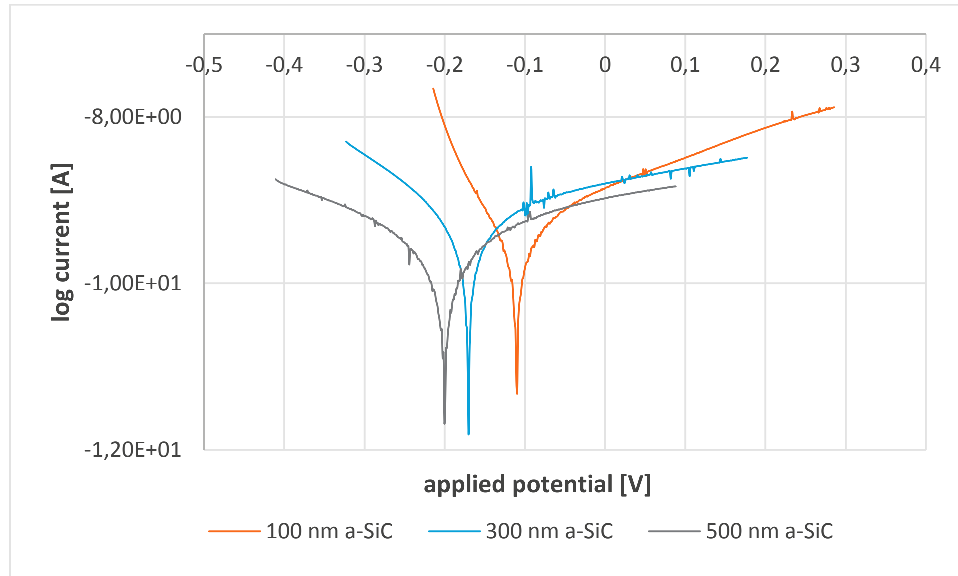

Figure 61: Tafel plots of a-SiC with variation of film thickness

Table 11: Data from Tafel plot analysis and inhibition efficiencies for the variation of film thickness (lotVE642365)

Wafer#	Film thickness [nm]	E_{corr} [V]	i_{corr} [A/cm²]	Polarization resistance [Ω]	Corrosion rate [mm/year]	Inhibition efficiency [%]
6	100	-0,1108	6,52E-10	6,90E+07	2,56E-05	99,78
8	300	-0,1703	2,03E-09	6,95E+07	7,96E-05	99,32
10	500	-0,1999	1,40E-09	1,69E+08	5,52E-05	99,53

Figure 62 shows the comparison of the Nyquist plots of the three investigated specimens. In contrast to Tafel plot analysis, the results of the EIS measurements suggest a dependence of the corrosion resistance on the thickness of the protective coating.

The obtained charge transfer resistances decrease with decreasing film thickness by two orders of magnitude. The equivalent circuit model determined by data fitting corresponds to the one of a simple Randles cell and applies to each sample (Figure 63).

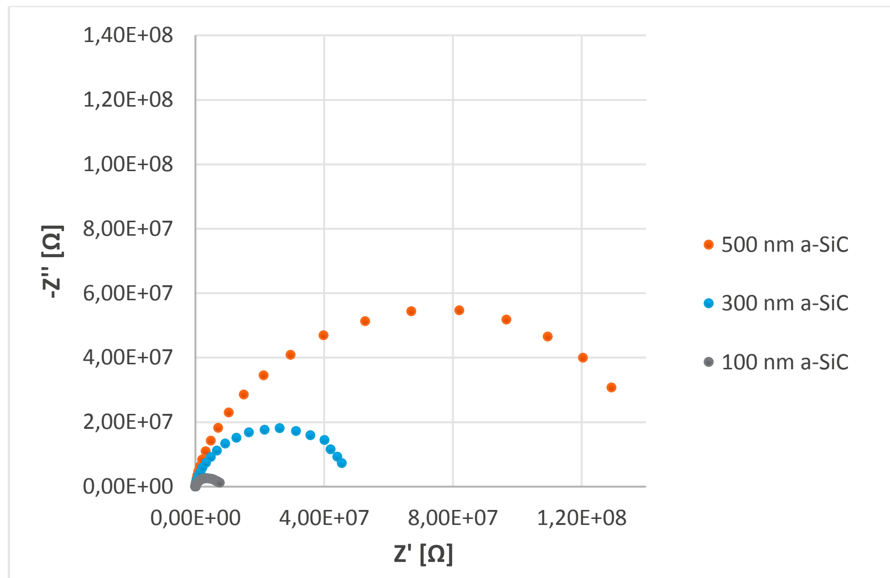

Figure 62: Nyquist plots of a-SiC with variation of film thickness

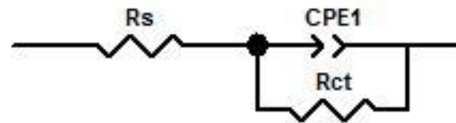

Figure 63: Equivalent circuit model for a-SiC with variation of film thickness

In Table 12 the results of both electrochemical measurement techniques are compared. The corrosion currents determined by Tafel plot extrapolation suggest that the analysed a-SiC layers exhibit more or less the same corrosion stability. The measured currents are so small that the corrosion rates are neither quantitatively nor qualitatively comparable. As it is the same type of a-SiC deposited with the same process parameters (except for the deposition time), it can be expected that the corrosion rates remain the same within the range of measurement related deviations.

Table 12: Comparison of corrosion rates obtained by Tafel plot analysis and charge transfer resistances from EIS mesasurements

Film thickness [nm]	Corrosion rates [mm/year]	Charge transfer resistance [Ω]
100	2,56E-05	5,99E+06
300	7,96E-05	4,18E+07
500	5,52E-05	1,21E+08

The results from the EIS measurements however suggest a dependence of the corrosion resistance on the film thickness (cf. Table 12). The a-SiC thin film with a thickness of 100 nm exhibits the lowest charge transfer resistance, the 500 nm layer has the highest. Contrary to the expectations the conductivity measurements on the MIS-C structures show that the 100 nm layer has the lowest conductivity of all three samples (Figure 64).

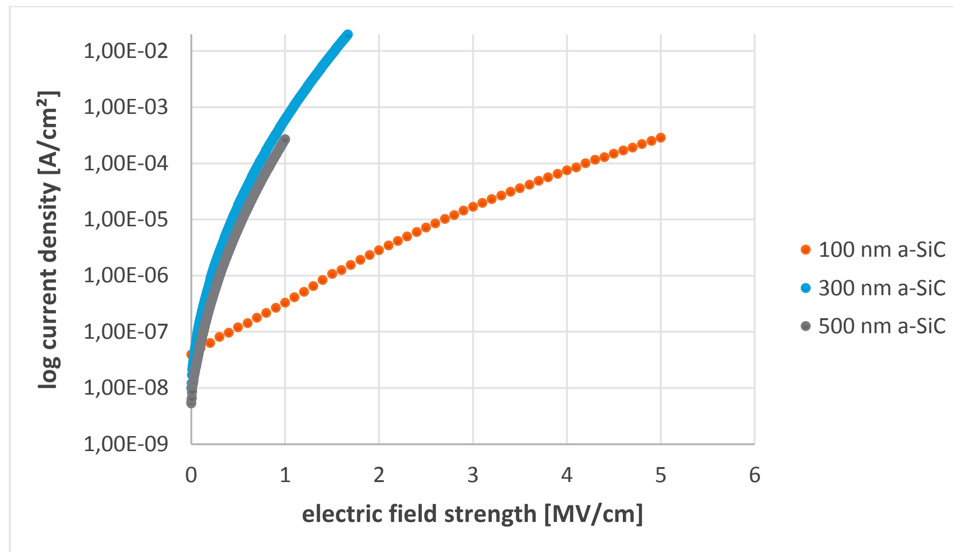

Figure 64: Results from the conductivity measurements on MIS-C structures; conductivity as a function of power density for varying a-SiC film thickness

In Figure 65 the charge transfer resistance and conductivity as a function of film thickness are displayed. The a-SiC film of 500 nm thickness exhibits a higher charge transfer resistance and lower conductivity than the 300 nm thick layer. One of the measurements of the 100 nm film could be an outlier, as the charge transfer resistance clearly contradicts the calculated conductivity. This deviation could be caused by errors during processing, for example skipping the pre-etch or too much residual oxide on the wafer substrates.

On the other hand, the thickness of the coatings is in the sub-micrometre range and thus unknown intra-structural effects might have an impact on the resistivity of the layers. The electrical conductivity of a thin film depends to a certain degree on its dimensions, as it decreases when width or thickness of the sample approach the electron mean free path, which is a measure of how far an electron in the layer can move on average without collisions with other electrons, phonons or impurities. When the sample thickness is about the same or smaller than the mean free path, the electrons do not only lose energy upon collisions with other species, but also upon impact on top and bottom surfaces of the film [chung52]. The 100 nm a-SiC thin film might already be affected by this phenomenon.

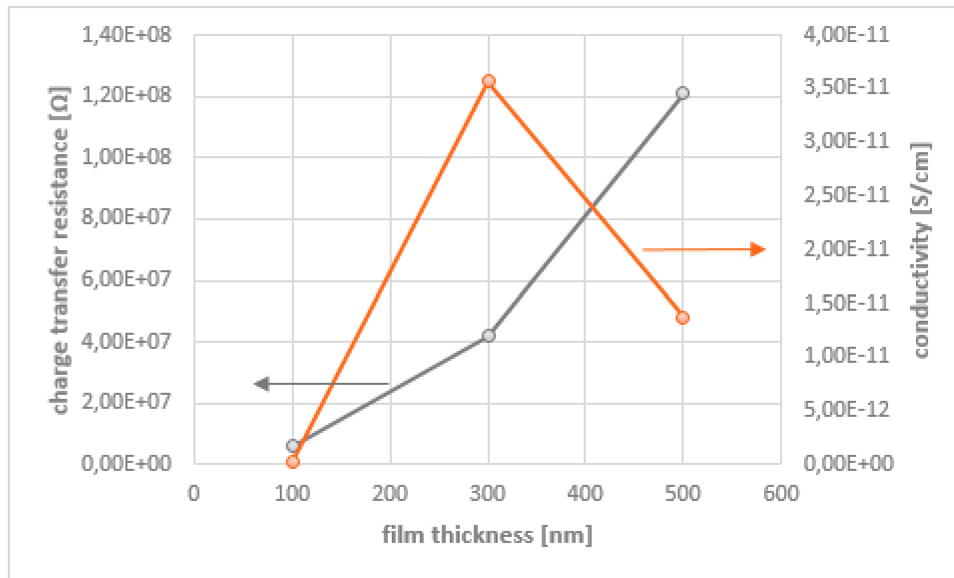

Figure 65: Charge transfer resistance and conductivity as a function of film thickness

As a conclusion, the thickest a-SiC layer exhibits the highest charge transfer resistance. The corrosion rates derived from Tafel plot extrapolation differ only slightly from one another, thus based on these values no quantitative comparison of the samples can be drawn.

The polarization measurements probably are not sensitive enough to detect the comparably small differences in corrosion current between the samples. The conductivity measurements on MIS-C structures result in roughly the same conductivities for the 300 and 500 nm thick a-SiC films, however a conductivity two orders of magnitude lower for the 100 nm thick film. This divergence might be caused by errors during processing or by nano-scale effects.

4.2.3 Corrosion behaviour depending on stoichiometry

The wafers #21-25 from lot VE642365 were deposited with a-SiC thin films with gradually increasing silane/methane gas flow ratio. In Fig. 66 the obtained Tafel plots are shown, the measurement data and calculated corrosion rates are summarized in Table 13.

Inferring from the positions of Tafel plots and the comparably small differences in corrosion current densities, the thin films do not vary too much in their corrosion behaviour. This is confirmed by the obtained corrosion rates, which all lie in the range between 5,27E-05 and 7,89E-05 mm/year. The inhibition efficiency factors that compare the corrosion current density of the coating to the one of the pure substrate lie above 99 % for all silane gas flow rates.

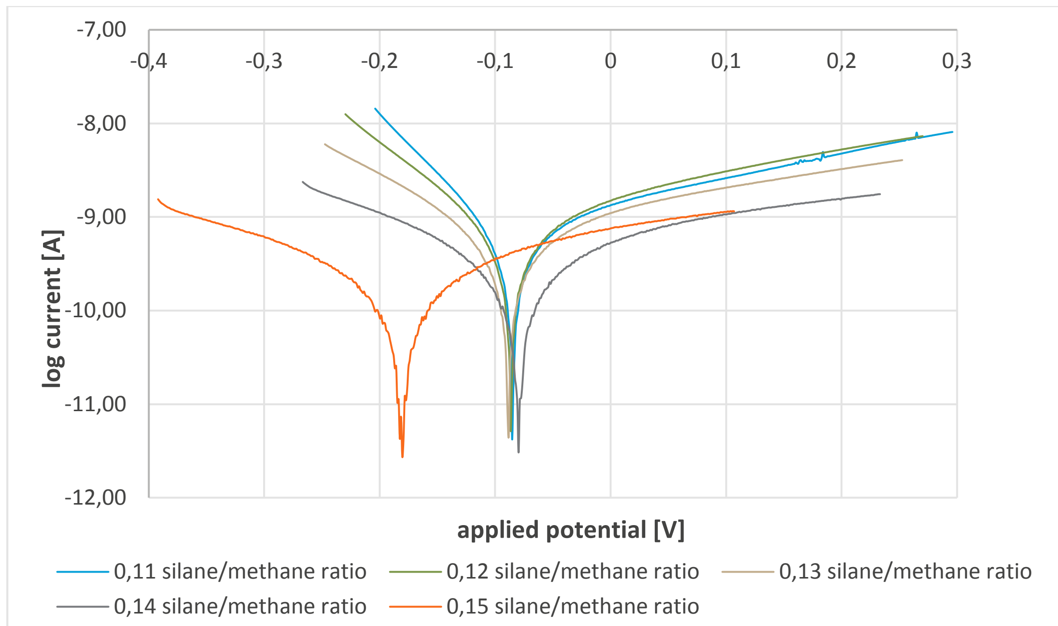

Figure 66: Tafel plots for the variation of the silane/methane gas flow ratio during deposition

The EIS spectra of the samples are displayed in Figure 67. The sample deposited at the highest silane/methane gas flow ratio of 0,15 exhibits a charge transfer resistance of 2,99E+08 Ω. The corresponding equivalent cicuit model is shown in Figure 69.

Table 13: Results from Tafel plot measurements (variation of stoichiometry)

Wafer#	Silane/ methane gas flow ratio	E_{corr} [V]	i_{corr} [A/cm²]	Polarization resistance [Ω]	corrosion rate [mm/year]	inhibition efficiency [%]
21	0,11	-0,08505	1,34E-09	4,35E+07	5,27E-05	99,55
22	0,12	-0,08624	1,65E-09	4,58E+07	6,48E-05	99,45
23	0,13	-0,08858	1,96E-09	6,42E+07	7,72E-05	99,34
24	0,14	-0,07991	2,01E-09	1,35E+08	7,89E-05	99,33
25	0,15	-0,1799	1,40E-09	2,19E+08	5,31E-05	99,53

The charge transfer resistances decrease gradually with decreasing silane gas flow rate. However, the difference in charge transfer resistances is comparably small in the range of one order of magnitude. Samples 21 – 23 were modelled with a Randles circuit that is extended by a Warburg element (Fig. 68), the others with a simple Randles cell (Fig. 69).

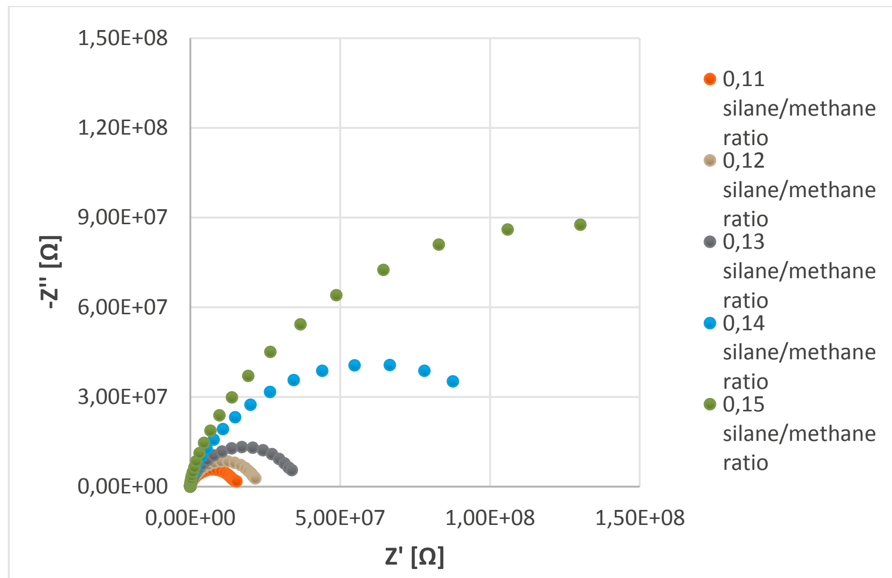

Figure 67: EIS spectra (Nyquist plots) for the variation of the silane/methane gas flow ratio

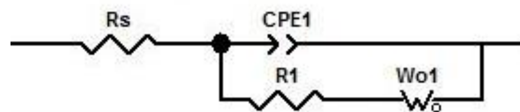

Figure 68: Equivalent circuit model for a-SiC deposited with increasing silane/methane gas flow ratio

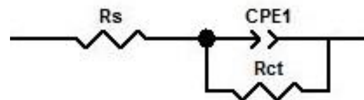

Figure 69: Equivalent circuit model for a-SiC deposited with increasing silane/methane gas flow ratio

The corresponding corrosion rates and charge transfer resistances are summarized in Table 14. The results of the Tafel plot analysis do not quite match the ones of the EIS measurements. The Tafel plots for samples 24 and 25 are coherent, but not for the other ones. Maybe the Tafel plot analysis is not sensitive enough to detect the comparably small differences in corrosion behaviour between the samples.

In contrary, by varying the RF power the charge transfer resistance could be changed in the range of three orders of magnitude (cf. chapter 4.2.1.2), resulting in quantitatively comparable corrosion rates. By varying the stoichiometry, the charge transfer resistances are only altered in the range of one magnitude. The polarization measurements are conducted with very small currents; therefore small deviations in charge transfer resistances of the samples might pose a limitation for Tafel extrapolation. The results for the conductivity measurements with MIS-C structures are shown in Figure 70. As already

suggested by the charge transfer resistances determined by EIS, the elevated silicon content in the films leads to decreasing conductivity.

Table 14: Comparison of the results from Tafel plot analysis and EIS measurements

Wafer #	Silane/ methane gas flow ratio	Corrosion rate [mm/year]	Charge transfer resistance [Ω]
21	0,11	5,27E-05	1,33E+07
22	0,12	6,48E-05	1,92E+07
23	0,13	7,72E-05	3,20E+07
24	0,14	7,89E-05	8,69E+07
25	0,15	5,31E-05	2,99E+08

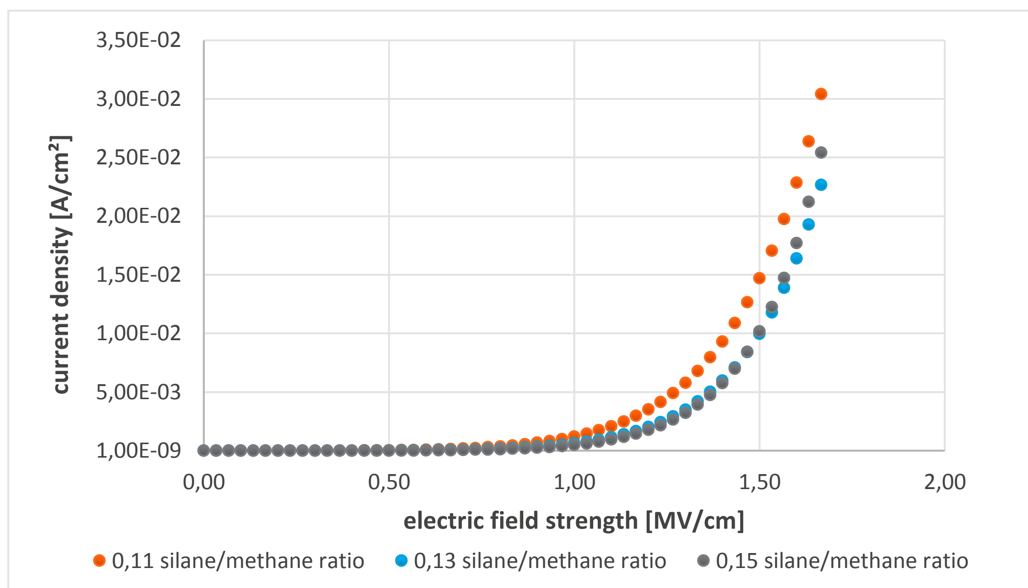

Figure 70: Results of the conductivity measurements for a-SiC PECVD with different silane/methane gas flow ratios

In Figure 71 the obtained charge transfer resistances are compared with the film conductivity at 0,5 MV/cm² electric field strength. The EIS data agrees very well with the results of the conductivity measurements. The conductivity of all three samples lies within the same order of magnitude, which explains the small differences between the calculated corrosion rates.

The a-SiC film deposited with the highest silane/methane gas flow ratio exhibits the highest charge transfer resistance and the lowest conductivity, which indicates that it has the highest electrochemical corrosion stability of all five samples.

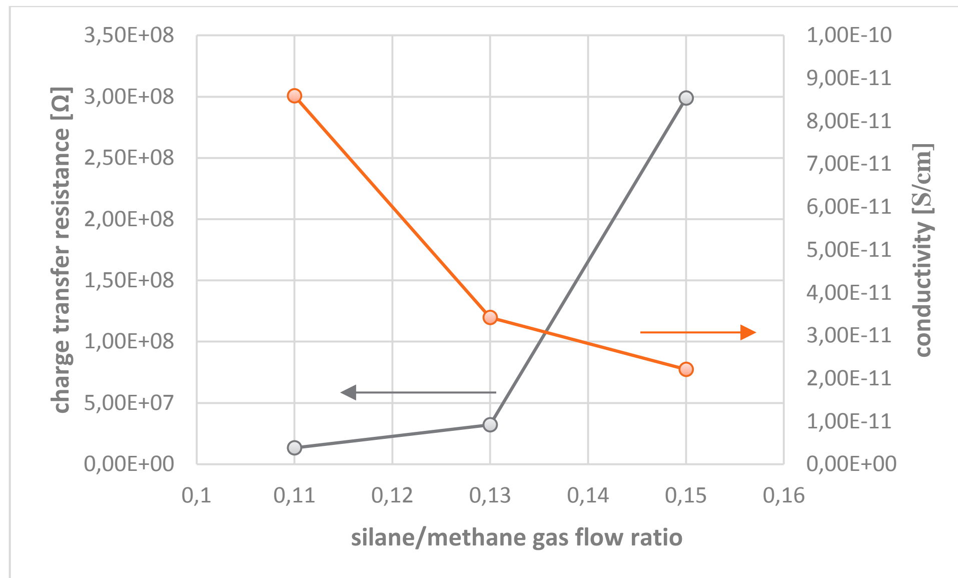

Figure 71: Charge transfer resistance and conductivity as a function of the silane/methane gas flow ratio

In Figure 72 the relationship between elemental film composition and corrosion stability is displayed. It was shown that by increasing silane gas flow rate the incorporation of silicon in the network is being promoted (cf. chapter 4.1.1.1), while at the same time the carbon content decreases. As discussed before, at an RF power density of 2,55 W/cm² the a-SiC layers are already partly graphitized, therefore the increased corporation of tetrahedrally bonded silicon apparently reduces the conductivity of the films.

Thus, not only the applied RF power, but also the precursor gas flow ratio can be varied in order to influence the elemental composition and structure as well as the conductivity of the resulting a-SiC thin films. Moreover, these deposition parameters have a major impact on the electrochemical corrosion stability of the films.

The structural changes upon raising either the carbon or the silicon content also affect the stability of the films against moisture and oxidation. According to Jiang et al. [jiang56] through further incrementing the silane/methane gas flow ratio the moisture barrier ability of the films can be greater enhanced, as with the increased incorporation of silicon microvoids and hydrogen in the amorphous network are reduced. Arce et al. [arce57] varied the gaseous mixture ratio $CH_4/(CH_4 + SiH_4)$ between 0 and 0,87 and measured the IR spectra of the samples immediately after deposition and additionally after six months exposure to air at room temperature. None of the films was altered due to the exposure to air except for the one with the highest carbon content of around 45 at.%, which became oxidized. The researchers draw the conclusion, that the high carbon content entails a high fraction of connected voids and thus, facilitates the incorporation of oxygen in the network [arce57]. So by reducing the carbon content in a-SiC thin films, the moisture barrier ability, the oxidation stability and resistivity against chemical attacks can be enhanced effectively.

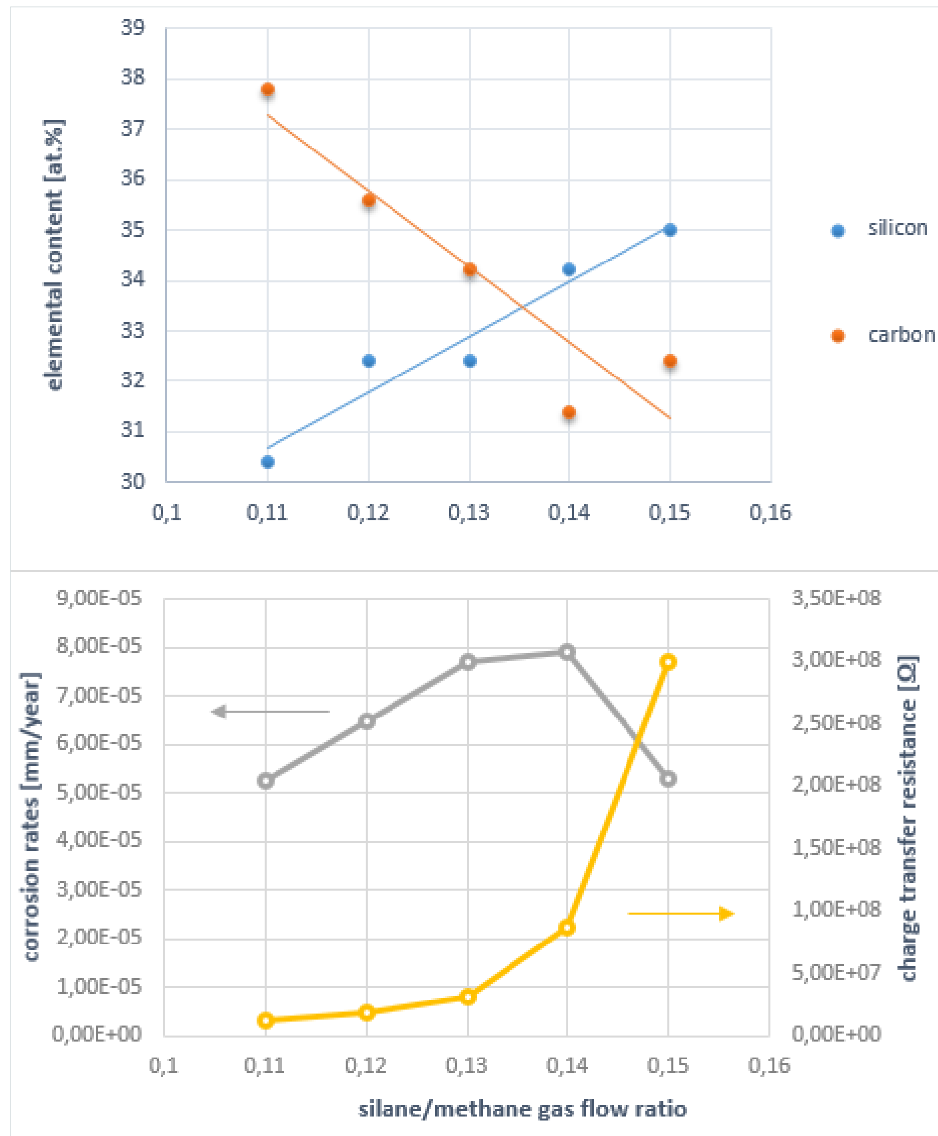

Figure 72: Corrosion rate and charge transfer resistance as a function of elemental composition of a-SiC

4.2.4 Corrosion behaviour of oxides and nitride passivation layers

Samples 18 – 25 from lot VE628564 are coated with either silicon oxides deposited with different techniques, polymer-like SiC (polymeric SiC) or with a-SiC/nitride layer (cf. chapter 3.1 in Experimental). The conductivity measurements on the MIS-C structures show that the oxides and nitrides layers exhibit high resistivities and are hardly conductive compared to the investigated a-SiC films. This can be affirmed by the electrochemical corrosion measurements seen in figure 73 and 75. The Tafel plots of the respective samples cannot be analysed due to strong scattering of the values. The EIS data are modelled by the equivalent circuit of an undamaged, purely capacitive coating (cf. Fig. 74).

The Nyquist plots of a-SiC/nitride and silicon dioxide (POLOX) are shown representatively for all samples in Figures 73 and 75.

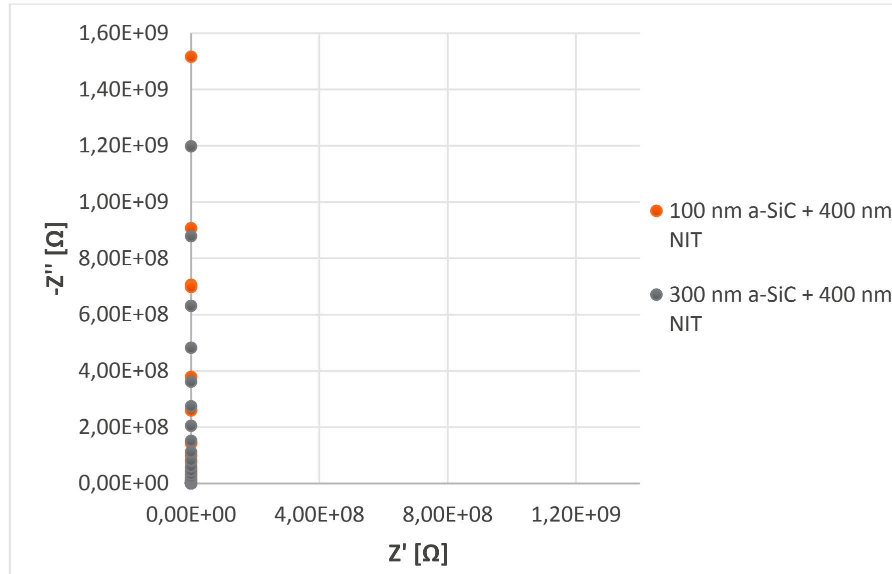

Figure 73: EIS spectra (Nyquist plot) of silicon wafers coated with a-SiC/nitride layer

Various attempts were made in order to achieve corrosion of the samples. Besides from the sodium chloride electrolyte solutions, sulphuric acid and sodium hydroxide solutions were used as well. Moreover, some of the samples were immersed in the electrolyte solution prior to the measurements for about 1 – 65 hours. All these attempts were unsuccessful. As shown in Figure 75, the Nyquist plot of the wafer sample coated with POLOX does not change after 65 hours of immersion in sodium chloride solution.

No quantitative statements can be made on the corrosion stability of the specimens. However, they exhibit better resistance against electrochemical attacks than the a-SiC thin films without annealing. In Figure 73, the effect of a nitride layer on the BKM a-SiC is shown (internal best known method). The nitride film is completely undamaged and there is no evidence of an electrochemical corrosion attack on the film stack, which is why neither corrosion rates nor charge transfer resistances can be determined for the samples. The same film without a nitride passivation layer exhibits a corrosion rate of 9,35E-05 mm/year and a charge transfer resistance of 4,18E+07 Ω. Thus, a nitride thin film as passivation layer for a-SiC is suitable for enhanced corrosion protection.

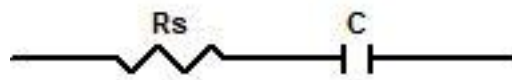

Figure 74: Equivalent circuit of a purely capacitive coating

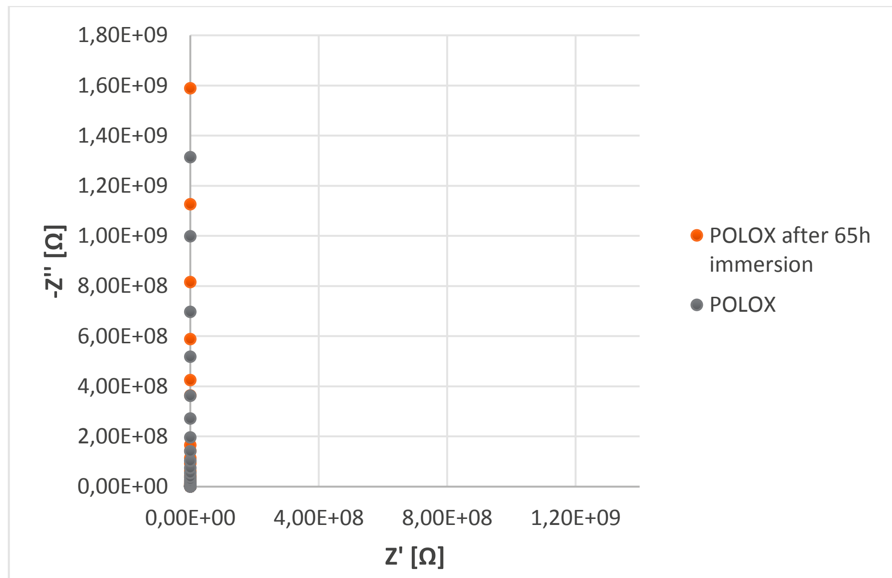

Figure 75: EIS spectra (Nyquist plot) of POLOX, in situ and after 65 hours immersion in 0,35% aqu. NaCl solution

Polymer-like silicon carbide reveals the same electrochemical behaviour as the oxide and nitride layers (Figure 76). Due to the high film resistivity neither corrosion rate nor charge transfer resistance can be determined. The comparison between the conductivity of the polymer-like SiC and the a-SiC films deposited at different RF powers is shown in Figure 77. The polymeric SiC exhibits a conductivity of 6,56E-09 µS/cm at 0,5 MV/cm² electric field strength and is therefore a much less conductive than the layer deposited at the lowest RF power (2,17E-06 µS/cm). Despite its stability against electrochemical attacks, polymeric SiC is no suitable substitute for a-SiC. As mentioned before, polymer-like SiC tends to absorb water, which can lead to preliminary failure of the power device.

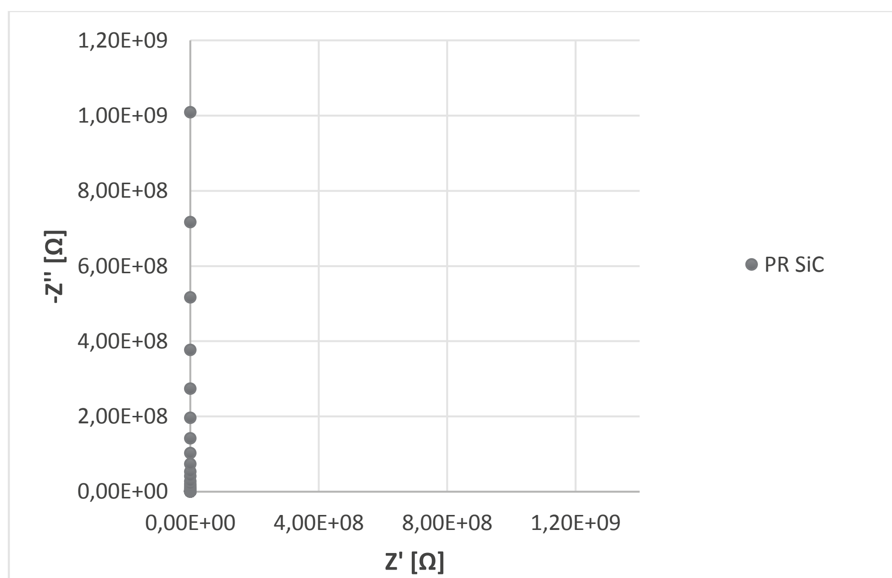

Figure 76: EIS spectra (Nyquist plot) of polymeric SiC

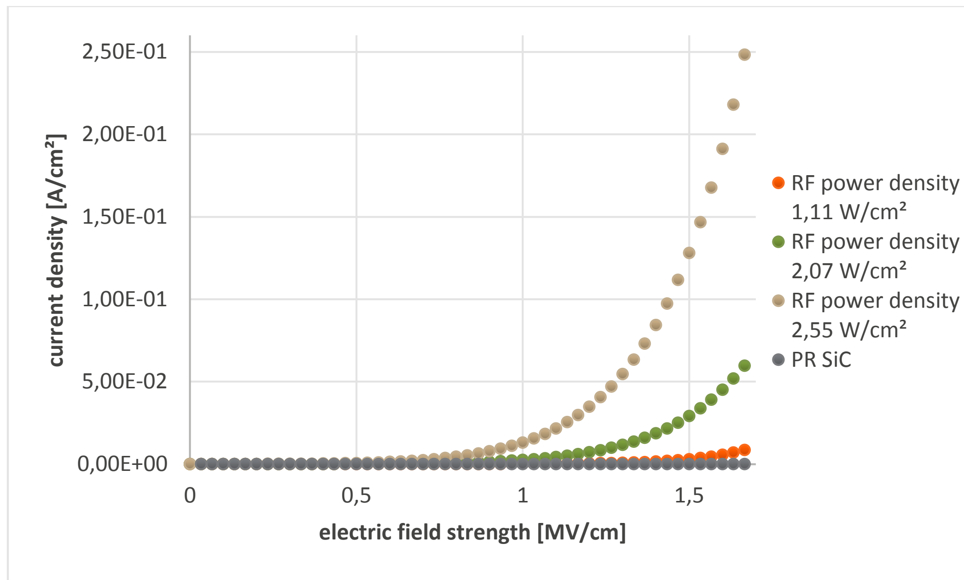

Figure 77: Comparison of the conductivities between PR SiC and a-SiC deposited at different RF power densities

In Figure 78 the IR spectra of PR SiC and a-SiC LP (1,11 W/cm² RF power density) are displayed. The a-SiC film deposited at low RF power density exhibits a sharp Si-C related peak with intensity; the one for PR SiC is less intense and additionally features a more pronounced peak shoulder, which can be assigned to Si-CH_3 bonds. The peaks related to Si-H and C-H bond vibrations have higher intensities in the PR SiC spectrum. It can be shown that by reducing the RF power density, a-SiC starts to develop polymer-like features.

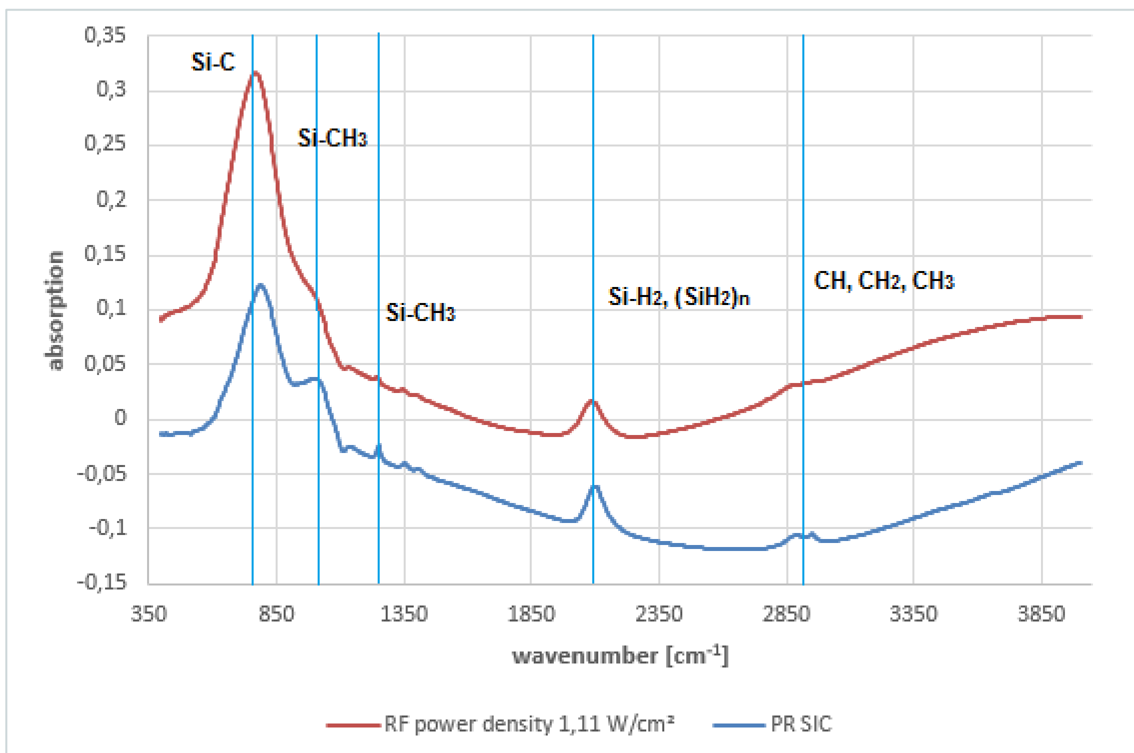

Figure 78: IR spectra of PR SiC and a-SiC deposited at low RF power

4.2.5 Corrosion behavior for a-SiC films deposited by different chamber types

In this subchapter the dependence of the corrosion resistance of a-SiC films on the used deposition chambers is investigated.

For this purpose the BKM recipes for a-SiC deposition are applied for the booth chamber types. Furthermore, the relationship between thin film annealing and corrosion stability is studied. For this purpose, five wafers from lot VC058588 (cf. chapter 3.1) are used: one blank silicon wafer, two coated with a-SiC in a CxZ chamber and two in a MKII chamber, one of each annealed. The obtained Tafel plots from the polarization experiments are shown in Figure 79. The highest corrosion rate is determined for the blank silicon wafer, followed by a-SiC deposited in the MKII chamber without thermal treatment (cf. Table 15). The annealing of the a-SiC MKII coating shifts the corrosion current to more negative values, resulting in a reduced corrosion rate. Thin films of a-SiC deposited in the CxZ chamber are more corrosion resistant than the MKII types. The calculated corrosion rate for a-SiC CxZ without thermal treatment only lies one order of magnitude above the annealed a-SiC MKII. The annealed CxZ variant apparently is too little conductive for the polarization measurements; due to intense scattering no evaluable Tafel plot can be obtained (cf. Fig. 80). The inhibition efficiency factors are the highest for the a-SiC films deposited in the CxZ chamber without annealing and in the MKII chamber with following treatment. The a-SiC CxZ coating achieves an inhibition efficiency of 99,36 %, while the comparable MKII type only has one of 61,72 % compared to the bare silicon wafer.

Table 15: Results from Tafel plot analysis (ht.: heat treatment)

Wafer #	Label	E_{corr} [V]	i_{corr} [A/cm²]	Polarization resistance [Ω]	Corrosion rate [mm/year]	Inhibition efficiency [%]
25	blank	-0,1888	2,91E-07	3,08E+05	1,14E-02	0,00
23	MKII	0,01739	1,11E-07	1,35E+06	4,38E-03	61,72
21	MKII ht.	0,01934	5,95E-11	2,04E+09	2,34E-06	99,98
16	CxZ	-0,1696	1,87E-09	1,66E+08	7,36E-05	99,36

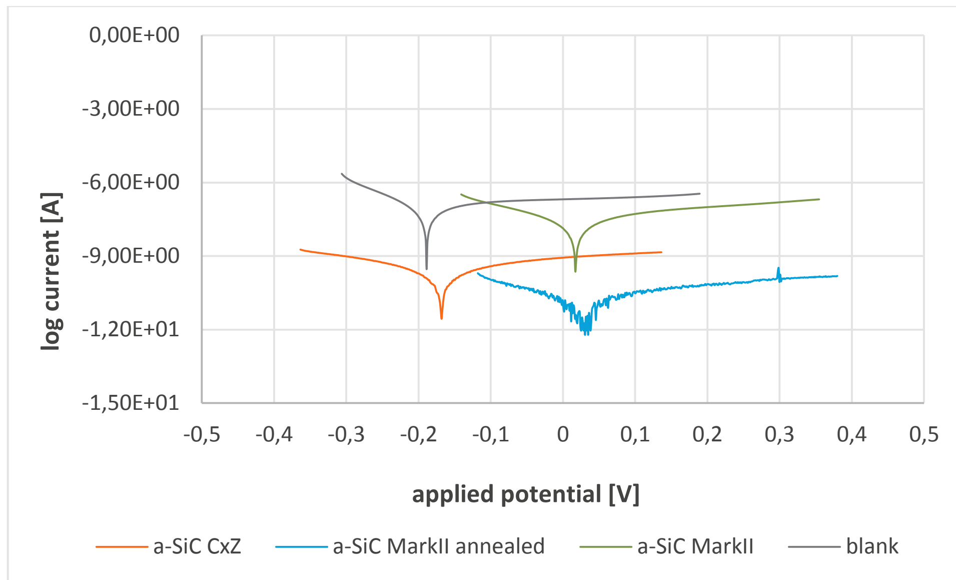

Figure 79: Tafel plot analysis for lot VC058588

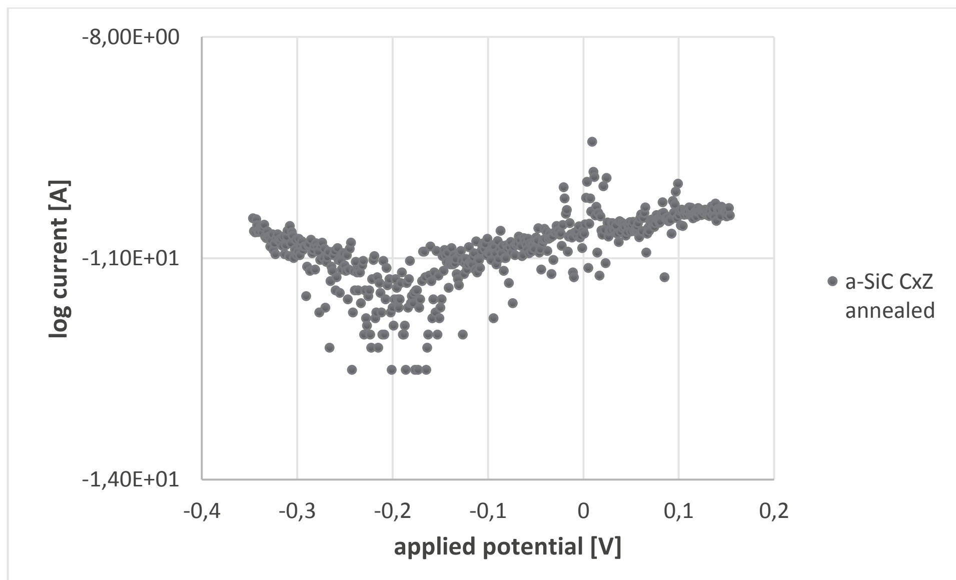

Figure 80: Polarization measurement of a-SiC CxZ after annealing

Figure 81 displays the Nyquist plot for the blank silicon wafer. Two semicircles can be identified, the first one is assigned a resistance of 7300 Ω and might be caused by pore formation in the residual silicon oxide layer of the wafer. The charge transfer resistance is given as 1,13E+05 Ω.

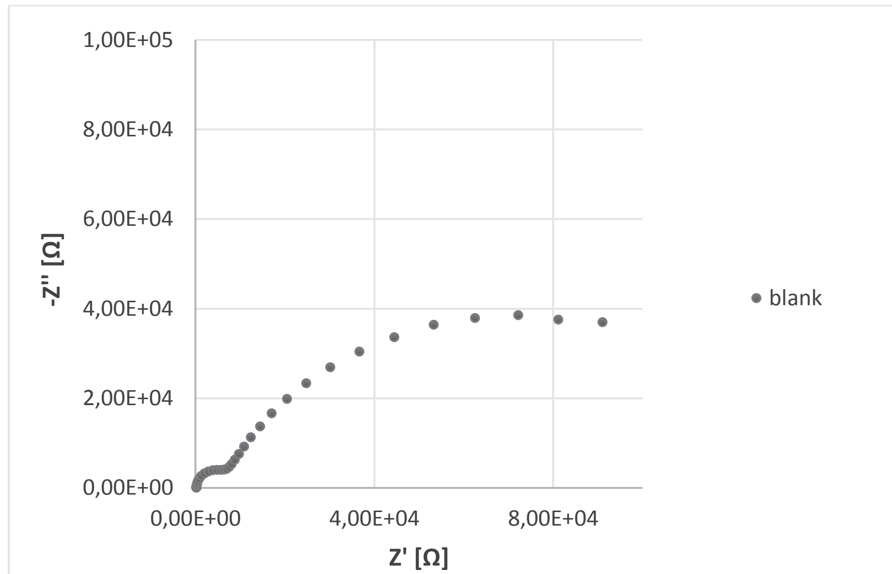

Figure 81: Nyquist plot of the blank sample

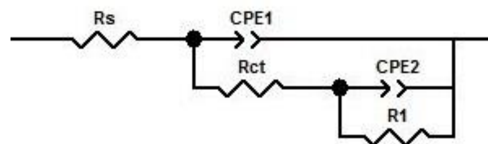

Figure 82: Equivalent circuit model for the blank silicon wafer

In the Nyquist plot of a-SiC deposited in a MKII chamber (no heat treatment) two semicircles are identified as well (cf. Fig.83). The first one is comparably small and can be described by a resistance of

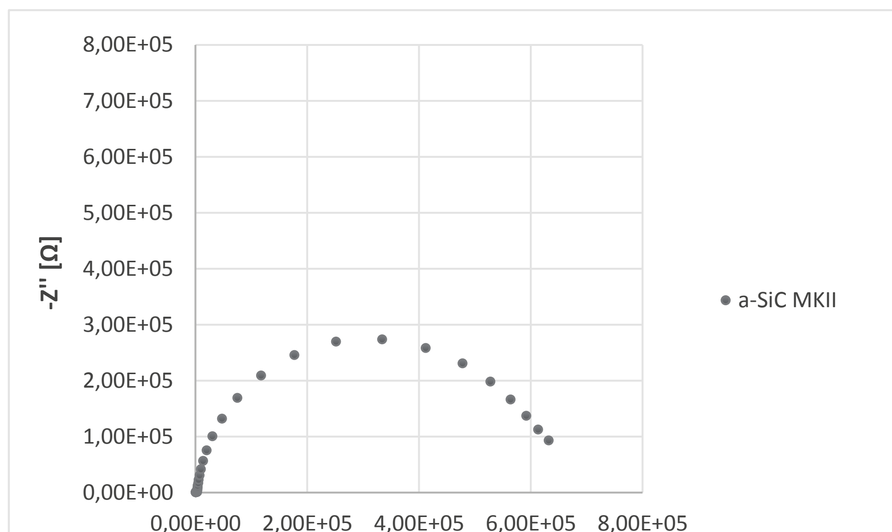

Figure 83: Nyquist plot for a-SiC MKII

2700 Ω. A charge transfer resistance of 6,35E+05 Ω is determined for the coating. The presence of two semicircles might indicate the formation of pores or beginning failure of the layer. The corresponding equivalent circuit model is shown in Figure 84.

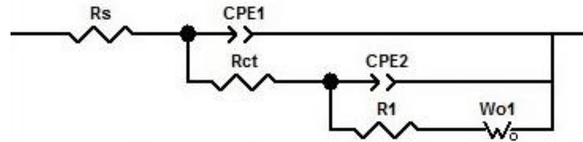

Figure 84: Equivalent circuit model for a-SiC MKII

The Nyquist plot for the a-SiC MKII variant with heat treatment (cf. Fig. 85) is described with the model for a simple Randles cell (cf. Fig. 86). By applying a heat treatment, the charge transfer resistance is increased from 6,35E+05 up to 9,68E+07 Ω. The annealing seems to entail a decrease in the conductivity and consequently in the corrosion susceptibility of the a-SiC thin films.

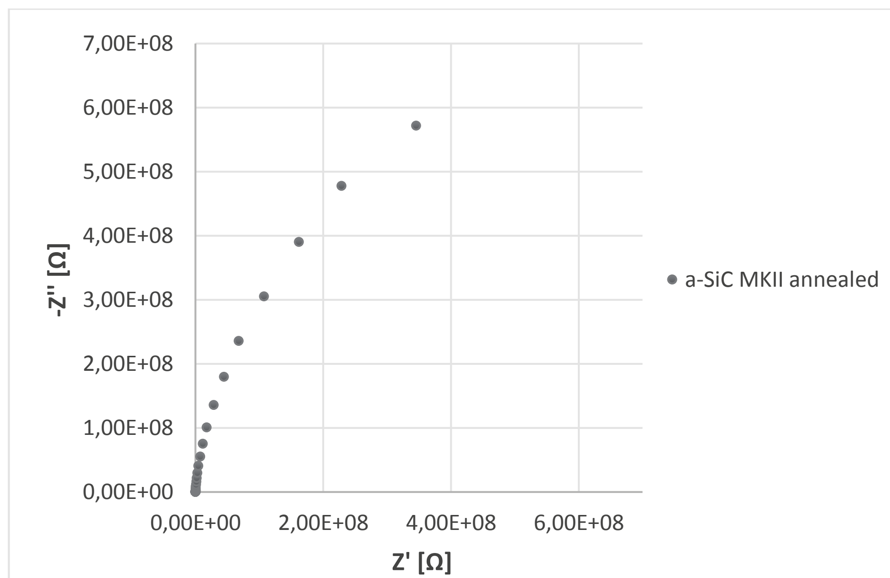

Figure 85: Nyquist plot for a-SiC MKII after thermal treatment

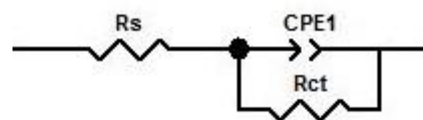

Figure 86: Equivalent circuit model for a-SiC MKII annealed and a-SiC CxZ

The a-SiC thin film deposited in the CxZ chamber exhibits greatly enhanced corrosion behaviour compared to the MKII types (cf. Fig. 87). The data is fitted with the equivalent circuit model of a simple Randles cell (cf. Fig. 86), calculating a charge transfer resistance of 9,68E+07 Ω. The EIS spectrum of the corresponding annealed sample is shown in Fig. 88. It appears as purely capacitive and undamaged

coating (cf. Fig. 89), a charge transfer resistance cannot be determined based on the equivalent circuit model.

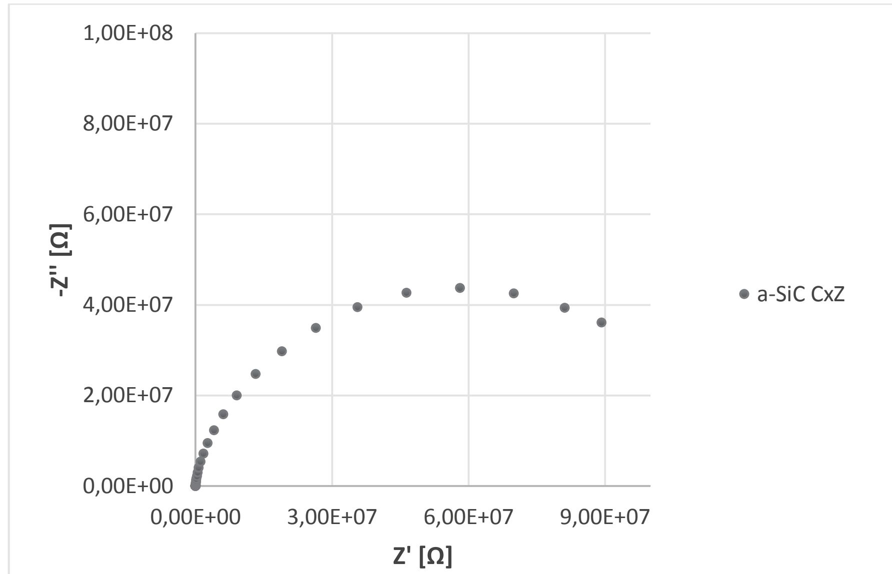

Figure 87: Nyquist plot of a-SiC CxZ

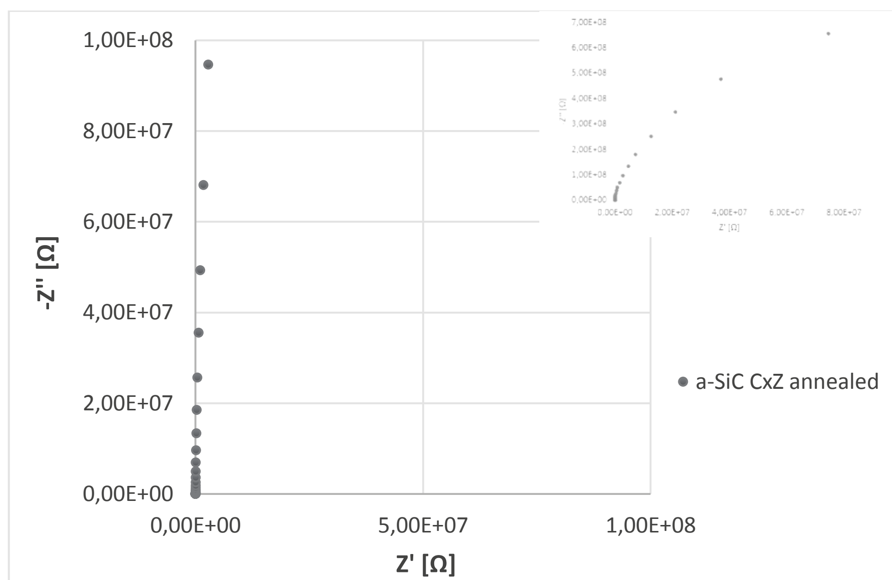

Figure 88: Nyquist plot of a-SiC CxZ after heat treatment, shown in detail in the right corner

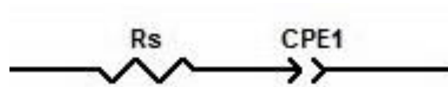

Figure 89: Equivalent circuit model for a-SiC CxZ after annealing

As a result, the films of a-SiC deposited in the CxZ chamber are more resistant to corrosion than the ones processed in the MKII chamber. The charge transfer resistance is two orders of magnitude higher for the standard a-SiC CxZ layer compared to the a-SiC film deposited in the MKII chamber, indicating

an increased corrosion stability. The results from the Tafel plot analysis agree very well with the ones obtained by EIS measurements (cf. Table 16). Applying a heat treatment on the wafers after deposition greatly increases the conductivity of the a-SiC coatings. For the MKII variant, annealing leads to an increase of the charge transfer resistance from 6,35E+05 to 9,68E+07 Ω.

The annealed CxZ layer was too little conductive to even be measured electrochemically, indicating very good electrochemical stability. This means that the annealed BKM film variant from the CxZ chamber is as corrosion resistant as for example PECVD nitride or oxide. For these films, due to high resistivity also no charge transfer resistance or corrosion rate could be determined.

Table 16: Comparison of corrosion rates and charge transfer resistances for the samples of lot VC058588

Sample	Annealing	Corrosion rate [mm/year]	Charge transfer resistance [Ω]
blank	no	1,18E-02	1,13E+05
MKII	no	3,13E-03	6,35E+05
MKII	yes	2,22E-06	9,48E+08
CxZ	no	6,77E-05	9,68E+07
CxZ	yes	-	-

The choice of deposition chamber has a significant impact on the electrochemical corrosion stability. The BKM a-SiC deposited in the CxZ chamber exhibits a corrosion rate of 6,77E-05 mm/year and a charge transfer resistance of 9,68E+07 Ω, while on the contrary the MKII film shows comparably small values of 3,13E-03 mm/year and 6,35E+05 Ω. The corrosion rate of the MKII film is only one order of magnitude higher than the one of the bare silicon wafer, the difference between the obtained charge transfer resistances is even smaller. Therefore the a-SiC MKII coating yields a corrosion inhibition efficiency factor of 61,72 % compared to the uncoated sample, while the a-SiC CxZ coating exhibits a high inhibition efficiency of more than 99 %.

The reason for this divergence in electrochemical corrosion resistance is the influence of the deposition chamber and method on film structure and composition. The results of previous TOF-ERDA measurements are displayed in Figure 90. The a-SiC CxZ film shows stoichiometric composition, while the MKII film has a high content of carbon of around 44 at.% and only about 20 at.% silicon. FT-IR spectroscopy measurements that have been previously conducted at the Infineon site in Villach show a broader and less intense peak for Si-C at around 780 cm^{-1} for the MKII film (Figure 91). Furthermore, the spectra of a-SiC MKII exhibit stronger pronounced peaks for Si-H and Si-C bonds than the CxZ film, indicating a decreased film density for MKII structures.

As mentioned before, increased carbon content is associated with microvoid formation in the amorphous network and reduced moisture barrier ability [jiang56]. Arce et al. [arce57] showed that a-SiC with a high carbon content of around 45 at.% also becomes oxidized upon six month exposure to air at room

temperature [arce57]. High humidity performance tests in an autoclave (AC tests) have shown that the tested CxZ film types are in general chemically stable during the tests. The investigated a-SiC MKII film types did not pass the AC test and showed changes in film stress. An increase in RF power by a factor of four yielded a MKII film that remained stable during the AC test. The high plasma power however damaged the silicon substrate, making the high power recipe inapplicable for high voltage termination structures due to severely increased leakage currents.

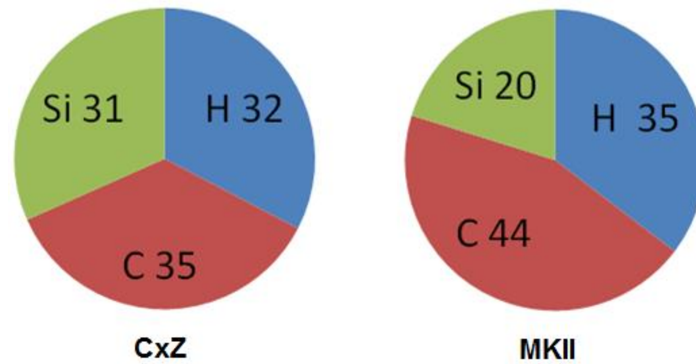

Figure 90: Elemental composition [at-%] of a-SiC deposited in CxZ and MKII chamber

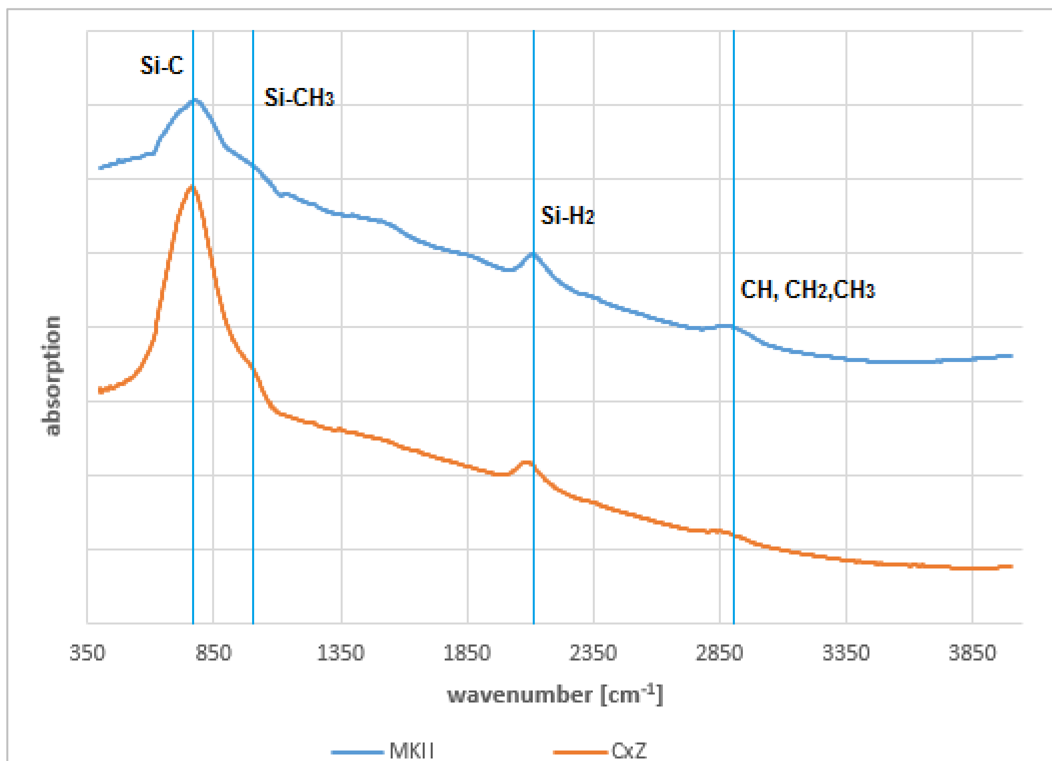

Figure 91: IR spectra of a-SiC deposited in CxZ and MKII chambers

The film parameters of both a-SiC CxZ and MKII are compared in Table 17. The films deposited in the CxZ chamber exhibit stoichiometric composition, a low Si-H and C-H content and chemical stability during AC tests. The MKII film type has a high carbon content, which results in a decreased refractive

index of 2,42 compared to 2,5 of the CxZ film. The increased carbon content leads to poor performance in the AC tests and reduced the overall film stability.

Table 17: Comparison of film parameters of a-SiC deposited in CxZ and MKII chambers

Film parameter	CxZ chamber	MKII chamber
Stoichiometry	1:1 Si:C	carbon rich
Infrared absorption	low SiH and CH content, a-SiC like	matrix dominated carbon rich
Autoclave stability	stable	not stable
Refractive index n	2,5	2,42
Tauc gap [eV]	2,42	2,1

The relationship between corrosion rates and charge transfer resistances for each sample is displayed in Figure 92. The improved corrosion stability as a consequence of the prior heat treatment can also be explained by the increased densification of the thin films. According to IR measurements by Oliveira and Carreño [oliv53] heat treatment leads to a decrease of Si-H and C-H bonds in a-SiC thin films. Moreover, they showed that heat treatment causes a reduction of the film thickness, concluding that it promotes the effusion of hydrogen and the densification of the layers [oliv53].

Annealing reduces the conductivity of the films because upon applying heat voids within the amorphous structure decrease [dutt54]. Thus, on the one hand the films become denser and are less likely to absorb water and on the other, heat treatment increases the electrical corrosion stability by reducing the conductivity of the films. By deposition of a-SiC in the CxZ chamber and subsequent annealing, the resulting film exhibits the same electrochemical corrosion stability as the highly resistive PR SiC (cf. chapter 4.2.4).

Due to denser structure however, the annealed CxZ BKM film is not water-absorbent and features an improved overall film stability compared to the polymer-like PR SiC.

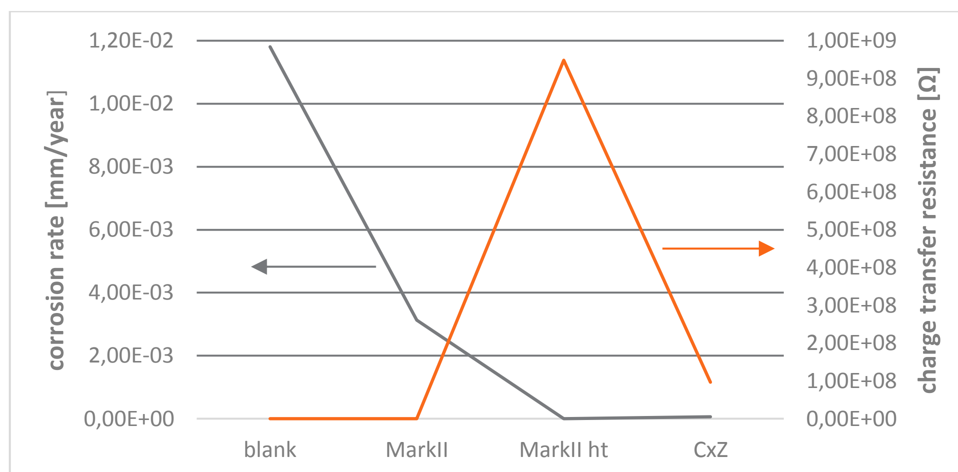

Figure 92: Corrosion rate and charge transfer resistance for each sample (ht: heat treatment)

As a conclusion, the choice of deposition chamber and method has a significant impact on the overall corrosion stability of a-SiC films. The BKM a-SiC film deposited in the CxZ chamber exhibit improved electrochemical corrosion stability and high humidity performance compared to the MKII BKM film. The CxZ a-SiC yields a corrosion rate of 6,77E-05 mm/year and a charge transfer resistance of 9,68E+07 Ω, while on the contrary the MKII film shows comparably small values of 3,13E-03 mm/year and 6,35E+05 Ω. The a-SiC MKII coating yields a corrosion inhibition efficiency factor of 61,72 % compared to the uncoated sample, while the a-SiC CxZ coating exhibits a high inhibition efficiency of more than 99 %. This divergence in electrochemical corrosion stability can be explained by the high carbon content of around 44 at.% and the increased inclusion of Si-H and C-H bonds in the amorphous network of MKII films.

A subsequent heat treatment of the samples enhances the electrochemical corrosion resistance of both CxZ and MKII samples. Annealing leads to hydrogen effusion and increased densification of the films. By annealing, the corrosion rate of the MKII film is reduced from 3,13E-03 to 2,22E-06 mm/year, resulting in an enhanced corrosion inhibition efficiency factor of over 99 %. Moreover, the heat treatment reduces the conductivity of the layers. Thus, upon annealing the charge transfer resistance of the MKII film is increased by three orders of magnitude.

The a-SiC CxZ film exhibits a charge transfer resistance two orders of magnitude higher than the MKII sample. Upon annealing, the CxZ film becomes too little conductive to even be measured electrochemically, which indicates an excellent corrosion stability. Thus, the annealed a-SiC CxZ film shows a high corrosion resistance comparable to PECVD oxides and nitrides.

5 Conclusions

The aim of this thesis was the tuning of the a-SiC film deposition process and the subsequent correlating of the obtained film parameters to electrochemical corrosion properties. Electrochemical corrosion of passivation films used in high power semiconductor devices is one of the major problems in overall device reliability. Due to the fact, that harsh environment conditions in the field challenge safety and stability of the power device, several tests with up-speeded aging conditions are used during development. However, such tests can take up to several thousand hours and the results are often difficult to interpret. Therefore, new test methods for single film systems were implemented in order to gain information on the influence of film properties on electrochemical corrosion behaviour. In order to meet this goal, several new approaches are assessed:

- An electrochemical cell in the three electrode arrangement was designed and manufactured
- Specimen coated with PECVD silicon carbides, nitrides and oxides were manufactured by tailoring prominent process parameters like plasma power density and gas flow variation
- The electrochemical cell was used to characterise every thin film with electrochemical impedance spectroscopy and Tafel plot analysis
- A model of the electrochemical corrosion mechanism of a-SiC was developed
- Charge transfer resistances and corrosion rates are correlated with other film parameters like SiC, SiH, CH bonding content, carbon hybridisation and elemental film composition
- The influence of silicon-nitrides and oxides as cap on a-SiC films was investigated
- The gained results tailor the process design for highly reliable film systems for future high power semiconductor solutions

With the results of this thesis, an approach was found to pre-select PECVD deposited film variants by their electrochemical durability for particular power semiconductors like IGBT und Diode.

The proposed model of the electrochemical corrosion mechanism in a-SiC is shown in Figure 93. The corrosive attacks on a-SiC are identified to be mainly of electrochemical nature. The Si-H groups on the surface of the films might be prone to hydrolysis leading to a conversion to Si-OH with additional hydrogen gas evolution; this hydrolysis reaction however is restricted to the surface of the film and does not affect the bulk material. Silicon compounds exhibit lower standard reduction potentials than carbon compounds, which makes them more likely to be oxidized. The electrochemical attacks of the bonds Si-Si and Si-C start from the surface of the film and might lead to a diminution of the compact layer. At the same time C-OH bonds or H_3O^+ species might become reduced.

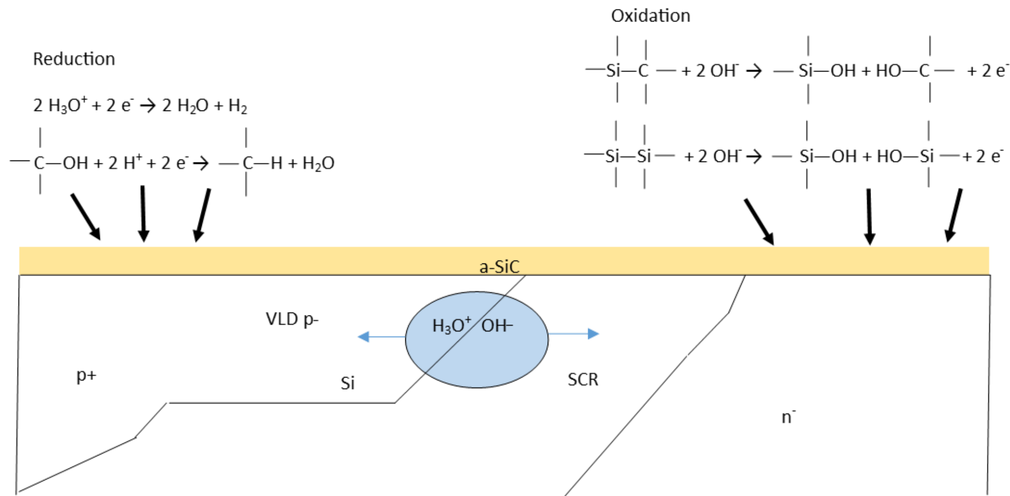

Figure 93: Graphical representation of the corrosion mechanism of a-SiC

The electrochemical measurements showed that the resistance of a-SiC against electrochemical attacks highly depends on the conductivity of the respective films. Furthermore, it was revealed that the PECVD operating conditions have a huge impact on the resistivity of the resulting a-SiC thin films.

It was shown that the RF power has an impact on structure, elemental composition and conductivity of the a-SiC films. Those are all properties that subsequently influence the overall stability and electrochemical corrosion resistance of the layers. By tuning the RF power density in the range between 1,11 and 2,55 W /cm² the corrosion rate increases from 2,38E-06 to 2,44E-03 mm/year and the inhibition efficiency factor decreases from 99,98 to 79,16 %.

The conductivity measurements with MIS-C structures revealed that higher RF power densities lead to a decrease of the resistivity of the a-SiC thin films, subsequently resulting in a higher susceptibility to electrochemical corrosion. The decrease of the measured refractive index of the films from 2,54 to 2,44 indicated an incremented incorporation of carbon in the a-SiC network. The film stress was shifted from -232 to -910 MPa upon increasing RF power, indicating an increasing densification of the layers.

Results from Raman spectroscopy showed that the RF power not only changes the elemental composition of the films, but also that it can be used to modify the structure and bonding types within the layers. High RF power entails the increasing graphitization carbon in of a-SiC, while low RF power results in growth of almost polymer-like films. Comparison of the IR spectra revealed that the a-SiC low RF power variant started developing the same features as the polymeric film PR SiC. The a-SiC film variant deposited at the lowest RF power density is the least conductive and exhibits the most improved stability against electrochemical corrosion. However, it cannot be used as electroactive barrier

layer in edge termination structures because it tends to absorb water, thus resulting in instable electrical performance and premature failure of the final device. The a-SiC material with increased density can withstand the absorption of water and thus, is able to maintain stable electrical performance, although its higher conductivity makes it more prone to electrochemical corrosion.

The gas flow rates of the precursor gases have an influence on the elemental composition and conductivity of a-SiC films. By gradually increasing the silane/methane gas flow ratio from 0,11 to 0,15 the silicon content of the films was tuned from 30 to 35 at.%. The refractive index was changed from 2,42 to 2,56 and the Tauc gap was decreased from 2,50 to 2,31. The elevated silicon content led to lowered conductivities and therefore improved electrochemical corrosion stability of the deposited thin films. As discussed before, at an RF power density of 2,55 W/cm² the a-SiC layers are already partly graphitized and therefore highly conductive, which is why the increased corporation of tetrahedrally bonded silicon apparently reduces the conductivity of the films. The film deposited with a silane/methane gas flow ratio of 0,15 yields a charge transfer resistance of 2,99E+08Ω, while the one with 0,11 only exhibits an R_{ct} of 1,33E+07, indicating an increased electrochemical corrosion resistance for the film with the highest silicon content. The corrosion rates lie within the range between 5,27E-05 and 7,89E-05 mm/year and therefore do not allow a quantitative comparison of the film variants. This might be due to the limitations of the Tafel extrapolation method, as the films do not differ much in R_{ct} and conductivity.

The tested oxides and nitrides were highly resistive, so neither a corrosion rate nor a charge transfer resistance could be determined, which indicates an elevated electrochemical corrosion stability. The respective EIS spectra showed a highly capacitive and undamaged coating. Thus, both oxides and nitrides exhibited better resistance against electrochemical attacks than the a-SiC thin films without annealing. In conclusions, the investigated nitrides and oxides are suitable passivation layers for a-SiC in terms of enhanced corrosion protection.

The polymeric PR SiC revealed a high resistivity and the same electrochemical behaviour as the oxide and nitride layers. Despite its stability against electrochemical attacks, polymeric SiC is no suitable substitute for a-SiC in semiconductor power devices. PR SiC tends to incorporate water in the polymeric network, which will lead to preliminary failure of the power device.

The choice of deposition chamber has a significant impact on the electrochemical corrosion stability. The a-SiC thin film deposited in the MKII chamber achieved a corrosion rate of 3,13E-03 mm/year and a charge transfer resistance of 6,35E+05 Ω, while the corresponding layer processed in a CxZ chamber exhibited improved values of 6,77E-05 mm/year and 9,68E+07 Ω. The reason for this divergence in electrochemical corrosion resistance is the influence of the deposition chamber and method on film structure and composition. The a-SiC CxZ film showed stoichiometric composition, while the MKII

film had a high content of carbon of around 44 at.% and only about 20 at.% silicon. IR spectra of a-SiC MKII showed a broader and less intense peak for Si-C at around 780 cm^{-1} and stronger pronounced peaks for Si-H and C-H bonds compared to the CxZ film. The high content of carbon and hydrogen-related bonds in a-SiC MKII might have led to the incorporation of microvoids in the structure and to decreased density of the layers, resulting in a reduced moisture barrier ability. High humidity performance tests in an autoclave have shown that the tested CxZ film types remained chemically stable, while the investigated a-SiC MKII film types failed.

Subsequent heat treatment of the films was proven to further enhance the corrosion behaviour of the samples. Annealing seems to be a means of lowering the conductivity of a-SiC thin films by filling voids and increasing film densification. The electrochemical corrosion resistance of both a-SiC CxZ and MKII were improved upon annealing. The corrosion rate of the MKII film was reduced from 3,13E-03 to 2,22E-06 mm/year, while the charge transfer resistance was increased by three orders of magnitude. The a-SiC CxZ film exhibited a charge transfer resistance two orders of magnitude higher than the MKII sample. Upon annealing, the resistivity of the CxZ film became too high for electrochemical corrosion analysis, which indicates an excellent corrosion stability.

By deposition of a-SiC in the CxZ chamber and subsequent annealing, the resulting film showed the same electrochemical corrosion stability as the highly resistive polymeric SiC. Due to the increased film density, the annealed CxZ layer is not water-absorbent and features an improved film stability.

Based on these findings it is possible to design a PECVD process that yields a-SiC films with improved electrochemical corrosion resistance and overall film stability. Elemental composition, structure, density and conductivity were identified as the major influencing factors for the resistance of a-SiC against moisture and electrochemical attacks. The obtained results showed that all these parameters can be varied over a wide range by modifying the PECVD conditions. When using a-SiC in power semiconductor devices, a compromise between electrochemical performance and good corrosion resistance of the thin films should be achieved.

It was shown, that with a simple electrochemical test setup, pre-selection of single layers for applications in the product is possible. With these results a deeper understanding of degradation reactions during electrochemical attack in the final product is gained.

References

[ahmad23] Z. Ahmad: Principles of Corrosion Engineering and Corrosion Control, p. 9-98, (2006)

[ahme42] R.A. Ahmed, R.A. Farghali, A.M. Fekry: Study for the Stability and Corrosion Inhibition of Electrophoretic Deposited Chitosan on Mild Steel Alloy in Acidic Medium, International Journal of Electrochemical Science (7), p. 7270 – 7282, (2012)

[arce57] R. Arce, R. R. Koropecki, R. H. Buitrago et al.: Direct evidence of porosity in carbon-rich hydrogenated amorphous silicon carbide films, in Journal of Applied Physics (66), p. 4544-4546, (1989)

[bloom34] I. Bloomer, R. Mirsky: Broadband spectrophotometry, Photonics Spectra 36 (5), p. 86-92, (2002)

[bull40] J. Bullot, M.P. Schmidt: Physics of Amorphous Silicon-Carbon Alloys, Physica status solidi 143 (2), p. 345-418, (1987)

[caff24] E. McCafferty: Introduction to Corrosion Science, p. 127 – 139, (2010)

[chung52] Y. Chung: Introduction to Materials Science and Engineering, p. 79 & 48-49, (2007)

[dasg4] N. Dasgupta, A. Dasgupta: Semiconductor Devices – Modelling and Technology, p. 76-77, (2004)

[desch49] T. Deschaines, J. Hodkiewicz, P. Henson: Characterization of Amorphous and Microcrystalline Silicon Using Raman Spectroscopy, Thermo Fisher Scientific Application Note 51735, (2009)

[dieb33] A.C. Diebold, W.W. Chism et al.: Metrology for on-chip interconnect dielectrics, in Handbook of Silicon Semiconductor Metrology, ed. by A.C. Diebold, p. 117-118, (2001)

[dutt54] R. Dutta, P.K. Banerjee, S.S. Mitra: Effect of Hydrogenation on the electrical conductivity of amorphous silicon carbide, Solid State Communications Vol. 42 (3), p. 219-222, (1982)

[entre36] Entrepix Inc.: Opti-Probe 5240, http://www.entrepix.com/thermawave/opti-probe/entrepix-opti-probe-5240.php (accessed November 21, 2016)

[fabj38] E.Š. Fabjan, T. Kosec, V. Kuhar, A.Legat: Corrosion stability of different bronzes in simulated urban rain, Materials and technology 45 (6), p. 585-591, (2011)

[ferra64] A.C. Ferrari, J. Robertson: Raman spectroscopy of amorphous, nanostructured, diamond-like carbon, and nanodiamond, in Philosophical Transactions of the Royal Society 362 (1824), p. 2477-2512, (2004)

[flew35] A.J. Flewitt, W.I. Milne: a-Si:H TFT Thin Film and Substrate Materials, Thin Film Transistors Volume 1, ed. by Y. Kuo, p. 59-60, (2004)

[fox60] M. Fox: Optical Properties of Solids, p. 3-42, (2001)

[fran31] S. Franssila: Introduction to Microfabrication, p. 58-60, (2010)

[gamry29] Gamry Instruments: Basics of Electrochemical Impedance Spectroscopy, http://www.gamry.com/application-notes/EIS/basics-of-electrochemical-impedance-spectroscopy/ (accessed Septembre 29, 2016)

[gaug65] G. Gauglitz, T. Vo-Dinh: Handbook of Spetroscopy Volume 1, p. 43-44 & 557, (2003)

[ghali42] E. Ghali: Corrosion resistance of Aluminum and Magnesium Alloys, p. 588-589, (2010)

[guru51] S. Guruvenket, M. Azzi, D. Li et al.: Structural, Mechanical, Tribological, and Corrosion Properties of a-SiC:H coatings prepared by PECVD, in Surface & Coatings Technology (204), p. 3358-3365, (2010)

[hamd62] A.S. Hamdy, E. El-Shenawy, T. El-Bitar: Electrochemical Impedance Spectroscopy Study of the Corrosion Behavior of Some Niobium Bearing Stainless Steels in 3.5% NaCl, in International Journal of Electrochemical Science (1), p. 171-180, (2006)

[herm43] M. Hermann, K. Sempf: Electrochemical corrosion of silicon carbide ceramics in sodium hydroxide, Journal of European Ceramic Society 34 (7), p. 1687-1693, (2014)

[hueb3] R. Huebener: Leiter, Halbleiter, Supraleiter – Eine Einführung in die Festkörperphysik, p. 68-77, (2013)

[hura14] J. Huran, L. Hrubcin et al.: Properties of amorphous silicon carbide films prepared by PECVD, in Vacuum (47), 10, p. 1223-1225, (1996)

[hype58] Hyperphysics Georgia State University: Band Theory of Solids, http://hyperphysics.phy-astr.gsu.edu/hbase/Solids/band.html (accessed: February 12, 2017)

[ili16] C. Iliescu, D.P. Poenar: PECVD Amorphous Silicon Carbide (a-SiC) layers for MEMS applications, in Physics and Technology of Silicon Carbide Devices, ed. by Y. Hijikata, p. 131-148, (2012)

[ino50] Y. Inoue, S. Nakashima et al.: Raman Spectra of Amorphous SiC, in Solid State Communications (48), 12, p. 1071-1075, (1983)

[janz12] S. Janz: Amorphous Silicon Carbide for Photovoltaic Applications, p. 18-22, 49-57 & 204, (2006)

[jiang56] L. Jiang, X. Chen, X. Wang et al.: a-SiC$_x$:H films deposited by plasma-enhanced chemical vapour deposition at low temperature used for moisture and corrosion resistant applications, in Thin Solid Films Vol. 352 (1-2), p. 97-101, (1999)

[jung15] C.-K. Jung, D.-C. Lim et al: Hydrogenated amorphous and crystalline SiC films grown by RF-PECVD and thermal MOCVD; comparative study of structural and optical properties, in Surface and Coatings Technology (171), p. 46-50, (2003)

[kahn48] M. Kahn: Room-Temperature Deposition of DLC Films by an Ion Beam Method, Reactive Magnetron Sputtering and Pulsed Laser Deposition: Process Design, Film Structure and Film Properties, p.34-50, (2009)

[kasa61] S. Kasap, P. Kapper: Springer Handbook of Electronic and Photonic Materials, p. 47-49, (2006)

[knip8] U. Knipper: Untersuchungen zur Robustheit von IGBT-Chips im Lawinendurchbruch, p. 25-28, (2011)

[kuhm55] D. Kuhman, S. Grammatica, F. Jansen: Properties of Hydrogenated Amorphous Silicon Carbide Films prepared by Plasma-enhanced Chemical Vapour Deposition, in Thin Solid Films Vol. 177 (1-2), p. 253-262, (1989)

[li13] D. Li, S. Guruvenket et al.: Effect of C/Si Ratio on the Electrochemical Behavior of a-SiC_x:H Coatings on SS301 Substrate Deposited by PECVD, International Journal of Corrosion, (2014)

[lnf59] LNF Wiki University of Michigan: Plasma enhanced chemical vapour deposition, http://lnf-wiki.eecs.umich.edu/wiki/Plasma_enhanced_chemical_vapour_deposition (accessed February 12, 2017)

[lutz1] J. Lutz, H. Schlangenotto, U. Scheuermann: Semiconductor Power Devices - Physics, Characteristics, Reliability, p. 1-18 & 382-390, (2011)

[lutz5] J. Lutz: Halbleiter-Leistungsbauelemente, p. 30-37, (2012)

[lvov28] V.F. Lvovich: Impedance Spectroscopy, p. 1-5, (2012)

[metr27] Metrohm Autolab B.V.: Electrochemical Impedance Spectroscopy (EIS) Part 1, Application Note EIS01, (2011)

[metr30] Metrohm Autolab B.V.: Corrosion Part 4, Application Note COR04, (2011)

[ncstate46] NC State University: Electrical and Computer Engineering, Power Semiconductor Devices, https://www.ece.ncsu.edu/research/pes/psd (accessed January 18, 2017)

[oliv53] A.R. Oliveira, M.N.P. Carreño: Post thermal annealing crystallization and reactive ion etching of SiC films produced by PECVD, in Journal of Non-Crystalline Solids (352), p. 1392-1397, (2006)

[olymp44] N&K Technology Inc.: Semiconductor Olympian Series, http://www.nandk.com/metrology-systems/semiconductor/olympian-series/ (accessed December 07, 2016)

[opsal32] J. Opsal, Kla-Tencor Corp.: Beam profile ellipsometer with rotating compensator, US7400403B2, (2008)

[pern17] M. Perný, V. Šály et al.: AC Impedance spectroscopy of Al/a-SiC/c-Si(p)/Al Heterostructure under Illumination, in Journal of Electrical Engineering (65) No.3, p. 174-178, (2014)

[photo37] Photonic Microdevices: Optiprobe 5240 Description, http://www.photonicmicrodevices.com/files/OptiProbe_5240_Description.pdf (accessed November 21, 2016)

[rash7] M.H. Rashid: Power Electronics Handbook, p. 15-25 & 71-88, (2007)

[refra47] Mikhail Polyanskiy: Refractive Index Database, http://refractiveindex.info/ (accessed January 29, 2017)

[revie22] R.W. Revie, H.H. Uhlig: Corrosion and Corrosion Control, p.1-63, (2008)

[robe10] J. Robertson: Diamond-like amorphous carbon, Materials Science and Engineering (R 37), p.129-281, (2002)

[sadd6] S.E. Saddow: Silicon carbide biotechnology, p. 1-61, (2012)

[schmidt63] G. Schmidt, J.G. Bauer, C. Schaeffer et al., Infineon Technologies AG: Semiconductor Device with a Passivation Layer, US 20140061733 A1, (2012)

[schröd9] D. Schröder: Leistungselektronische Bauelemente, p. 656-660, (2006)

[silv26] V. Silva: Impedance Spectroscopy, reference entry, http://link.springer.com/referenceworkentry/10.1007/978-3-642-40872-4_1886-1 (accessed Septembre 22, 2016)

[sing2] M.D. Singh, K.B. Khanchandani: Power Electronics, p.4-8 & 135, (2008)

[smith41] D.W. Smith: Inorganic substances, p. 175, (1990)

[stans21] E.E. Stansbury, R.A. Buchanan: Fundamentals of Electrochemical Corrosion, p. 1-13, (2000)

[stenz39] O. Stenzel: Optical Coatings, p. 194, (2014)

[wiki45] Wikipedia, the free Encyclopedia: Standard electrode potential (data page), https://en.wikipedia.org/wiki/Standard_electrode_potential_(data_page) (accessed January 11, 2017)

[wool19] J.A. Woollam Co., Inc.: Thin Film Thickness, https://www.jawoollam.com/resources/ellipsometry-tutorial/thin-film-thickness (accessed October 20, 2016)

[wool20] J.A. Woollam Co., Inc.: Guide to Using WVASE, p. 2-1 – 2-26, (2012)

[xia18] L.-Q. Xia, M. Chang: Chemical Vapour Deposition, in Handbook of Semiconductor Manufacturing Technology, ed. by R. Doering, Y. Nishi, p. 13-1 – 13- 88, (2008)

[zeng11] A. Zeng, V.F. Neto et al.: Diamond-like carbon (DLC) films as electrochemical electrodes, in Diamond and Related Materials (43), p. 12-22, (2014)

[zoski25] C.G. Zoski (ed.): Handbook of Electrochemistry, p. 11-22, (2007)